

UNIVERSITY OF CALIFORNIA
RIVERSIDE

A Measurement of Bottom Quark Production
in $p\bar{p}$ -Collisions at $\sqrt{s} = 1.8$ TeV

A Dissertation submitted in partial satisfaction
of the requirements for the degree of

Doctor of Philosophy

in

Physics

by

Thorsten Bernhard Huehn

December, 1995

Dissertation Committee:

Professor A. Kernan, Chairperson

Professor Gordon VanDalen

Professor Jose Wudka

The Dissertation of Thorsten Bernhard Huehn is approved:

Thorsten Huehn

Anne Kermans

Committee Chairperson

University of California, Riverside

Acknowledgements

First I would like to thank my advisor Anne Kernan for giving me the opportunity to work in high energy physics, and for her support throughout my graduate career. I benefitted immensely from her high standards for the physics analysis itself as well as her insistence on concisely communicating my results to others.

I owe great debt to Steve Wimpenny for his guidance and advice throughout the analysis, and to Jim Cochran for his input on the infinite number of small problems "popping up" along the way. Thanks to both Steve and Jim for reading preliminary versions of the thesis.

Yvonne Ayers at UCR was of immense help way beyond the call of duty with administrative matters, especially throughout my stay at Fermilab. Thanks also to my colleagues in the UCR cubicles at DØ, Ray Hall and Brajesh Choudhary, for many uplifting discussions, and to Ann Heinson in Riverside for her help and suggestions.

I thank Arthur Maciel for countless helpful discussions and suggestions on my analysis. I also thank Jussara de Miranda, Joao de Mello, Marcelo Nicola, Andre Sznajder and Wagner Carvalho for help with the Monte Carlo simulation and discussions and many useful discussion on *b*-physics topics. It was a pleasure to work with Guilherme Lima, Vitor Oguri and Mario Vaz on the early parts of the analysis and the commissioning of the muon level 1 trigger. Thanks also to our long time system manager Paul Russo for his very skillful management of the offline computing systems at DØ.

Ken Johns and Andrzej Zieminski provided strong leadership for the bottom quark physics group at DØ, Dave Hedin and Daria Zieminska shared their knowledge of the DØ muon reconstruction program, Amber Boehnlein and Dan Claes answered many questions on the trigger simulation programs and Rich Astur shared his expertise on the jet reconstruction algorithm. I thank Herbert Greenlee for his advice and help with the Monte Carlo event generation.

Thanks to Kamel Bazizi for his help on the analysis and the trigger and to Dan Green for his advice.

I had the great privilege of meeting many other people at Fermilab who also made life out here tolerable, and at times even enjoyable. They are too many to name them all, but definitely among them were: Gene Alvarez, Chris Murphy, Leigh Markosky, Freedy Nang, Myungyun Pang, Regina Demina, Scott Snyder, Srinivasa Rajagopalan, Joey Thompson, Paul Rubinov, Meena Narain, Steve Jerger, Tom Fahland, Cecilia Gerber, Daniel Elvira, Erfan Amidi, ...

At Riverside I would like to thank Nasser Budraa, Tom Durbin, Jim Harvey and Oscar Bernal for many lively lunch discussions and a good time while studying for the comprehensive exams.

Most importantly I would like to thank my parents. Their steady support throughout my education and belief in my success made all this possible. I dedicate this thesis to them.

Work supported by the U.S. Department of Energy

Contract No. DE-AM03-76SF00010

and

Grant No. DE-FG03-94ER40837

ABSTRACT OF THE DISSERTATION

A Measurement of Bottom Quark Production in $p\bar{p}$ -Collisions at 1.8 TeV

by

Thorsten Bernhard Huehn

Doctor of Philosophy, Graduate Program in Physics

University of California, Riverside, December 1995

Professor Anne Kernan, Chairperson

We present a measurement of the bottom quark production cross section at a center of mass energy of 1.8 TeV in the rapidity region $|y| < 1$ and the transverse momentum range 13 to 37 GeV/c. The measurement is extracted from a dataset of 2707 events containing muons and jets, corresponding to an integrated luminosity of 228 nb^{-1} , taken during the 1992-93 collider run of the Tevatron proton-antiproton collider at Fermilab. The measurement is about two standard deviations above QCD predictions, but is consistent with it within measurement uncertainties and uncertainties in the QCD calculation.

Contents

List of Figures	xx
List of Tables	xxii
1 Overview	1
2 Heavy Quark Cross-Sections in QCD	5
2.1 Cross Sections and Perturbative QCD	5
2.2 Heavy Quark Production	8
2.3 Summary	15
3 The Apparatus	16
3.1 The Fermilab Accelerator Complex	16
3.1.1 $p\bar{p}$ -Production	16
3.1.2 Luminosity	20
3.2 An Overview of the DØDetector	21
3.3 Central Detectors	23
3.3.1 The Vertex Drift Chamber	23
3.3.2 The Central Drift Chamber	24

3.4	Calorimeter	26
3.4.1	Overview and Design	26
3.4.2	Calorimeter Performance	29
3.5	The Muon Detector	31
4	The Trigger System	40
4.1	Overview	40
4.2	The Muon-Jet Trigger	42
4.3	Main Ring Veto	43
4.4	Minimum Bias Trigger (Level 0)	45
4.5	Muon Trigger	46
4.6	Calorimeter Trigger	48
5	Off-Line Reconstruction	50
5.1	Overview	50
5.2	Vertex Reconstruction	50
5.3	Muon Reconstruction	52
5.4	Jet Reconstruction	54
6	Simulation of Data	59
6.1	Introduction	59
6.2	Generation of Event 4-Vectors	60
6.3	Detector Simulation	64
6.4	Trigger Simulation	65
6.5	The Simulated Data Samples	66

6.6	Test of Validity of ISAJET Predictions	68
6.7	Summary	72
7	Data Selection	73
7.1	Introduction	73
7.2	Fiducial and Kinematic Cuts	74
7.2.1	Muons	74
7.2.2	Jets	76
7.3	Muon Quality Cuts	77
7.4	Background Cuts	79
7.4.1	Background to Jets	79
7.4.2	Background to Muons	80
7.5	Summary	85
8	Efficiencies	92
8.1	Introduction	92
8.2	Jet Efficiency	94
8.2.1	Jet Trigger Efficiencies	94
8.2.2	Jet Reconstruction Efficiency	98
8.2.3	Efficiency of Jet Quality and Fiducial Cuts	101
8.2.4	Overall Jet Efficiencies	103
8.3	Muon Efficiencies	105
8.3.1	Muon Trigger Efficiency	105
8.3.2	Muon Reconstruction Efficiencies	106
8.3.3	Muon Offline Cut Efficiencies	106

8.3.4	Overall Muon Efficiency	111
8.4	Summary	111
9	The Muon Spectrum	113
9.1	Introduction	113
9.2	Differential Muon Cross Section for μ -Jet Events	114
9.3	Isolation of the $b\bar{b}$ -Component of the Muon p_T -Spectrum	119
9.4	Summary	128
10	The b-Quark p_T-Spectrum	129
10.1	Overview	129
10.2	Unfolding the Muon Momentum Resolution	130
10.3	Extraction of the b -Quark p_T -Spectrum	134
10.4	Summary	139
11	Conclusions	140
11.1	Introduction	140
11.2	Current Status of b -Quark Production Cross Sections	140
11.3	Future b -Quark Cross Section Measurements at D \emptyset	148
A	Modelling of the Muon Detector Efficiencies and Resolutions	152
B	Decays-in-Flight of Pions and Kaons	155
C	Bayes' Method for Unfolding Resolution Effects	160

List of Figures

2.1	Examples of Feynman Diagrams for leading (a and b) and next-to-leading order (c to e) QCD processes for b -production	9
2.2	b -quark production cross section as a function of the transverse momentum of the quark, for $ y < 1$, from the NDE calculation [14]. The central value (solid line) is for $\Lambda = 140$ MeV and $\mu = \mu_0$. The dotted lines define the theoretical uncertainty obtained by varying Λ and μ to 187 MeV and $\mu_0/2$ (upper line) versus 100 MeV and $2\mu_0$ (lower line).	10
2.3	Contribution from gluon-gluon, gluon-quark and quark-quark processes to b -quark production.	11
2.4	Fraction of next-to-leading order contribution to b -production. .	12
2.5	Ratio of b -quark production cross section obtained with DFLM/MRSD0 structure functions.	14
3.1	An overview of the Fermilab accelerator complex with the DØ and CDF detectors.	17
3.2	An isometric cut-away view of the DØ detector.	21
3.3	A cross section of the DØ central detectors	23

3.4	End-view of the central drift chamber, shown are the 7 sense wires per cell as well as the delay-lines embedded in the walls of the cells. There are guard wires for field-shaping on either side of the sense wires.	25
3.5	The DØ calorimeters, showing the central and the two end-cryostats and the various calorimeter subsystems.	26
3.6	A schematic of the calorimeter cell structure.	27
3.7	Calorimeter response for electrons and pions of known energy in the testbeam (top). The bottom plots show the residuals (deviations) from linearity for electrons and pions.	30
3.8	Elevation view of the DØ detector showing the three layers of proportional drift tubes of the muon system and the toroidal magnet. The "main ring" is passing through the detector ≈ 1 m above the Tevatron beam pipe.	32
3.9	Schematic drawing of a muon magnetic spectrometer.	33
3.10	Number of interaction lengths in the DØ detector as a function of polar angle. The dip at 40° is due to the gap between the CF and EF magnet toroids.	35
3.11	Cross section of a drift tube, showing the equipotential lines and the cathode pads on the top and bottom of the cell.	35

3.12 Cathode pad showing the inner and outer sections divided by a repeating diamond pattern. Below is a plot of the ratio of difference and sum of the charged induced on the inner and outer sections of the pads versus the position of the hit along the wire.	36
3.13 Distance of muon trajectory from the sense wire versus drift time.	37
5.1 The jet energy scale correction factor for the jet E_T shown for jets of two different pseudorapidities. Shown are the best estimate for the correction, and an upper and lower limit indicating the uncertainty in the corrections.	56
6.1 Peterson fragmentation function for b and c -quarks for $\epsilon_Q = 0.022$ and 0.15 , respectively.	63
6.2 Comparison of the inclusive charged hadron cross section predicted by ISAJET and from CDF data. Fig. b) shows the ratio of CDF/ISAJET.	69
6.3 Comparison of ISAJET and NDE [14] calculations for b -production (figs a, c) and c -production (figs b ,d), as a function of the p_T of the heavy quark. The data points in a) and b) denote ISAJET predictions, while the solid line is for the NDE calculation. All plots are for $ y < 1.0$ of the b and c quarks. The solid line in c) and d) is a fit of a constant to the ratio NDE calculation/ISAJET. .	71

7.1	Ratio of muon ϕ -distributions from Data and Monte Carlo. The discrepancy in the region around 90° is due to radiation damage in the muon A chambers near the Main Ring pipe.	75
7.2	Summed energy deposition in the calorimeter cells traversed by a muon track and in the eight neighboring cells.	78
7.3	Impact parameter I_T in the transverse (non-bend) plane as a function of muon momentum for (a) data and (b) Monte Carlo. Kinematic, fiducial and muon quality cuts have been applied. The curve shows the cut $I_T = \sqrt{(300/p)^2 + 100}$ cm.	81
7.4	Bend view impact parameter I_{bv} as a function of muon momentum for (a) data and (b) Monte Carlo. Kinematic, fiducial and muon quality cuts have been applied to both samples. The curve shows $I_{bv} = \sqrt{(300/p)^2 + 100}$ cm.	82
7.5	The time difference between the actual and fitted T_0 values, ΔT_0 , for muon tracks for a) beam data and b) cosmic rays. All cuts (table 7.1) have been applied to the beam data; to the cosmic data only fiducial and kinematic cuts were applied. . .	84
7.6	Angular separation in Θ and ϕ of the track reconstructed in the muon detector and the closest track in the centra drift chamber.	86
7.7	p_T and η -distributions of all muons in the data sample after selection cuts.	88
7.8	E_T and η -distribution of the jet with the highest transverse energy in the event after selection cuts.	89

7.9	Event display of a 6 GeV/c muon within an 11 GeV jet. The bottom figure shows a blowup of the calorimeter and central detectors.	90
8.1	(a) Level 1 trigger efficiency for reconstructed jets with $E_T > 20$ GeV. The solid points show the efficiency obtained from inclusive muon data, while the dotted points are from Monte Carlo. Fig. (b) shows the ratio of data/Monte Carlo. Jets in the shaded regions ($1.0 < \eta < 1.6$ and $ \eta > 2.2$) are not included in the analysis.	95
8.2	(a) Level 1 trigger efficiency for reconstructed jets as a function of jet- E_T , for jets with $ \eta < 1.0$. The Monte Carlo is shown for trigger tower thresholds of 3.0 and 4.25 GeV. Fig. b) shows the ratio of data: Monte Carlo efficiencies for both thresholds.	97
8.3	Level 2 jet efficiency as a function of the E_T of the reconstructed jet.	98
8.4	Overall jet trigger efficiencies as a function of E_T of the highest E_T jet in the event. The efficiency obtained from the inclusive muon sample is compared to the Monte Carlo result.	99
8.5	Jet Reconstruction and offline quality cut efficiencies from Monte Carlo. a) The solid histogram indicates the reconstruction efficiencies, while the dotted histogram indicates the efficiency of the offline cuts. b) shows the combined reconstruction and offline jet quality cut efficiencies.	100

8.6 Efficiency of the jet fiducial cut in η for the Monte Carlo. The abscissa shows the transverse energy of the highest E_T jet in the event, while the ordinate shows the transverse energy of the highest E_T jet within $ \eta < 1.0$ or $1.6 < \eta < 2.2$	102
8.7 Combined jet efficiency, including trigger, reconstruction and offline cuts, for Monte Carlo events. The efficiency is parameterized in terms of the E_T of highest jet generated by ISAJET. The dashed lines show the uncertainty in the jet efficiency. The shaded region denotes the region excluded by the 15 GeV minimum E_T -cut. The solid line is a fit through the data points, the dotted lines indicate an uncertainty of 13%.	104
8.8 Muon trigger efficiency from Monte Carlo. The efficiency is plotted as a function of the transverse momentum of the muon as generated in ISAJET.	105
8.9 Muon reconstruction efficiency from Monte Carlo. The efficiency is plotted as a function of (a) p_T^μ and (b) η^μ	107
8.10 Efficiency comparison of data and Monte Carlo for a) the “three layer requirement” and (b) the central track match requirement.	108
8.11 Efficiency of the offline muon cuts as a function of the measured muon transverse momentum. The plot shows the Monte Carlo efficiencies corrected with the factor “data/Monte Carlo from table 8.1.	110
8.12 Overall muon efficiency. The dotted lines show the 13% systematic error.	111

9.1	Differential muon spectrum $d\sigma^\mu/dp_T^\mu$ for muon-jet events with $ \eta^\mu < 0.8$, and $E_T > 15 \text{ GeV}$ for the highest E_T jet in the event. The experimental data points are compared to a Monte Carlo prediction, (section 6.2) with the experimental momentum resolution (appendix A) applied to the generated muon momentum.	115
9.2	Prediction of the fraction of muons from b -quark production from Monte Carlo.	119
9.3	Definition of p_T^{REL}	120
9.4	Monte Carlo p_T^{REL} -distributions for b and c -quark decays, and for in-flight decays of pions and kaons. The plots show the Monte Carlo with statistical errors (points) and the parameterization used in the fit (smooth line).	122
9.5	Experimental p_T^{REL} distributions for $3 < p_T^\mu < 24 \text{ GeV}/c$. The smooth curves are fits to the summed Monte Carlo p_T^{REL} distributions for b -, c -quark and π/K decay events.	123
9.6	Muon spectrum for events with $ \eta^\mu < 0.8$ and $E_T^{\text{high}} > 15 \text{ GeV}$ with c , π/K and W/Z components subtracted, compared to a Monte Carlo calculation of $b \rightarrow \mu X$ processes (solid histogram). The dashed histogram indicates the uncertainty in the Monte Carlo prediction.	125

10.1 The effect of the muon momentum resolution on the measured muon p_T spectrum. The solid line shows the true momentum spectrum from b and \bar{b} production and the dashed line shows the spectrum after muon momentum resolution has been applied. The dotted lines indicate the uncertainty on the resolution function.	131
10.2 Comparison of the muon transverse momentum spectrum $d\sigma/dp_T^\mu$ after correction for muon momentum resolution effects, and the ISAJET prediction (histogram) for $b/\bar{b} \rightarrow \mu X$ production. The inner error bars are the statistical error, and the outer error bars show the sum in quadrature of statistical and systematic errors.	132
10.3 Illustration of the method used to convert the muon spectrum into the b -quark production cross section. The conversion factor $f^{\mu \rightarrow b}$ is obtained by dividing the area of the outer (empty) histogram by the area of the shaded histogram.	135
10.4 b -quark production integral cross section as a function of p_T^{\min} , for $ y^b < 1$, compared to the NDE prediction. The inner error bars on the data show the statistical error, the outer ones indicate the sum in quadrature of statistical and systematic errors. The solid line shows the central QCD prediction, and the dashed lines show the uncertainty arising from varying Λ and μ_0	137

11.1 Integral b -quark cross sections from dimuon and muon-jet events from the UA1 experiment at CERN, in $p\bar{p}$ collisions at $\sqrt{s} = 0.63$ TeV, for $ y^b < 1.5$. The central theory prediction (solid line) and uncertainties (dashed lines) are described in the text.	141
11.2 Integral b -quark production cross sections for $ y^b < 1$ from the CDF experiment in $p\bar{p}$ collisions at $\sqrt{s} = 1.8$ TeV.	143
11.3 b -quark production integral cross section from this analysis, compared to the NLO QCD theory prediction.	144
11.4 b -quark production integral cross section from this analysis, compared to DØ measurements based on inclusive muon, inclusive dimuon, and J/Ψ data.	146
11.5 Ratio data / theory prediction for the b -quark production cross section measurement from (a) DØ at $\sqrt{s} = 1.8$ TeV for $ y^b < 1.0$, and b) UA1 at $\sqrt{s} = 0.63$ TeV for $ y^b < 1.5$. The theory curves are described in the text.	149
A.1 Muon momentum resolutions from MUSMEAR. The curve denotes the resolution of $\Delta(1/p) = \sqrt{(0.18/p)^2 + 0.008^2}$ measured from J/ψ and Z data.	153
B.1 Prompt particles generated in ISAJET jet events. Only particles of $p_T > 4$ GeV/c and $ \eta < 0.8$ are plotted. More than 90% of the charged particles are pions and kaons which can decay to muons in the detector.	156

B.2 Fraction of charged pions and kaons in the inclusive charged hadron spectrum generated by ISAJET. 158

List of Tables

4.1	Collider runs used in the Analysis	44
6.1	The Simulated Data Sample	66
7.1	Summary of Muon and Jet Selection Cuts	87
8.1	Comparison of the efficiency for the offline cuts in the data and Monte Carlo for $p_T^\mu > 4 \text{ GeV}/c$	109
8.2	Efficiencies for muons and jets	112
9.1	The differential muon spectrum for muon-jet events, showing the p_T^μ intervals, the number of observed muons in each of the intervals, the differential muon cross section and its statistical error. The muon differential cross section and its statistical error are calculated with formulas 9.2 and 9.3, respectively. calculated with form	116
9.2	Mean/RMS deviation from the mean for p_T^{REL} distributions from Monte Carlo.	124

9.3 Calculation of $d\sigma/dp_T^\mu(b/\bar{b} \rightarrow \mu + \text{jet} + X)$. Shown for each p_T^μ bin are the fraction of muons in the data sample due to W/Z -decays, asa well as $f_b = b/(b + c + \pi/K)$ from the p_T^{REL} fits and the muon spectrum associated with $b/\bar{b} \rightarrow \mu X$ decays.	126
9.4 Uncertainty in theory prediction of $d\sigma/dp_T^\mu(b\bar{b}/ \rightarrow \mu X)$	127
10.1 The unsmeearing factor $f_u = (d\sigma/dp_T^\mu)^{\text{true}} / (d\sigma/dp_T^\mu)^{\text{reco}}$ and its uncertainties, and the unsmeared muon differential cross section.	133
10.2 Conversion of the differential muon cross section into the b -quark production cross section	138
11.1 The $b \rightarrow \mu + \text{jet} + X$ and b quark cross section after correction for resolution and background effects	145
11.2 Ratio data/central NDE theory prediction for DØ data at $\sqrt{s} = 1.8 \text{ TeV}$ and UA1 data at $\sqrt{s} = 0.63 \text{ TeV}$	147

Chapter 1

Overview

The Tevatron Collider at the Fermilab National Accelerator Laboratory provides the highest energy particle collisions in the world. Protons (p) and antiprotons (\bar{p}) are collided at a center of mass energy of 1.8 TeV and studied with two general purpose collider detectors, DØ and CDF. The analysis of these collisions is used to test the Standard Model of elementary particles and forces and to look for new phenomena beyond the scope of this model.

The Standard Model, currently the best description of subnuclear matter and its interactions, encompasses the strong force, (described by the theory of quantum chromodynamics, QCD) and the electromagnetic and weak forces (described by the unified electroweak force theory). It hypothesizes that all matter is made up from different combinations of 12 fundamental particles (6 quarks and 6 leptons) and their antiparticles. The quarks form 3 doublets of increasing mass. The first of these contains the stable up (u) and down (d) quarks, from which protons and neutrons are built. Production of the charm (c) and strange (s) quarks, which form the second doublet, and of the

bottom (b) quark, which is in the third doublet, has been observed in both electron-positron and hadron collisions [1]. The existence of the top (t) quark, the predicted partner to the b -quark, has recently been established by the D \emptyset and CDF experiments at Fermilab [2, 3].

In QCD nucleons are composed of point-like particles, quarks and gluons, which are collectively referred to as “partons”. The strength of an interaction between partons is specified by the strong coupling constant, α_s , which decreases with increasing four-momentum transfer (Q^2). Cross sections in QCD cannot be calculated exactly, and are commonly expressed as perturbative expansions in α_s . These expansions converge if α_s is sufficiently small, which typically requires $Q^2 > \text{few GeV}^2$. Cross-sections for high Q^2 parton-parton interactions at high energies can thus be reliably calculated in QCD, while interactions at lower Q^2 are described with less precise, phenomenological models.

At the Tevatron center-of-mass energy of $\sqrt{s} = 1.8 \text{ TeV}$, high Q^2 collisions occur with relatively large cross sections allowing significant tests of QCD predictions. In particular, perturbative QCD can be used to calculate the production rate of the heaviest quarks, bottom and top. The applicability of perturbative QCD to charm and lighter quarks is questionable because of the small quark masses.

The UA1 experiment at the CERN proton-antiproton collider was the first to observe b -production in strong interactions and to measured the cross section. The measured transverse momentum cross section for b -quark production was found to be in good agreement with QCD predictions in shape,

but was a factor of 1.5 to 2 higher [4] than the prediction. Subsequent measurements of the same quantity by the CDF collaboration at $\sqrt{s} = 1.8 \text{ TeV}$, are also a factor of about 2 to 3 higher than predictions [5, 6].

The study of b -quark production is important not only as a test of QCD, but also because knowledge of the cross section is required for understanding backgrounds to top-quark signals and in the search for supersymmetric particles and other particles beyond the scope of the Standard Model. It is also relevant to the planning of future experiments at high energy colliders such as such as the upgraded Tevatron [7] or the Large Hadron Collider (LHC) at CERN [8].

This thesis describes a measurement of b -quark production with the D \emptyset detector at the Fermilab Tevatron collider. D \emptyset is a general purpose collider detector with a special focus on the detection of electrons, muons, and jets. The measurement utilizes of the characteristic signature of a muon and a jet to identify events containing a b or a \bar{b} quark.

Chapter 2 outlines some theoretical considerations relevant to b -quark production. The detector is described in chapter 3, and chapter 4 deals with the triggers used in data taking. Chapter 5 describes the reconstruction program used to determine the momentum and energy of muon and jet candidates in the triggered data sample. The extensive Monte Carlo data set generated for the study of efficiencies and the background contamination of the sample are summarized in chapter 6. Chapters 7 and 8 explain the selection cuts imposed offline which reduce the sample to a data set of about 8000 events enriched in b -production, and the efficiencies associated with the trigger and

the selection cuts, respectively. Chapter 9 describes the extraction of the muon differential cross section for the data sample described in chapter 7 using the efficiencies from chapter 8, and explains the procedure to determine the amount of background in the data sample due to processes other than b -production. Chapter 10 describes the extraction of the b -quark production cross section. The results of this analysis are summarized and compared to other measurements of the b -quark production cross section measurements in chapter 11.

Chapter 2

Heavy Quark Cross-Sections in QCD

This chapter describes the theoretical modelling of b -quark production in hadron collisions. We also describe calculations of the rate of b -quark production, and the problems and uncertainties associated with these calculations.

2.1 Cross Sections and Perturbative QCD

Deep inelastic scattering experiments performed in the 1960's revealed that hadrons are composite objects consisting of pointlike partons [9]. Later partons were identified as quarks and gluons, and their interactions described by QCD, the theory of the strong force.

The strong force is carried by gluons, which are analogous to photons, the carriers of the electromagnetic force. The strong force acts between particles that carry the color charge, which is equivalent to the electric charge in electromagnetism. A major difference between the electromagnetic and strong forces is that the gluons themselves are colored, while photons are electrically

neutral, so that, unlike photons, gluons can interact with each other. A quark constantly radiates and reabsorbs virtual gluons, and is hence surrounded by a “cloud” of gluons, in much the same way as an electron is engulfed in a cloud of virtual photons. However, because of the self-interaction of the gluons, this cloud has an “anti-screening” effect, in contrast to the screening effect of the photon cloud around an electron: The gluon cloud amplifies the color charge of the parton, while the photon cloud around an electron appears to decrease its electric charge. Thus the strength of the strong force increases with distance from the parton. This leads to the phenomenon of confinement - free particles with net color charge are not observed.

On the other hand, since the strong coupling constant α_s becomes small at short distances (high momentum transfer) quarks in high energy collisions act as pseudo-free particles. This property is known as asymptotic freedom and is implicit in QCD. In this regime (interactions of a 4-momentum transfer $Q^2 > \text{few GeV}^2$) we can decompose the proton-antiproton interaction into interactions between partons from the proton and antiproton.

We can separate (factorize) the short distance parton level part of the interaction from the lower Q^2 non-perturbative fragmentation process; the factorization theorem relates the cross-section σ for a particular reaction with parton level cross sections $\hat{\sigma}$ between a parton in each of the interacting hadrons:

$$\sigma = \sum_{ij} \int dx_i dx_j \hat{\sigma}_{ij}(x_i p_A, x_j p_B, \mu, \Lambda) F_i^A(x_i, \mu) F_j^B(x_j, \mu) \quad (2.1)$$

where F_i^A and F_j^B are the structure functions describing the density of partons i and j inside the proton (A) or antiproton (B); x_i and x_j are the correspond-

ing fractions of the total proton (p_A) and anti-proton (p_B) momenta. The structure functions and the momentum scale parameter (Λ) are derived from deep inelastic scattering experiments and evolved to the relevant Q^2 scale (μ) using QCD theory.

The strong coupling constant α_s depends on the 4-momentum exchange (Q^2) of the interaction. In the leading order QCD expansion, α_s is given by

$$\alpha_s(\mu) = \frac{12\pi}{(33 - 2n_f) \ln(\mu^2/\Lambda^2)} \quad (2.2)$$

where the explicit Q^2 dependence is contained in the scale parameter $\mu(Q)$. $\mu(Q)$ is typically chosen to be of the order of momentum transfer in the interaction. Here we adopt the definition $\mu = \sqrt{p_T^2 + m^2}$, where p_T and m are the transverse momentum and the mass of the b -quark, respectively.

Since quarks are confined within hadrons, their masses cannot be measured directly and have to be extracted based on their influence on hadron properties. Consequently, their values depend on the method used for the extraction, as well as the exact definition of the quark mass. A recent calculation within the framework of heavy quark effective theory [10] results in a value of $m_b = 4.74 \pm 0.14 \text{ GeV}/c^2$ [11, 12]

Λ is experimentally determined to be 100-250 MeV[13]; n_f denotes the number of accessible quark flavors, For the center of mass energy of 1.8 TeV, we take $n_f = 5$, rather than 6 because of the large mass of the top quark [2, 3].

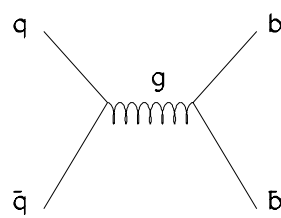
2.2 Heavy Quark Production

For interactions in the realm of asymptotic freedom, heavy quark production cross sections in parton interaction are calculated using a perturbative expansion in α_s :

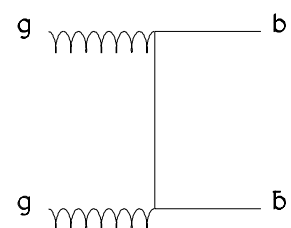
$$\hat{\sigma}_{ij} = \alpha_s^2(\mu) G_{ij}^{LO}(\hat{s}, m_Q) + \alpha_s^3(\mu) G_{ij}^{NLO}(\hat{s}, m_Q) + \dots \quad (2.3)$$

where the coefficients $G_{ij}^{LO}(\hat{s}, m_Q)$ and $G_{ij}^{NLO}(\hat{s}, m_Q)$ depend on the quark mass (m_Q) and the center of mass energy $\sqrt{\hat{s}}$ in the parton system. For the data in this study the momentum transfer is $\approx 30 \text{ GeV}/c$ and hence well into that regime. The μ -dependence of the cross section is the result of terminating the perturbative expansion after a finite number of terms; if it were carried out to infinite order, the result would be independent of μ .

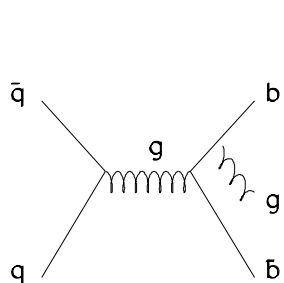
The cross section for heavy quark production is calculated by combining the contributions from the contributing processes. Examples for Feynman diagrams for some of the leading and next-to leading order processes are shown in figure 2.1. The leading order processes (Fig. 2.1a) and b) are often characterized as 2-to-2 processes because two partons in the initial state react to two partons in the final state. Such processes are observed in the detector as two jets which are collinear in the transverse plane because of momentum conservation. The next-to-leading order processes (Fig. 2.1c), d), e) are 2-to-3 processes, having three partons in the final state. Apart from radiative corrections for leading order processes (Fig. 2.1c), the next-to-leading order calculation introduces a new class of processes in which the b -quarks are no longer collinear in the transverse plane. In contrast to leading order, which



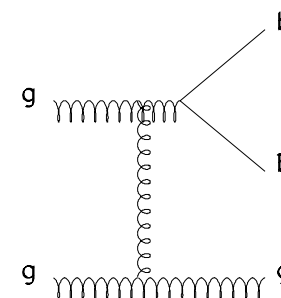
a)



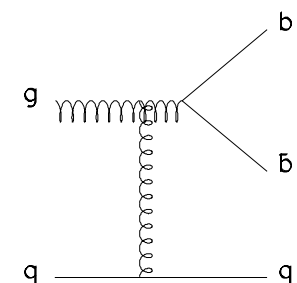
b)



c)



d)



e)

Figure 2.1: Examples of Feynman Diagrams for leading (a and b) and next-to-leading order (c to e) QCD processes for b -production

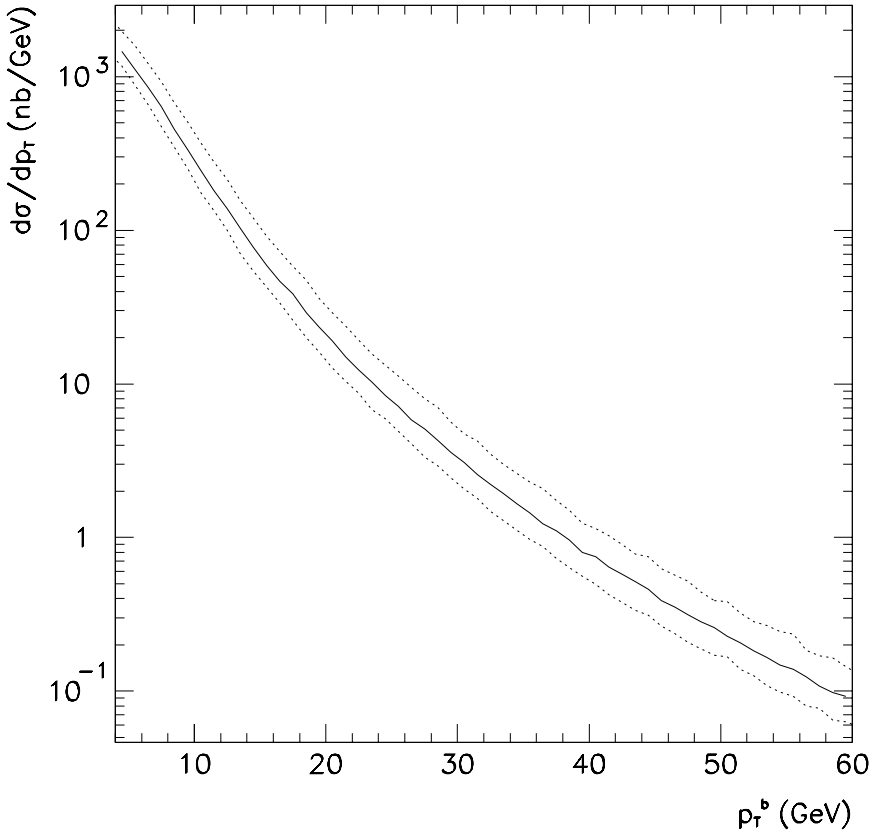


Figure 2.2: b -quark production cross section as a function of the transverse momentum of the quark, for $|y| < 1$, from the NDE calculation [14]. The central value (solid line) is for $\Lambda = 140$ MeV and $\mu = \mu_0$. The dotted lines define the theoretical uncertainty obtained by varying Λ and μ to 187 MeV and $\mu_0/2$ (upper line) versus 100 MeV and $2\mu_0$ (lower line).

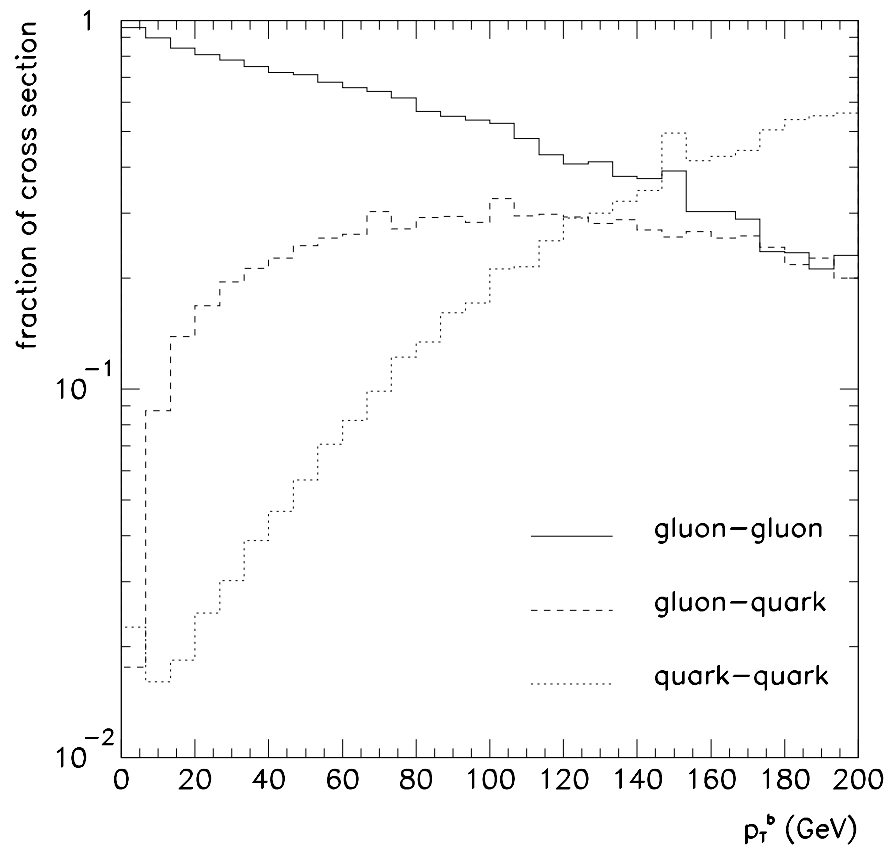


Figure 2.3: Contribution from gluon-gluon, gluon-quark and quark-quark processes to b -quark production.

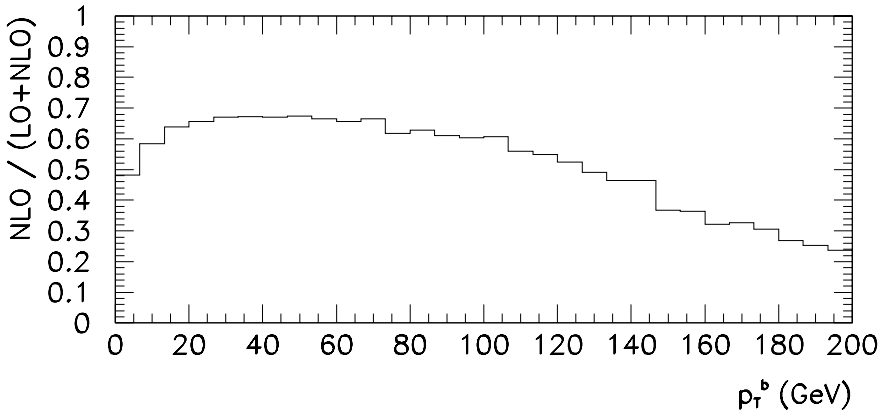


Figure 2.4: Fraction of next-to-leading order contribution to b -production.

can proceed only from gluon-gluon or quark-quark initial states, b -production in next-to-leading order can include gluon-quark initial states (Fig. 2.1 e).

Cross sections for b and c -quark production have been calculated by Nason, Dawson and Ellis (NDE) [14] and Beenakker *et al.* [15] to next-to-leading order; both calculations agree very well. The convergence of the perturbation series is however questionable for the c -quark because of its small mass ($m_c \approx 1.8 \text{ GeV}/c^2$). We have used the NDE calculation as implemented by M. Mangano [16]. For this analysis we are using Monte Carlo program implementation by M. Mangano which uses the NDE calculation. Figure 2.2 shows the resulting cross section for b -quark production as a function of the quark transverse momentum, for a rapidity range of $|y| < 1$. The calculation uses the MRSD0 structure function parameterization of Martin, Roberts and Stirling [17] with $\Lambda = 140 \text{ MeV}$ and a central value for μ of $\mu_0 = \sqrt{p_T^2 + m^2}$,

where m denotes the mass of the b -quark ($m_b = 4.74 \pm 0.14 \text{ GeV}/c^2$). The uncertainty in the calculation has been estimated by varying Λ between 187 and 100 MeV and varying μ between $\mu_0/2$ and $2\mu_0$. The range in Λ reflects the result of $\Lambda = 140^{+47}_{-40} \text{ MeV}$ obtained by MRS from the analysis of deep inelastic scattering data [17]. The variation in μ reflects the best current estimate of the uncertainty in the choice of the scale parameter. To obtain the uncertainty for the b -quark production cross section, we vary Λ and μ in a way as to maximize the error. The upper edge of the error band corresponds to $\Lambda = 187 \text{ MeV}$ and $\mu = \mu_0/2$, while the lower edge corresponds to $\Lambda = 100 \text{ MeV}$ and $\mu = 2\mu_0$. These variations in parameters result in an overestimate of the uncertainty since μ and Λ are partially correlated. They change the overall normalization of the spectrum by about $\pm 60\%$, but do not effect its shape.

Figure 2.3 shows the decomposition of the cross-section into the contributions from gluon-gluon, gluon-quark and quark-quark initial states. The gluon-gluon processes dominate in the low transverse momentum region, while quark-quark processes dominate at the highest transverse momenta. Fig. 2.4 shows the relative contribution of next-to-leading order processes to the b -production cross-section. At high p_T^b most of the cross section is due to leading order production, reflecting the dominance of the quark-quark processes. The constituent partons involved in high p_T processes are predominantly quarks, which on average carry a higher nucleon momentum fraction than gluons, and in addition $q\bar{q}$ -processes have quite small a cross section for next-to-leading order processes.

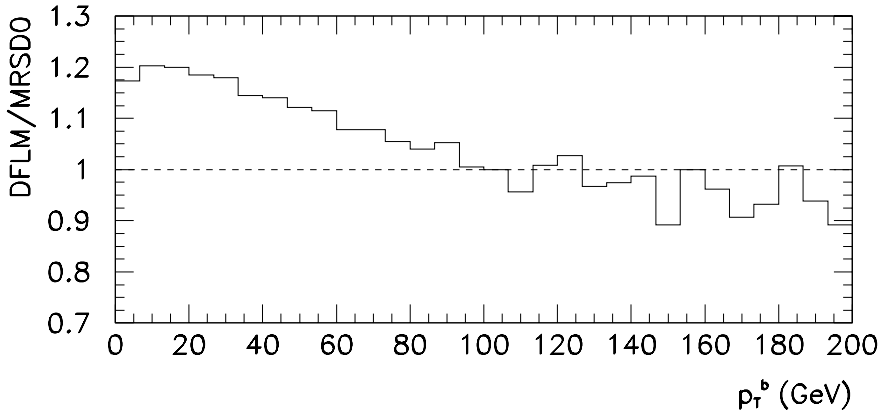


Figure 2.5: Ratio of b -quark production cross section obtained with DFLM/MRSD0 structure functions.

Figure 2.5 shows the effect of the structure functions on the cross section calculation. Replacing the MRSD0 [17] structure functions by the DFLM parameterization [18] causes a change of up to 20% in the cross section. The DFLM parameterization predates MRSD0 and does not make use of the same wealth of deep inelastic scattering data, but it was extracted independently and was hence chosen for this comparison. Note that the change in structure function affects primarily the lower end of the p_T spectrum. This is expected since, for low p_T (and low values of x) gluons dominate, and since gluon distributions are more difficult to extract from deep inelastic scattering data than quark distributions. They are hence more uncertain than quark distributions and vary significantly more between structure function parameterizations. Finally, the QCD cross-section depends on the value of the b -quark

mass, $m_b = 4.74 \pm 0.14 \text{ GeV}/c^2$ [11, 12]. The effect on the prediction of the b -quark production cross section is greatest near threshold, i.e. at low values of p_T^b . The systematic error in the b -production cross-section due to the above 0.14 GeV/c^2 uncertainty in m_b varies from $\approx 5\%$ for $p_T^b = 10 \text{ GeV}/c$ to $\approx 2\%$ for $p_T^b > 20 \text{ GeV}/c$.

2.3 Summary

We have outlined the QCD based calculations of bottom quark production in hadron colliders and estimated the errors associated with those calculations. Uncertainties in the parameters μ and Λ result in a 60% uncertainty in $d\sigma/dp_T^b$, while uncertainties in parton densities in the colliding hadrons contribute an additional 20% error. The uncertainty in the mass of the b -quark adds another 2-5%. At the conclusion of this study we will return to these predictions and confront them with our measurement of b -quark production cross section.

Chapter 3

The Apparatus

3.1 The Fermilab Accelerator Complex

3.1.1 $p\bar{p}$ -Production

The Fermilab Tevatron accelerator produces protons and anti-protons with an energy of 900 GeV each. $p\bar{p}$ colliders have the advantage that both proton and antiproton beams can travel in the same accelerator in opposite direction, but this convenience comes at the expense of a much more involved procedure of antiproton production. The acceleration of the particles proceeds in several steps through a series of accelerators described below. The layout of the accelerator complex is shown in figure 3.1.

Both the proton and the antiproton beam start out as H^- ions produced in a magnetron surface plasma source. The ions are produced from the interaction of electrons in the plasma with Cesium atoms coating the cathode of the

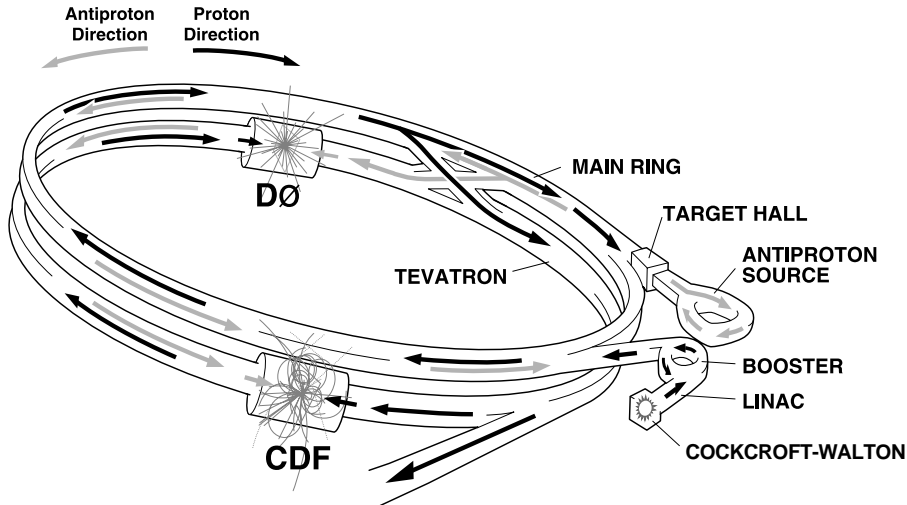


Figure 3.1: An overview of the Fermilab accelerator complex with the $D\bar{\Omega}$ and CDF detectors.

plasma source. The H^- ions escape the plasma chamber through an aperture and are electrostatically accelerated to 18 keV.

The next stage of the acceleration process is a an electrostatic accelerating column increasing the energy of the hydrogen atoms to 750 keV. The energy of an electrostatic accelerator is limited by the maximal input voltage. The next step of the acceleration process is the linear accelerator that accelerates the ions to 200 MeV through a series of drift tubes, separated by a gap. An RF potential is applied to drift tubes in such a way that the particles are accelerated by the field in the gap between the tubes and are shielded inside the drift tubes from the decelerating field. The length of the drift

tubes is increasing throughout the 500 ft of the linear accelerator to match the increasing velocity of the ions.

At 200 MeV the ions are well relativistic such that they can be further accelerated in a synchrotron, a circular accelerator where the particles are accelerated by multiple passes through a circular arrangement of drift tubes. While the accelerating field is produced by an RF frequency, the bending and focusing of the beam is accomplished with dipole and quadrupole magnets, respectively. The "Booster" synchrotron, the first in a series of three synchrotrons has a radius of 75m and accelerates the protons to 8 GeV.

The next step of the accelerator is the "main ring" of radius 1km that further accelerates the protons to 150 GeV. At that energy the particles are transferred to the Tevatron which has the same radius as the main ring, but is equipped with superconducting magnets, and hence produces stronger magnetic fields for bending of the beam than the main ring which is equipped with conventional magnets. There the protons are accelerated to their final energy of 900 GeV.

Antiprotons are produced by extracting a fraction of the protons from the main ring, which operates at 120 GeV for antiproton production, and steering them to a nickel target. The secondary particles are focused with a lithium lens and antiprotons of \approx 8 GeV are magnetically selected and transferred into the debuncher where the momentum spread of the particles is reduced to 0.2% (from 4% out of the lithium lens). The process is called stochastic cooling. Because of the low yield of antiprotons (one for every 10^5 protons), the antiprotons are stored in the antiproton accumulator until a sufficient number

of antiprotons are produced. That process takes about 5 hours. At that time the antiprotons are transferred into the Main ring, accelerated to 150 GeV and are then transferred into the Tevatron.

Protons and antiprotons in the Tevatron are distributed among six p and \bar{p} bunches, each 30 cm long. Proton bunches contain $\approx 100 \times 10^9$ particles each while antiproton bunches are about half that size. The counterrotating bunches remain in the Tevatron for a “store”-duration of 12-18 hours. during that time the main ring continues to operate to replenish the antiproton supply.

Since there are 6 bunches in each of the counterrotating beams, the bunches pass each other at six spots along the ring. Detectors are installed at three of these, at the remaining ones the proton and antiproton beams are separated to avoid losses due to collisions between particles. In the collision regions where detectors are installed, the transverse beam spot size is reduced through additional quadrupole magnets on either side of the detector to $\sigma_{xy} = 40 \mu\text{m}$, which increases the probability of a $p\bar{p}$ interaction.

The beam spot size in the transverse plane is small compared to the resolutions of the detector, its size is, however, included as an error in the determination of the muon momentum (section 5.3). Because of the 30 cm longitudinal size of the beam spot, the z position of the interaction vertex is directly measured using the central drift chamber (section 5.2).

3.1.2 Luminosity

The reaction rate R for a given process is given by

$$R = \sigma \mathcal{L} \quad (3.1)$$

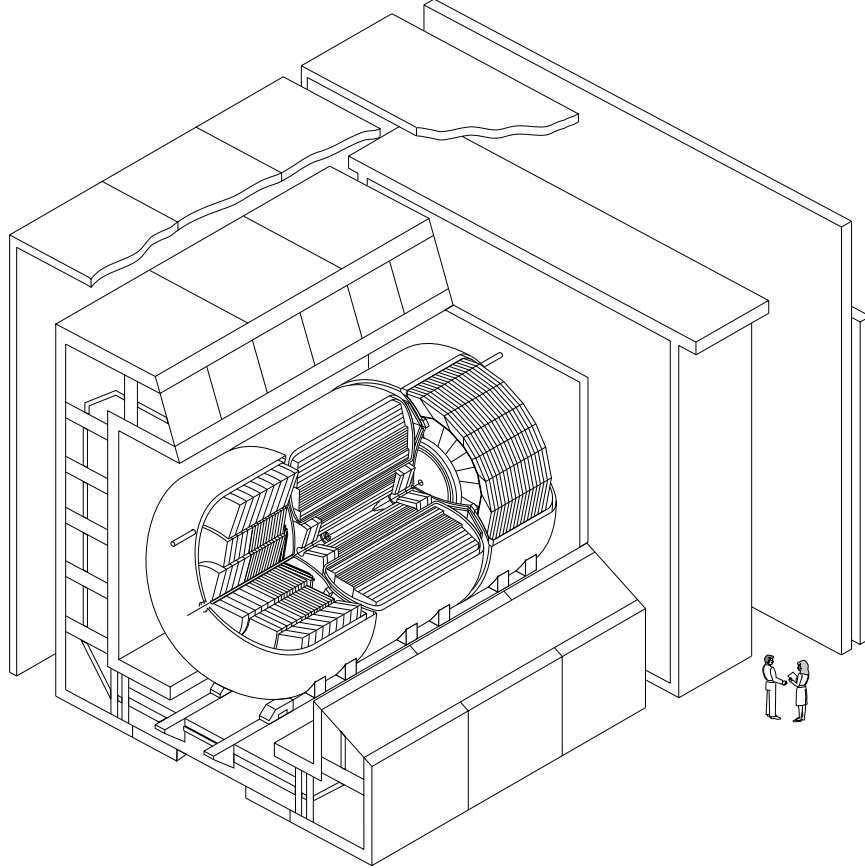
where σ is the cross section for the process and \mathcal{L} is the instantaneous luminosity. The cross section is a property of the physics process and the luminosity is a parameter of the accelerator. For two oppositely directed beams of relativistic particles, the luminosity is given by

$$\mathcal{L} = f n \frac{N_1 N_2}{A} \quad (3.2)$$

where N_1 and N_2 are the number of particles in each of the p and \bar{p} bunches, n is the number of bunches (6), f is the revolution frequency. A denotes the cross sectional area of the colliding beams, assuming them to completely overlap.

The determination of the instantaneous luminosity is based on data from the level 0 (L0) hodoscope (section 4.4). The cross section "visible" to the L0 detector, a combination of the measured inelastic, single diffractive and double diffractive cross sections, and the efficiency of the detector, is 48.2 ± 5.2 mb [21]. The cross section measurements for the inelastic, single diffractive and double diffractive cross sections are obtained from averaged measurements with the CDF [19] and E710 [20] detectors.

The instantaneous luminosity is then obtained from equation 3.2, with R being the count rate of the L0 detector. Instantaneous luminosities for the data used in this analysis are in the range of $1 - 3 \cdot 10^{30} \text{ cm}^{-2}\text{s}^{-1}$.



DØ Detector

Figure 3.2: An isometric cut-away view of the DØ detector.

3.2 An Overview of the DØ Detector

The DØ detector is a general purpose high energy particle physics facility for the study of high p_T -phenomena in $p\bar{p}$ -collisions at a center of mass energy of $\sqrt{s} = 1.8 \text{ TeV}$. The design has been optimised for charged lepton and jet energy measurements coupled to excellent hermiticity for missing energy measurements.

Figure 3.2 shows a cutaway view of the detector. It is 13 m high, 13 m wide and 20 m along the beam direction, with an overall mass of over 5000 metric tons. The figure shows the concentric layers of sub-detectors that make up the D \emptyset detector. Innermost is the central tracking system which consists a vertex drift chamber, a transition radiation detector and drift chambers which cover central and forward regions. This is surrounded by the Uranium liquid-Argon calorimeters which are located in three cryostats. The outermost part of the system is the muon spectrometer which consists of three layers of proportional drift tube chambers, with a toroidal magnetic field of 2 T between the first and second layer.

The detectors that are used in this analysis are discussed in more detail in the following paragraphs. Further details as well as a description of the electronics, the monitoring and control software, and the mechanical support structure can be found in ref. [22].

D \emptyset uses a right handed coordinate system with the y -axis vertically upwards and the z -axis pointing in the proton direction (South). The radius vector R and the polar and azimuthal angles θ and ϕ denote the usual spherical coordinates, while r denotes the projection of the polar radius vector R on the (transverse) xy -plane. The location of a particle in the detector is often expressed in terms of pseudorapidity $\eta = -\ln(\tan(\theta/2))$, which approximates the true rapidity $y = 1/2 \ln((E + p_z)/(E - p_z))$ in the limit $\beta \rightarrow 1$. The geometrical center of the detector is the origin of the coordinate system.

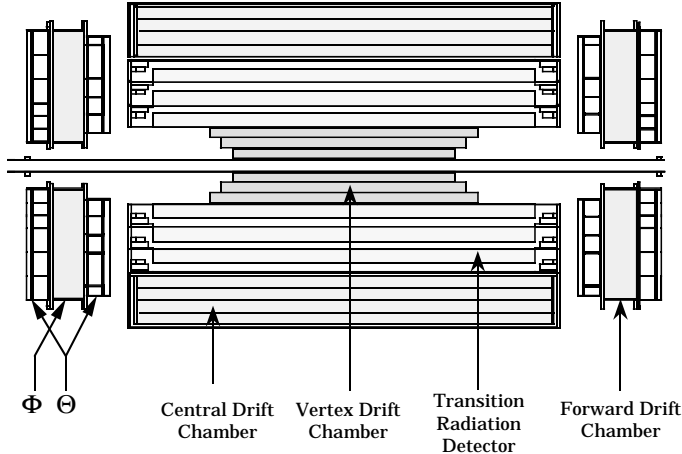


Figure 3.3: A cross section of the DØ central detectors

3.3 Central Detectors

The central detectors of DØ consist of the vertex drift chamber (VTX), the transition radiation detector (TRD), the central drift chambers (CDC) and the two forward drift chambers (FDCs). Fig 3.3 shows the arrangement of these detectors.

The VTX, TRD, and CDC form concentric cylinders, while the two FDCs are arranged perpendicular to the beam. The complete set of central detectors fits in the inner cylindrical aperture of the calorimeter in a volume bounded by $r = 78$ cm and $z = \pm 135$ cm.

3.3.1 The Vertex Drift Chamber

The vertex drift chamber begins just outside the Beryllium beam pipe at $r = 3.7$ cm and extends out to $r = 16.2$ cm with a maximum length of 116.8 cm. It consists of 3 concentric layers of cells, the innermost layer contains 16 cells,

the other layers have 32 cells. Additional wires are included for field shaping. The VTX operates with $\text{CO}_2(95\%) - \text{ethane}(5\%) - \text{H}_2\text{O}(0.5\%)$ gas mixture at one atmosphere. The electric field has a strength of about 1kV/cm .

3.3.2 The Central Drift Chamber

The central drift chamber (CDC) is located between the TRD and the calorimeter. It extends in radius from 49.5 to 74.5 cm and has a length of 184 cm. It consists of 4 concentric rings of 32 azimuthal cells per ring. Each cell contains seven gold-plated tungsten sense wires of $30\text{ }\mu\text{m}$ diameter parallel to the beam line and two delay lines embedded in the cell walls just before the first and after the last sense wire as shown in figure 3.4. Also shown are the guard wires for field shaping on either side of the sense wires. The CDC is operated with $\text{Ar}(92.5\%) \text{CH}_4(4\%) \text{CO}_2(3\%)$ with $0.5\% \text{ H}_2\text{O}$ at 1 atm with a potential of 1.5 kV on the sense wires.

The delay lines propagate pulses induced from the nearest sense wire to both ends of the cell where a measurement of the difference of arrival time gives the location of the charged particle's trajectory along the z -coordinate. In cosmic ray tests fits using information from delay lines from all four layers of chambers show a resolution of about $\sigma_z = 2\text{ mm}$. The spacial resolution for fitted tracks in the drift plane was found to be about $150\text{ }\mu\text{m}$ [23].

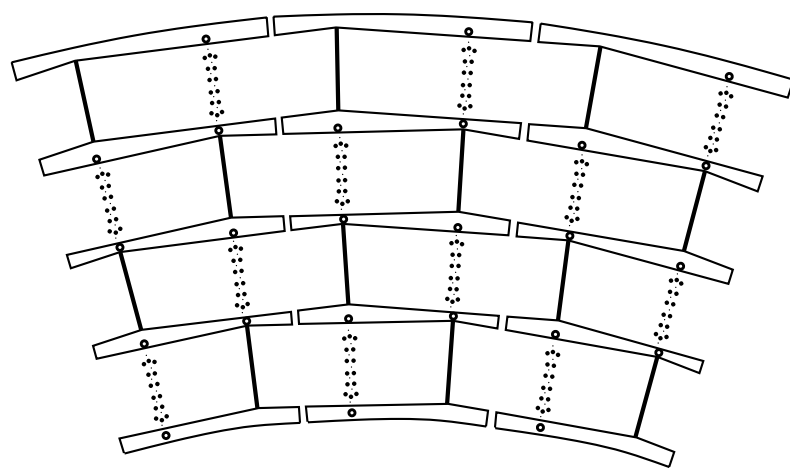


Figure 3.4: End-view of the central drift chamber, shown are the 7 sense wires per cell as well as the delay-lines embedded in the walls of the cells. There are guard wires for field-shaping on either side of the sense wires.

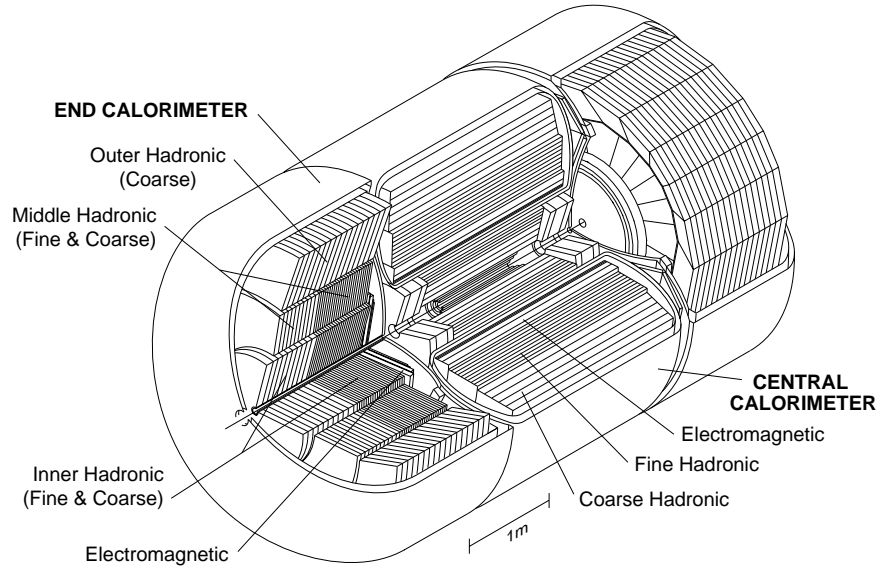


Figure 3.5: The DØ calorimeters, showing the central and the two end-cryostats and the various calorimeter subsystems.

3.4 Calorimeter

3.4.1 Overview and Design

The calorimeter is contained in three separate cryostats. The middle cryostat contains the central calorimeter (CC), and covers the region $|\eta| < 0.8$, while the two outer cryostats contain the end calorimeters (ECs) which extend the coverage to $|\eta| \approx 4.0$ (Fig. 3.5).

The calorimetry is of a sampling design with depleted uranium, copper and stainless steel as the absorbing materials and liquid argon as the active material. The basic structure of the calorimeter is a succession of layers, each

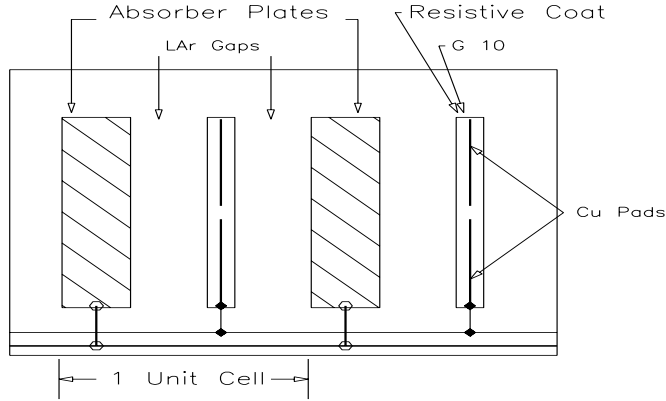


Figure 3.6: A schematic of the calorimeter cell structure.

consisting of an absorber material followed by a 2.3 mm liquid argon gap on either side of a 1.3 mm signal board. The signal board contains copper pads surrounded by a resistive coating (Fig. 3.6). The absorber and the copper pads are grounded while the resistive coating is connected to a high voltage source to create an electric field of about 9 kV/cm across the liquid argon gap. An electron or hadron travelling through the calorimeter will interact with nuclei of the absorber material creating a shower of particles which ionizes the liquid argon. The electrons thus liberated drift toward the signal board and induce a charge on the copper pads. The copper pads in different layers are aligned such that their centers lie on a ray originating at the center of the detector. The pads located on the same ray form a readout tower.

The transverse segmentation of the calorimeter is determined by the size of the readout towers which is 0.1×0.1 in $\Delta\eta \times \Delta\phi$ for $|\eta| < 3.2$. This is fine

enough to probe the transverse shape of a jet, which is typically about $\Delta R = \sqrt{(\Delta\eta)^2 + (\Delta\phi)^2} = 0.5$ in extent. In the very forward region, $3.2 < |\eta| < 4.0$, the segmentation is 0.2×0.2 , because the physical shower size in that region is much wider in $\eta - \phi$ space than in the central region.

The longitudinal segmentation is determined by the number of successive pads at different depth in the calorimeter that are read out together or “ganged”, forming a readout-layer.

Looking from the beam axis outwards, the D \emptyset calorimeter consists of a thin electromagnetic followed by a thicker hadronic one (Fig. 3.5). The electromagnetic calorimeter uses 0.3 cm thick uranium plates in both the central and forward calorimeter. It has a total thickness about 20 radiation lengths (X_0) grouped into four readout-layers. The segmentation is 0.1×0.1 in $\Delta\eta \times \Delta\phi$, except for the third readout-layer which spans the radial region of maximum electromagnetic energy deposition, where the segmentation is increased to 0.05×0.05 . This allows a more precise determination of the direction of photons and electrons.

The hadronic section uses uranium, copper and stainless steel plates of thickness between 0.6 cm (innermost layers) and 4.6 cm (outermost layers). The region with fine segmentation is used for hadronic shower-shape measurements and the thick absorber region is used for shower-containment of energetic jets. The total thickness of the hadronic calorimeters is about 6 interaction lengths in the central and about 9 interaction lengths in the forward calorimeter.

3.4.2 Calorimeter Performance

Before its installation at the DØ site the performance of the calorimeter modules was studied extensively in testbeams using electron and pion beams of known energy to determine sampling fractions, energy resolution and response functions [24].

The sampling fraction is the fraction of the energy deposited in the calorimeter that is detected. In a sampling calorimeter most of the energy is dissipated in the absorber and does not lead to any ionization of the liquid argon; the energy measured by the calorimeter is scaled by the 1/ (sampling fraction) to give the incident energy of the particle. The sampling fraction varies among the subsystems of the calorimeter and ranges from about 12% in the electromagnetic calorimeters to about 1.5% for the outermost layers of the hadronic calorimeters.

Figure 3.7 shows the calorimeter response function

$$\mathcal{R} = (E_{\text{measured}} - E_{\text{beam}})/E_{\text{beam}} \quad (3.3)$$

for electrons and pions as a function of the particle energy. Also shown are the deviations from linearity for both electrons and pions [25]. We observe excellent linearity with a response ratio for electrons and pions (e/π -ratio) varying between 1.11 for 10 GeV/c to 1.04 at 150 GeV/c.

The energy resolution, σ , of a sampling calorimeter can be parameterized as

$$\left(\frac{\sigma}{E}\right)^2 = C^2 + \frac{S^2}{E} + \frac{N^2}{E^2} \quad (3.4)$$

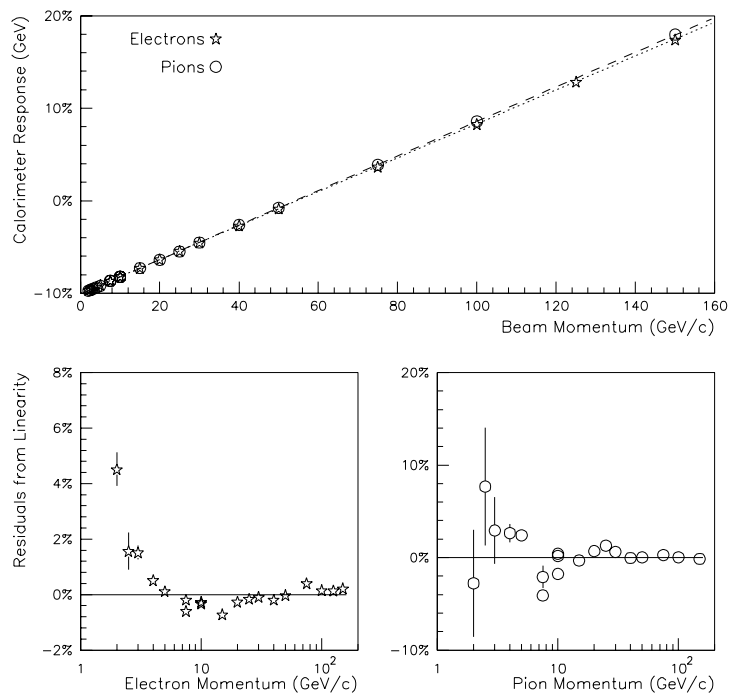


Figure 3.7: Calorimeter response for electrons and pions of known energy in the testbeam (top). The bottom plots show the residuals (deviations) from linearity for electrons and pions.

where E is the energy of the incident particle. C is a constant term embodying uncertainties in the test beam momentum and variations in the thickness of the liquid argon layers, S reflects the uncertainty in the sampling fractions and N is a noise term primarily due to the radioactivity of the uranium absorber. Typical values for electrons are 0.003 ± 0.002 , $(0.157 \pm 0.005)\sqrt{\text{GeV}}$ and 0.140 GeV for C , S and N respectively. For a 50 GeV electron, $\sigma/E \approx 0.02$. For pions the energy resolution is coarser, with values for C , S and N of 0.032 ± 0.004 , $0.41 \pm 0.04\sqrt{\text{GeV}}$ and 1.28 GeV for C , S and N respectively. For a 50 GeV pion, $\sigma/E \approx 0.06$.

3.5 The Muon Detector

The Wide Angle MUon Spectrometer (WAMUS) contains three solid-iron toroidal magnets of square cross-section and about 1 m thick. The magnetic field is about 2 Tesla strong with field lines running in the plane perpendicular to the beam axis. The central magnet (CF) covers the pseudorapidity region $|\eta| < 1.0$, the north and south end toroids (EFN, EFS) extend the coverage to $|\eta| = 1.7$. The Small Angle MUon Spectrometer (SAMUS) which was not used in this study, is described elsewhere [26, 27].

The WAMUS magnets are instrumented with three layers of proportional drift tubes. The innermost layer (A-layer) is located at the inner face of each magnet and the other two layers (B,C) which are separated by about 1 m, are located outside of the magnets. Figure 3.8 shows a schematic of the WAMUS and SAMUS spectrometers.

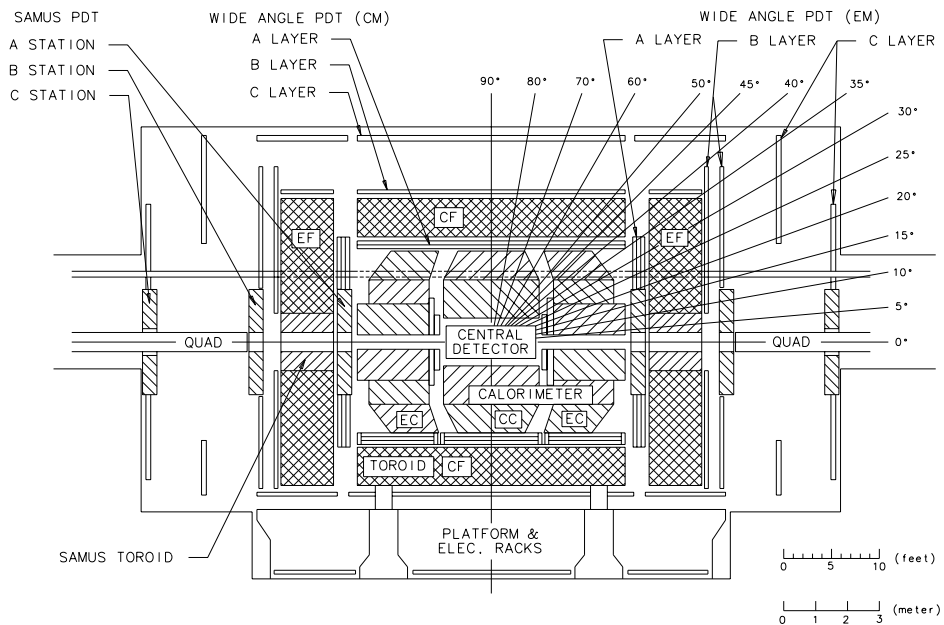


Figure 3.8: Elevation view of the DØ detector showing the three layers of proportional drift tubes of the muon system and the toroidal magnet. The "main ring" is passing through the detector ≈ 1 m above the Tevatron beam pipe.

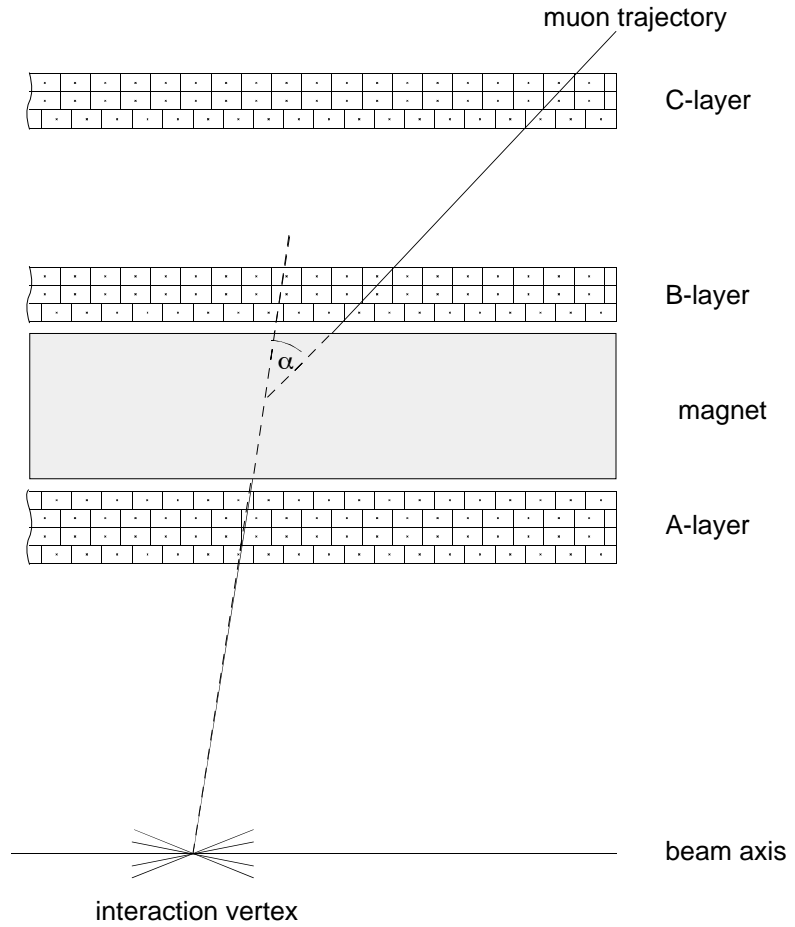


Figure 3.9: Schematic drawing of a muon magnetic spectrometer.

The principle of momentum measurement in the DØ magnetic spectrometer is shown in fig. 3.9. It is a schematic depiction of a section of the muon system, showing the three layers of proportional drift tubes and the magnet between the A and B layers. Individual drift tubes are shown with the wires transverse to the plane of the figure. The B and C layers consist of three sublayers of drift tubes, also referred to as planes, while the A layer has 4 planes.

The magnetic field lines are parallel to the wires such that a muon created at the center of the detector is deflected predominantly in the plane of the figure. The projection of the muon system shown in figure 3.9 is hence called the “bend view”, while the orthogonal projection in the plane perpendicular to the beam-pipe is referred to as the “non-bend” view.

The direction of the muon before the magnet is determined from the A-layer drift tubes, and the direction after the magnet is determined from the B and C-layers. Assuming a constant magnetic field strength of magnitude B (measured in Tesla), the momentum p (in GeV/c) of the muon is given by:

$$p = \frac{0.3 B d}{\sin \alpha} \quad (3.5)$$

where d is the thickness of the magnet in meters, and α is the deflection angle in the muon’s trajectory.

Over most of its coverage, the outermost two layers of the muon system are shielded by more than twelve interaction length of material, about half of which is provided by the calorimeter and the rest by the muon toroids (Fig 3.10). This reduces background from non-interacting hadrons and jets not fully contained in the calorimeter (punchthrough) to less than 0.1% of the muon rate. (These results were obtained from a simulation of high p_T jets in the calorimeter[28, 29]. The low punchthrough rate allows the identification of clean muon signals even when the muons are inside a high E_T -jet.

Each of the more than 11,000 drift tubes in the Wide Angle Muon System is 10 cm wide, 6 cm high and between 2 and 6 m long. A cross-section of a drift tube is shown in fig. 3.11. The cell walls are aluminum and each cell

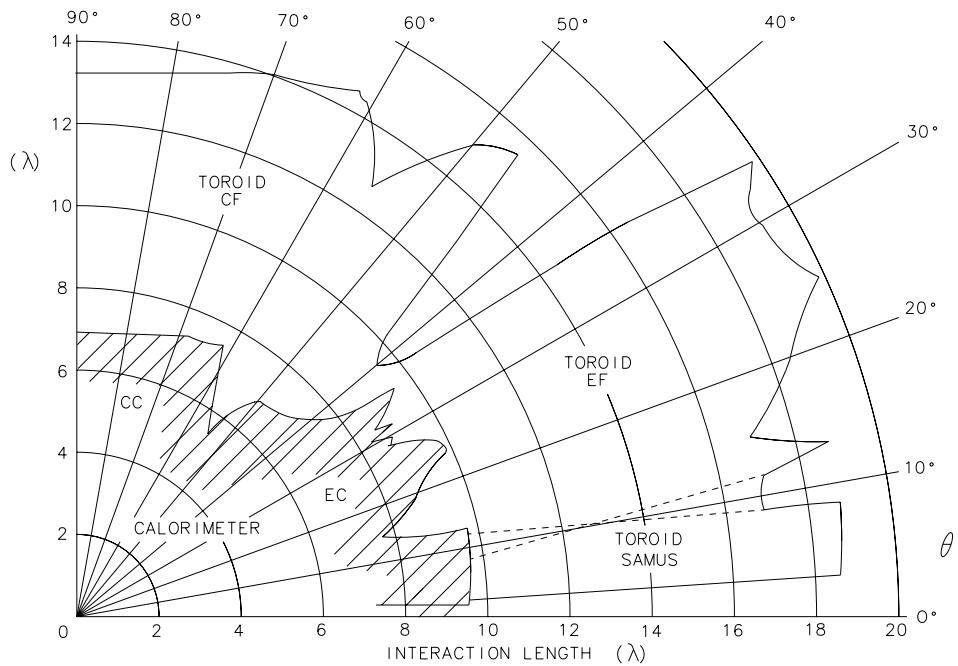


Figure 3.10: Number of interaction lengths in the $D\emptyset$ detector as a function of polar angle. The dip at 40° is due to the gap between the CF and EF magnet toroids.

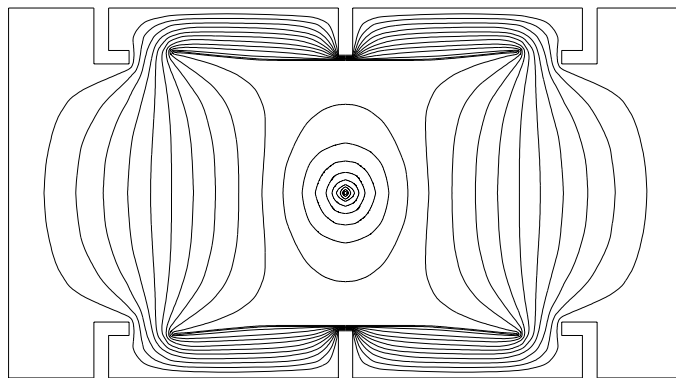


Fig. 4 ELECTROSTATIC EQUI-POTENTIAL LINES OF 4" PDT CELL
SIGNAL WIRE AT +5 KV, AND VERNIER PADS AT +2 KV

Figure 3.11: Cross section of a drift tube, showing the equipotential lines and the cathode pads on the top and bottom of the cell.

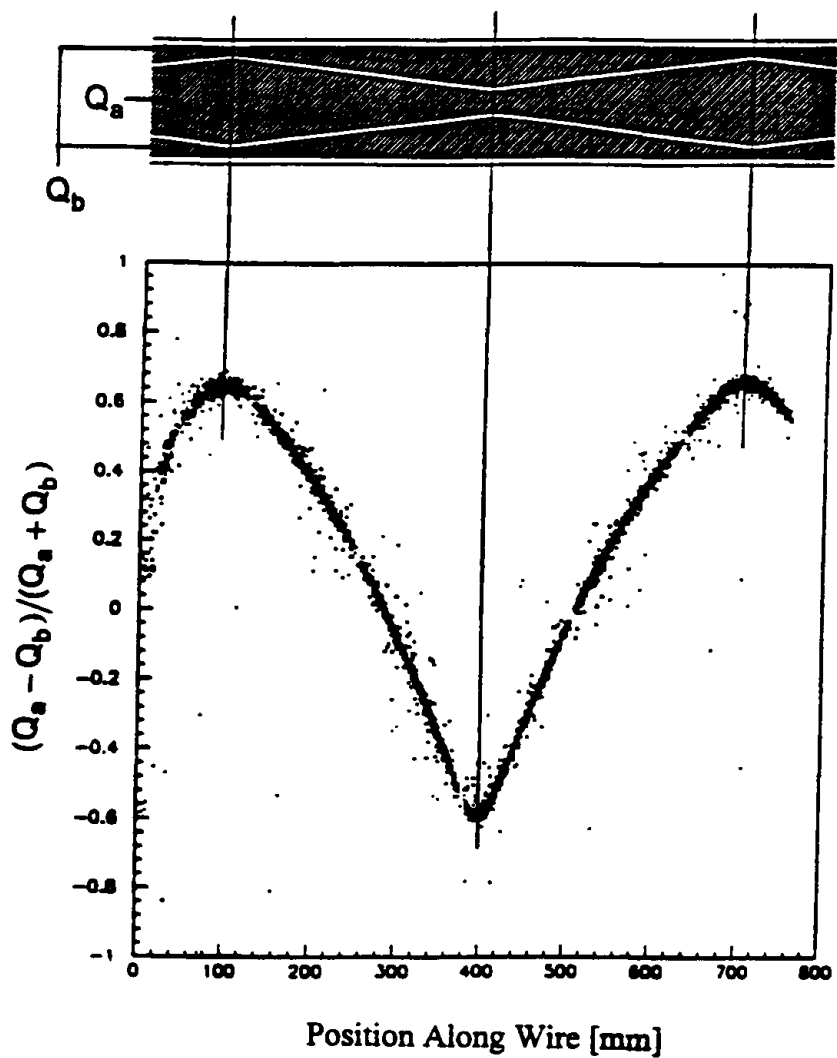


Figure 3.12: Cathode pad showing the inner and outer sections divided by a repeating diamond pattern. Below is a plot of the ratio of difference and sum of the charged induced on the inner and outer sections of the pads versus the position of the hit along the wire.

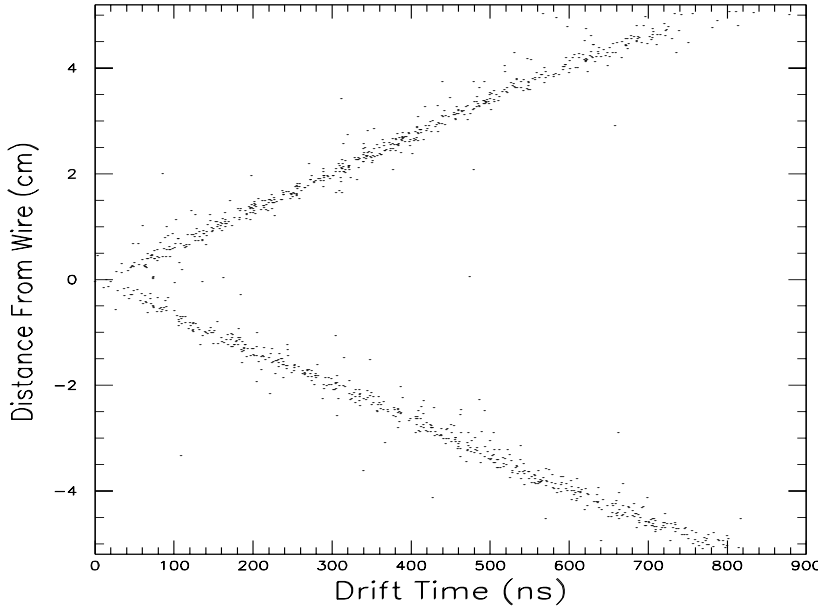


Figure 3.13: Distance of muon trajectory from the sense wire versus drift time.

contains a gold plated tungsten anode wire at the center. The wires from two adjacent tubes are electrically connected (“jumpered”) at one end and the readout electronics for both wires is located at the opposite end.

Cathode pads are installed at the top and bottom of each cell. Each pad is a copper coated insulator with the copper coating divided into an inner and outer region by a repeating insulating diamond pattern as shown in fig. 3.12. Each “diamond” is about 61 cm long. The drift tubes are operated with the gas mixture Ar(90%)CF₄(5%)CO₂(5%) at atmospheric pressure. The aluminum cell walls are grounded, the anode wires are kept at +4.6 kV while the pad pattern is at +2.3 kV.

A muon passing through the drift tube ionizes some of the gas molecules. The liberated electrons then drift towards the sense wire and create an avalanche near the wire, where the electric field is strongest. This results in a pulse, also referred to as a hit, on the wire and induces an image charge on the copper pads.

A coarse estimate of the hit coordinate along the wire (non-bend view) is made from the difference in arrival time (ΔT) of the pulse at each end of the jumpered anode wires. The spatial resolution was measured using a set of proportional wire counters to define cosmic ray tracks in the drift tubes [30]. The resolution for the ΔT -measurement is between 9 and 23 cm depending on the location of the hit along the wire.

Finer resolution in the non-bend view is obtained using information from the cathode pads. Depending on the position of the hit in the diamond pattern, the image charge is divided in different proportions between the outer and inner regions of the pad. The inner regions on the top and bottom pads are electrically connected and the charge deposition on it, Q_a , is read out independently from the charge deposition of the two outer pad-regions Q_b on the top and bottom of the cell. The ratio of the sum and difference of inner and outer signals, $(Q_a - Q_b)/(Q_a + Q_b)$ determines the position of the hit in the direction along the wire, modulo the half lengths of the diamond pattern (Fig. 3.12). The ΔT measurement described above provides the pointer to the correct section of the diamond pattern. The cathode pad patterns in adjacent planes of drift-tubes are shifted to help resolve ambiguities. This measurement improves the position resolution to about 1.6 mm

The muon trajectory perpendicular to the wires (bend view) is obtained from the drift time T , i.e. from the time difference between the muon passing through the chamber and the arrival of the corresponding pulse on the wire. The muon chambers were calibrated with cosmic ray muons. A muon chamber was placed between two sets of proportional wire counters and scintillators to define the trajectory and time of passage of the muon. Fig. 3.13 shows the relationship between drift time the drift distance [31]. The data from a single cell does not tell us on which side of the wire the muon passed. In order to resolve this “left-right ambiguity”, cells in different planes are staggered by a fraction of their widths. By combining information from several planes the ambiguity is resolved. The position resolution in the bend view is 0.3 mm.

The momentum resolution can be parameterized as $\Delta(1/p) = ((A/p)^2 + B^2)^{1/2}$ where $A = 0.18 \pm 0.02$ and $B = 0.008 \pm 0.002$ [32]. The first term arises from multiple scattering in the toroid iron and the second term is due to spatial resolution and alignment errors of the muon chambers. The second term has been obtained from the study of W and Z data [33], since spatial resolution effects are most pronounced at high muon momenta.

Chapter 4

The Trigger System

4.1 Overview

Beam crossings at the Tevatron occur every $3.5\ \mu\text{s}$, i.e. at a rate of 300 kHz. The total (elastic and inelastic) cross section for $p\bar{p}$ -interactions at $\sqrt{s} = 1.8\text{ TeV}$ is about 70 mb [34], which results in an interaction rate of 200 Hz at a typical luminosity of $3 \cdot 10^{30}\text{cm}^{-2}\text{s}^{-1}$.

With an average readout time of $\approx 400\ \mu\text{s}$, it is impossible to fully read out the detector for every $p\bar{p}$ -interaction. The trigger was designed to select collisions containing interesting physics processes while limiting the event rate to $\leq 3\text{ Hz}$. The trigger requires typically one or more leptons above some energy threshold and/or one or more jets. For example the W-triggers require a muon of $p_T > 15\text{ GeV}$ or an electron of $E_T > 20\text{ GeV}$, while those for the top-quark search required one or more high p_T -leptons ($p_T > 10\text{ GeV/c}$) in coincidence with at least one high E_T -jet ($E_T > 15\text{ GeV/c}$) .

The trigger logic is grouped into three stages: level 0, level 1 and level 2.

- The level 0 logic identifies non-diffractive inelastic collisions and estimates the z -position of the interaction vertex.
- For this study the level 1 trigger checks if the pattern of proportional drift tubes showing a charge distribution above threshold on the cathode pads is consistent with a muon originating in the beam pipe. Jets are identified by a minimum energy deposition in a set of calorimeter cells pointing to the center of the detector.
- The level 2 trigger uses 48 VAXstation 4000 60's to perform partial reconstruction of events satisfying the level 1 trigger. It provides a measurement of the momentum and energy of muons and jets respectively, and of their direction. In the process the raw information read out from the detector is transformed into the ZEBRA data structure [35].

The level 0 and level 1 decisions are made within the $3.5 \mu\text{s}$ interval between beam crossings. If the event satisfies both the level 0 and level 1 triggers, then level 2 trigger processing is started. The typical processing time for an event in level 2 is $350 \mu\text{s}$, resulting in an average deadtime of $\approx 2\%$ [36].

The level 0 trigger rate is dependent on the luminosity. For the data analyzed here this was typically around 200 kHz. Because of the limited processing power at level 2, the level 1 logic was configured to restrict the maximum level 1 trigger rate to ≈ 200 Hz. Similarly the maximum rate at which the host computer can record events to magnetic tape imposes a maximum trigger rate of ≈ 3 Hz on the level 2 processors.

4.2 The Muon-Jet Trigger

The trigger for the muon-jet analysis is designed to select a data set enhanced in b -quark production. As discussed in section 2.1 due to confinement quarks are not observed as free particles in the lab. We have to identify b -quarks from their decay products; we use the decay $b \rightarrow c + \mu\nu$ ($BR = 0.110 \pm 0.005$) [37]. The c quark forms a set of collimated hadrons referred to collectively as a jet, the energy of which is measured in the calorimeter. There may be additional jets in the event due to other final state partons. The fragmentation process responsible for the formation of jets is described in more detail in section 6.2. We use the presence of ≥ 1 muon and ≥ 1 in the trigger as well as offline to identify b -production. The coincidence of muons and jets reduces the background from cosmic ray muons and muons from W and Z boson decays. The estimates of backgrounds in the data sample are described in chapter 9.

The differential cross section for b -quark production decreases both with increasing p_T of the $b \rightarrow \mu X$ decay muon and E_T of the jet. In order to cover a large range in b -quark transverse momenta, it is desirable to set the thresholds in the trigger as low as possible. For this analysis the level 2 requirement was one jet with $E_T > 10$ GeV within $|\eta| < 3.2$, and one muon with $p_T > 3$ GeV/c and within $|\eta| < 1.7$.

At an instantaneous luminosity of $3 \cdot 10^{30} \text{ cm}^{-2}\text{s}^{-1}$, the muon-jet trigger selects about 1 event per second and hence consumes about a third of the available bandwidth. In comparison, the high p_T muon trigger for the measurement

of the W -boson production cross section passes events at about 0.1 Hz at the same luminosity.

Due to their low individual pass rates it is possible to run several of the high-threshold triggers (such as the W -trigger) in parallel. If the muon-jet trigger was to be included, it would have to be “prescaled” i.e. only a small fraction of the events passing the trigger would be recorded in order to be able to share the bandwidth with the other trigger. To get around this limitation the data for this analysis were taken during dedicated data taking runs in which 1/3 of the bandwidth was allocated to the muon-jet trigger while the remaining 2/3 were allocated to a higher rate inclusive low threshold muon trigger.

A total of 18 such “dedicated” runs were taken over a period of 36 hours, collecting 51329 events for a total luminosity of 228 nb^{-1} . Information about these runs is summarized in table 4.1.

4.3 Main Ring Veto

Since the Main Ring of the accelerator passes through the upper part of the DØ calorimeters, halo particles accompanying the circulating proton bunches can deposit energy in the calorimeter and corrupt the energy measurements both at the trigger level and later in the reconstruction.

This can happen whenever the Main Ring is operating for antiproton production concurrently with data taking at DØ. During main ring operation protons at 8 GeV are transferred (injected) from the booster ring into the

run number	duration of run (min)	starting luminosity ($10^{30} \text{cm}^{-2}\text{s}^{-1}$)	integrated luminosity (nb^{-1})	number of triggers
62354	67	3.1	9.28	2632
62488	70	2.6	6.56	1303
62515	50	3.7	7.81	2454
62516	72	3.5	10.3	3270
63478	74	2.0	5.98	1239
63497	189	3.2	24.4	4865
64092	98	3.6	14.3	2127
64215	200	2.2	17.1	2695
64485	53	2.4	4.94	788
64486	102	2.3	9.24	1436
64614	145	3.6	22.0	3697
64790	131	2.6	11.0	3175
64801	111	N/A	15.1	3709
65630	280	2.3	25.5	6168
65635	65	1.7	4.58	1087
65762	220	2.9	16.9	4631
65769	201	2.2	16.5	4261
65879	63	2.5	6.46	1997
total	2191		228	51329

Table 4.1: Collider runs used in the Analysis

Main Ring and subsequently “ramped up” in energy to 120 GeV and are then diverted to a target for antiproton production. This process repeats every 2.4 s. Due to poor magnetic field quality at 8 GeV, the beam lifetime is very short, of the order of 0.5 s. Some of the particles that are not confined to the beam pipe by the magnetic field (beam losses) travel parallel to the collider beam and can scatter off the magnets or parts of the detector and may end up in the calorimeter or muon system [38].

No events are recorded during the period of injection, which corresponds to the first 0.4 s of the 2.4 s main ring cycle. This results in $\approx 17\%$ loss of luminosity. In addition events are vetoed whenever a bunch of main ring protons passes through the detector during ramping, which causes an additional 7-9% loss in luminosity.

4.4 Minimum Bias Trigger (Level 0)

The level 0 trigger utilizes two scintillator hodoscopes mounted on the front surfaces of the end calorimeters, 140 cm away from the center of the detector. The hodoscopes have a checkerboard-like pattern of scintillators inscribed within a 45 cm circle centered at and perpendicular to the beam axis. The square cross-section of the hodoscope result in a partial pseudorapidity coverage of $1.9 < |\eta| < 4.3$ and a full coverage within $2.3 < |\eta| < 3.9$ [39].

For the trigger to fire, a signal above threshold has to be observed in both hodoscopes. This coincidence of signals on both sides of the interaction region differentiates inelastic collisions, in which both protons and antiprotons

fragment, from beam gas interactions and single diffractive processes, which typically produce a signal in only one of the scintillators; diffractive processes rarely produce a coincidence.

Such a trigger requiring only a non-diffractive inelastic interaction is referred to as a minimum bias trigger and is necessary since the muon trigger could in principle be satisfied by the overlap of cosmic ray background and a beam gas interaction. The additional requirement of an inelastic interaction eliminates this type of background. The level 0 hodoscopes also provide a measurement of the z -coordinate (along the beam pipe) of the interaction vertex which is used in the level 1 and level 2 logic. The vertex position is determined from the difference in arrival times of particles at the north and south hodoscopes. This measurement has a resolution of about 3 cm for single interactions which deteriorates to 6 cm for multiple interactions, when the scintillators have to distinguish between particles created in each interaction.

The level 0 counters also monitor the instantaneous luminosity. The relationship between the instantaneous luminosity \mathcal{L} , and the level 0 trigger rate, R , is given by $\mathcal{L} = \sigma R$, where σ is the minimum bias cross section, about 48 mb. Details of the luminosity calculation are given in reference [21]

4.5 Muon Trigger

- **The Muon Level 1: Hardware Trigger**

The muon level 1 trigger is based on a pattern of drift tubes showing a charge deposition on the cathode pads consistent with a muon incident

within 45° of the normal on each layer. For this purpose each layer (ABC) of the muon system is divided into 60 cm wide hodoscopic elements. In the B and C-layers charge depositions (“padlatches”) are required from two out of the three planes of drift tubes. In the A-layer three out of four planes are required [40].

The muon level 1 trigger identifies muon candidates in the region $|\eta| < 1.7$. A trigger algorithm checks if the hits in the hodoscopic elements are consistent with a muon coming from the interaction region [41].

To fire the level 1 trigger one of these hodoscopic elements is required to be hit in all three layers of the muon system. The only exception to this is the bottom of the detector where two-layers patterns are accepted because there is reduced A-layer coverage to accommodate the calorimeter support structure.

- **The Muon Level 2: Software Trigger**

The fully digitized readout from the detector is available to the level 2 processors. The muon level 2 trigger algorithm is similar to the one used in the offline reconstruction. It is divided into two parts, the first of which converts the information from each proportional drift tube that has a padlatch into points in the bend and non-bend views of the muon system. The second part of the algorithm reconstructs the trajectory of the muon and infers its momentum from the degree of bending of the track in the magnetic field. The residuals of the fits in the bend view

and along the wire are required to be consistent with a beam-produced muon.

The program also identifies cosmic rays by checking for hits in the muon system opposite each reconstructed muon. If two muon tracks are reconstructed back-to-back, with $\Delta\Phi > 160^\circ$ and $\Delta\theta > 170^\circ$, both are rejected as cosmic rays. In addition the program defines a window 60 cm wide in the bend view and 150 cm wide in the non-bend view centered around the extension of a reconstructed muon track into the opposite side of the muon system. If three points are reconstructed in both the bend and non-bend view, the reconstructed trajectory is attributed to a cosmic ray.

To pass the level 2 trigger, a muon is required to have $p_T > 3 \text{ GeV}/c$ and $|\eta| < 1.7$.

4.6 Calorimeter Trigger

- **Calorimeter Level 1 Hardware Trigger**

The calorimeter level 1 trigger bases its decision on the energy deposited in a set of cells (“trigger towers”) covering an area of $\Delta\eta \times \Delta\phi = 0.2 \times 0.2$ and projecting to the center of the beam crossing area. The trigger was instrumented for $|\eta| \leq 3.2$. The energy deposited in the trigger tower is converted to transverse energy, E_T , using the level 0 vertex information.

For this study at least one trigger tower with $E_T > 3 \text{ GeV}$ is required [43].

- **The Jet Level 2 Reconstruction**

Jets, a collimated set of high p_T hadrons from the hadronization of a parton, manifest themselves in the calorimeter as a collection of adjoining cells with a high deposition of transverse energy. The energy estimate of a reconstructed jet depends on the algorithm used. The Level 2 trigger and the offline reconstruction both use a cone algorithm to identify jets. The jet energy is defined as the energy deposited in a cone of $\Delta R = \sqrt{(\Delta\eta)^2 + (\Delta\phi)^2} = 0.7$ around the center of the level 1 trigger towers with $E_T > 3 \text{ GeV}$ [43].

To find the transverse energy of the jet, an energy vector \mathbf{E} is assigned to each cell within the jet cone. The magnitude of the energy vector is the energy deposited in the cell, its direction is given by the radius vector from the interaction vertex to the center of the cell.

The transverse energy of the jet and its direction are then:

$$E_T = \sqrt{\left(\sum_i E_x^i\right)^2 + \left(\sum_i E_y^i\right)^2} \quad (4.1)$$

$$\eta = -\ln \tan(\theta/2) \quad (4.2)$$

$$\theta = \sin^{-1} \frac{E_T}{\sum_i E^i} \quad (4.3)$$

$$\phi = \tan^{-1} \frac{\sum_i E_x^i}{\sum_i E_y^i} \quad (4.4)$$

where the summation index i runs over all cells in the jet cone.

Chapter 5

Off-Line Reconstruction

5.1 Overview

The offline event reconstruction was performed on a farm of Silicon Graphics microcomputers one week to one month after the data was recorded. The algorithms used in the offline reconstruction are similar but more refined than the ones used in the level 2 trigger. For example, the determination of the z -position of the interaction vertex is based on tracks reconstructed in the CDC. The offline reconstruction takes about 25 s for a typical event [44].

The time delay between data taking and reconstruction makes it possible to prepare calibration constants more precise than those used in the trigger.

5.2 Vertex Reconstruction

The reconstruction of the primary interaction vertex is based on tracks reconstructed in the CDC and, since there is no magnetic field, the particle

trajectories are straight lines. To remove background from particles that are not beam produced, the tracks used for vertex determination are required to have an impact parameter relative to the beam axis in the $r - \phi$ plane of ≤ 2.5 cm.

The z -coordinates corresponding to the r, ϕ points of closest approach, are then histogrammed in 2 cm wide bins. The bin containing the largest number of tracks (≥ 2) and its contiguous bins containing at least one track constitute a cluster. The mean z -position of the tracks in the cluster containing the most tracks is taken as the z -position of the primary vertex. If there are no bins with at least two tracks the largest contiguous sets of bins, containing one track each, is taken as the cluster [43].

The z -distribution of the vertices is approximately Gaussian, centered at $z = -7$ cm (i.e. south of the center of the detector) with a σ of about 30 cm. The standard deviation of an individual z -measurement is of the order of 1 cm.

The position of the primary vertex in the $r - \phi$ plane is determined from vertex detector data. The position of the center of the interaction point of the proton and antiproton beams is stable during a collider store and is verified on a run-by-run basis using the VTX tracking information. The measurement has a resolution $\approx 30\mu\text{m}$, which is roughly 1/2 of the diameter of the beam in the detector ($60\mu\text{m}$). The latter is taken as the error in the transverse position of the interaction vertex. The movement of the transverse beam position over several months of data taking has been measured to be less than one millimeter [46].

5.3 Muon Reconstruction

The offline muon reconstruction uses the same procedure as the level 2 trigger, with an additional step in which the muon momentum measurement is refined by the inclusion of the CDC tracking information to better constrain the track direction. The basic steps of the reconstruction are outlined below.

First the information from each proportional drift tube that has a pad-latch and drift time information is converted into points in the bend and non-bend view projections of the detector coordinate system. The program uses survey information indicating the position of the drift tube in the detector coordinate system and calibration constants describing the characteristics of the amplifiers and time to voltage converters. Then least squares fits in the bend and non-bend views determine the muon trajectory. The momentum is inferred from the amount of bending in the magnetic field.

In the non-bend view the hits in the three layers are fit to a straight line which is constrained to pass through the interaction point. The first fit uses only the charge division along the sense wire (ΔT -information) for the position of the muon along the wire; the result is used to determine which “diamond” of the pad pattern the muon passed through (see section 3.5), and a second fit is performed. The improved precision of this measurement allows us to obtain the position of the muon track without using the vertex position, provided that there sufficient hits for an accurate track position measurement. If the vertex is not used the measurement is not affected by multiple scattering of

the muon in the calorimeter. The vertex is used only if there are two or less points on the track in the A layer.

In the bend view separate track segments are fit inside and outside the magnet with the constraint that they must meet in the center of the muon iron. Similar to the non-bend view measurement, the vertex is used in the fit only if there are insufficient hits to determine the position of the track. If the track has information only in two of the three layers, then the vertex point is used as an additional constraint in the track fits.

The fit-residuals in both views, and the projections of the track back to the primary vertex in both views were required to be consistent with a beam-produced muon. Using formula 3.5, a first estimate of the muon momentum is obtained.

There is an additional level of reconstruction in which a search is performed to find the matching track in the CDC consistent with Multiple Coulomb Scattering of the muon as it passes through the calorimeter and the muon iron. If a matching CDC track is found, the information is incorporated into another fit of the muon trajectory.

The muon trajectory is recalculated with simultaneous least squares fits in the bend and non-bend view [47]. The following information serves as the input to the fit:

- There are two input variables describing the position of the interaction vertex in each view.
- The track segments in the CDC and in the muon system before and

after the magnet are described by an impact parameter relative to the interaction vertex and a direction each in both views.

The seven parameters of the least-squares fit are

- An impact parameter and a direction, describing the position of the muon track before the calorimeter in the bend and non-bend view each (4 parameters).
- An angle in each view describing the bending of the muon trajectory due to Multiple Coulomb Scattering in the calorimeter (2 parameters).
- The inverse $1/p$ of the muon momentum. From formula 3.5 we observe that that the magnetic deflection angle of the muon track, which is the quantity that is actually measured, is inversely proportional to the momentum. Hence we fit for the inverse of the muon momentum ($1/p$), which has a gaussian distribution (1 parameter).

5.4 Jet Reconstruction

The starting points for jet reconstruction are the calorimeter towers with a transverse energy E_T of more than 1 GeV each. As in the case of the level 1 trigger tower, a tower is a set of calorimeter cells which project to $z = 0$. If several such towers are directly next to each other, they are combined and the E_T weighted center in $\eta - \phi$ space of the resulting "precluster" is calculated.

The transverse energies associated with all calorimeter cells within $\Delta R = 0.7$ of the center of the precluster are added vectorially, and the E_T and the

direction (η and ϕ) of the axis of the jet are calculated using equations 4.1 - 4.4. The resulting η and ϕ serves as the axis of the jet cone for the next iteration. The iteration process is then continued until the η and ϕ values converge, which typically requires four such iterations. Only jets with $E_T > 8$ GeV are retained.

Sometimes the cones of two jets reconstructed with the above algorithm overlap. If the energy deposited in the cells that lie within the cones of both jets is more than half of the E_T of the smaller jet, then the jets are merged. The E_T of the merged jet and the direction of its axis are then recalculated by summing over the cells contained in both jets.

If the energy in the overlap of both cones is less than 50% of the E_T of the smaller jet, then the energy in each cell in the overlap region of both cones is assigned to the jet whose axis is closest to the cell in $\eta - \phi$ space, and the E_T as well as the directions of both jets are recalculated.

Several corrections are applied to the measured jet E_T obtained by the above prescription. The corrections are necessary because the “true” jet E_T differs from the jet E_T measured by the above method due to the following effects:

- Particles produced by processes other than the hadronization of the parton that produced the jet can deposit energy that falls within the jet cone. The additional particles can come from soft interactions of remaining (“spectator”) partons from the proton and antiproton or from

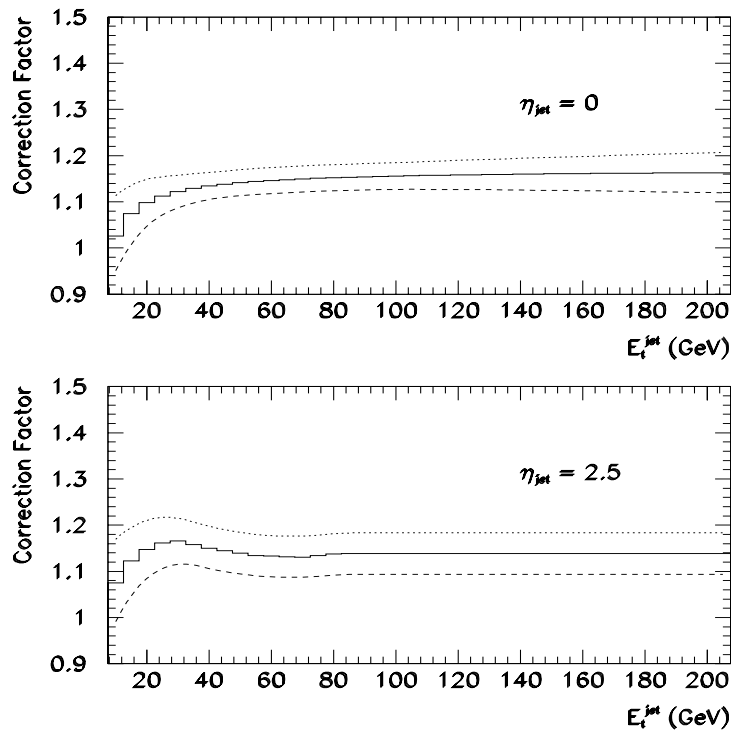


Figure 5.1: The jet energy scale correction factor for the jet E_T shown for jets of two different pseudorapidities. Shown are the best estimate for the correction, and an upper and lower limit indicating the uncertainty in the corrections.

the overlap of additional interactions within the detector live time. These effects contribute typically ≈ 1 GeV.

- Particles from the nuclear decays of Uranium atoms in the absorber can deposit energy in the calorimeter, leading also to an overestimate of the jet E_T . Data was taken in the absence of $p\bar{p}$ -collisions to measure the contribution of that effect. For central jets, "calorimeter noise" adds about 2 GeV to the energy in the jet.
- Since it is difficult to determine the "boundaries" of a jet, a jet is defined operationally as the collection of hadrons that fall within a cone of radius ΔR of the jet axis. However, if these hadrons interact in the calorimeter, some of the secondary particles are scattered out of the cone. This effect, sometimes referred to as "out of cone showering", lowers the measured jet E_T by about 5%.

In addition, once corrections for out of cone showering, noise and underlying event contributions are implemented, data from $p\bar{p}$ -collisions can be used for calibration of the calorimeter as well. The calibration of the electromagnetic part of the calorimeter can be done from the invariant mass peaks from $Z \rightarrow e^+e^-$ and $\Upsilon \rightarrow e^+e^-$ decays [48]. This calibration of the electromagnetic calorimeter can then be transferred to the hadronic part by adjusting the jet E_T in events containing exactly one jet and one photon 180° apart in ϕ to obtain E_T -balance (no net E_T) in the event [43].

Compensations for all these effects are combined in the jet energy scale correction function, which is a multiplicative correction to the reconstructed

E_T of a jet, parameterized as a function of transverse energy and pseudorapidity of the jet. Fig. 5.1 shows the jet E_T correction as a function of the reconstructed E_T of the jet for central ($\eta = 0$) and forward ($\eta = 2.5$) jets.

Chapter 6

Simulation of Data

6.1 Introduction

The goal of this project is to measure the $b\bar{b}$ production cross section in $p\bar{p}$ interaction at 1.8 TeV while simultaneously testing the QCD sector of the Standard Model. Monte Carlo simulations of Standard Model processes play a central role in this project.

This chapter describes how large samples of $b\bar{b}$ production events and a variety of background events are simulated in the D \emptyset detector. The cross sections at the parton level are calculated according to equation 2.1, using the ISAJET generator [49]. The partons fragment into hadrons followed by decays of the B and C hadrons. The hadron and lepton 4-vectors are then tracked through the D \emptyset apparatus using the detector simulation program GEANT [50].

GEANT simulates π/K decays and interactions with detector material, as well as the path of secondary particles created along the way. The output

of the detector simulation consists of raw data (such as pulse heights or ADC counts) which are encoded in the same ZEBRA data structure as the actual data read out from the detector. Events are then filtered through a trigger simulation routine and lastly are processed through the DØ reconstruction software.

As discussed in subsequent chapters the Monte Carlo events are employed for a variety of processes:

1. to test our understanding of detector acceptance and performance (see chapter 8).
2. to estimate backgrounds to the heavy quark signal such as W , Z , Drell-Yan production and decays-in-flight (chapter 10).
3. to verify that the observed heavy quark signal has the kinematic configuration predicted by the standard model.

6.2 Generation of Event 4-Vectors

ISAJET is a Monte Carlo program that generates 4-vectors of particles created in high energy $p\bar{p}$, pp or e^+e^- collisions.

Cross sections at the parton level are calculated according to equation 2.1

$$\sigma = \sum_{ij} \int dx_i dx_j \hat{\sigma}_{ij}(x_i p_A, x_j p_B, \mu, \Lambda) F_i^A(x_i, \mu) F_j^B(x_j, \mu) \quad (6.1)$$

where, as discussed in section 2.1, F_i^A and F_j^B are the structure functions describing the density of partons i and j inside the proton (A) or antiproton

(B). x_i and x_j are the corresponding fractions of the total proton (p_A) and anti-proton (p_B) momenta.

ISAJET generates a parton-parton hard scattering according to lowest order matrix elements, using $\Lambda = 0.2$ and $\mu = \sqrt{p_t^2 + m^2}$. Some of the corresponding Feynman diagrams are shown in fig. 2.1 a) and b). QCD radiative corrections to arbitrary order are included by allowing both the initial and final state partons to radiate gluons which can split into $q\bar{q}$ -pairs. Although it is not a complete next-to-leading order calculation, this procedure does a good job reproducing the kinematic features of next-to-leading order heavy flavor production. Thus both the UA1 collaboration at $\sqrt{s} = 0.63$ TeV and DØ at $\sqrt{s} = 1.8$ TeV have compared the angular difference $\Delta\Phi^{\mu\mu}$ in dimuon events enriched by heavy quark production. We expect that in leading order processes the heavy quarks, and hence the muons from their decays, are produced back-to-back. In next-to-leading order processes there are three final partons in the event, hence the b -mesons and the decay muons are closer together in Φ . Both experiments observed that ISAJET reproduces the experimental $\Delta\Phi$ distributions well [51, 52].

For this analysis ISAJET was run in $p\bar{p}$ -mode using versions 6.49 and 7.13. Version 6.49 was run in combination with the full detector and trigger simulations. It used the now obsolete EHLQ structure functions [53]. Due to the large computing time required for the detector simulation it was not feasible to repeat this simulation with improved structure functions. However, we use version 7.13, which contains the newer CTEQ2L structure functions [54]

for applications that do not require detector simulation, such as the cross section calculations.

For hadronization ISAJET adopts the Feynman Field model of independent fragmentation [55]. Basically, an initial quark q_0 radiates a gluon that splits into a light quark pair $q_1\bar{q}_1$, one of which forms a meson ($q_0\bar{q}_1$), carrying some fraction z of the q_0 's original momentum. This leaves q_1 in the place of q_0 , with momentum fraction $1-z$. The process repeats until the residual momentum fraction falls below a fixed cutoff value, at which time the remaining quarks are combined into hadrons.

The momentum fractions are distributed according to the fragmentation function $D(z)$ as described below. For light quarks (u, d and s), ISAJET uses

$$D(z) = 1 - a + a(b+1)(1-z)^b \text{ where } a = 0.96, b = 3 \quad (6.2)$$

while for heavy quarks (c, b and t) the Peterson fragmentation function is used:

$$D_Q(z) = \frac{1}{z [1 - 1/z - \epsilon_Q/(1-z)]^2} \quad (6.3)$$

where the Peterson parameter, ϵ_Q is a function of the mass of the quark (m_Q) considered: $\epsilon_Q = 0.5 \text{ GeV}^2/m_Q^2$. Figure 6.1 shows the fragmentation function $D_Q(z)$ as a function of the momentum fraction z for b and c -quarks. The b -quark fragmentation function peaks at a higher momentum fraction than the c -quark fragmentation function so that the resulting B -hadron spectrum is “stiffer”, i.e. has a higher mean transverse momentum, than the corresponding D spectrum from c quark fragmentation. The parameters of the b and c -quark Peterson functions are tuned to reproduce experimental data from e^+e^- -collisions.

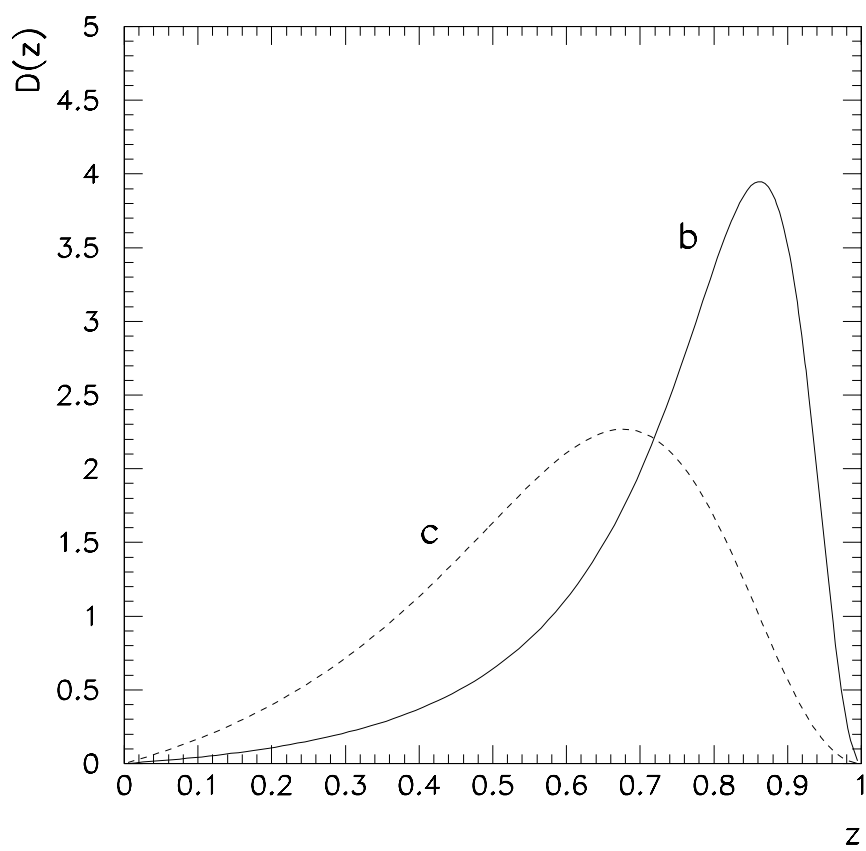


Figure 6.1: Peterson fragmentation function for b and c -quarks for $\epsilon_Q = 0.022$ and 0.15, respectively.

ISAJET decays short lived hadrons, that decay in the beam pipe, according to measured lifetimes and branching ratios if experimental values are available; otherwise phenomenological arguments were used for estimates. B hadrons are decayed in ISAJET using a simplified $V - A$ -spectator model. In this model the heavy quark in the meson is considered to be independent of the other quarks and decays as a free particle. Longer lived particles, such as pions or kaons, that travel into the detector, are decayed as part of the detector simulation (see section 6.3).

The leftover partons of the incoming proton and antiproton fragment to “beam jets”. ISAJET models beam jets by superimposing a minimum bias event on top of the hard scattering interaction [56]. The minimum bias event is generated with multi-pomeron chains which reproduce scaling and long range correlations between the hadrons in the beam jets [49].

6.3 Detector Simulation

The detector simulation for this analysis is based on the program DØGEANT, which is the DØ-specific implementation of the generic CERN detector simulation package GEANT [50]. The DØ implementation specifies the various materials present in the detector in the form of a list of “volumes” of the appropriate shape.

The program provides the framework for transporting particles (generated by ISAJET) through these volumes with the appropriate physical scattering and interaction processes included. Gamma-ray production, Multiple Coulomb

Scattering, showering by electromagnetic and hadronic particles, decays and Bremsstrahlung are accurately modelled.

The geometric simulation is most detailed for the central detectors and the muon system, which is described down to the level of the sense wires, cathode material and support structures. The calorimeter modelling is simplified in order to save computing time in the simulation of the complex showering process. While support-structures are still implemented in detail, the internal absorber/liquid argon structure is replaced with a homogeneous mixture of suitable effective atomic weight, greatly reducing the number of volumes in the Monte Carlo implementation. Still, the CPU requirements are significant, one typical $b\bar{b}$ events takes about 10 min of CPU time on a SGI INDIGO machine.

For the muon system, DØGEANT simulates an idealized detector. Inefficiencies in the chamber positions, resolutions, and errors in the alignment are not accurately modeled. A supplementary program, MUSMEAR, has been developed to include these effects [57]. The advantage of this add-on package is that the time consuming DØGEANT program will not have to be rerun if our knowledge of the detector alignment or chamber efficiencies improves. Details of the MUSMEAR program are given in appendix A.

6.4 Trigger Simulation

The trigger simulator determines whether an event passes a specific trigger. The hardware of the level 0 and level 1 triggers is modeled in detail in the

	process	number of events generated
1	$p\bar{p} \rightarrow b\bar{b}X \rightarrow \mu X$	20,000
2	$p\bar{p} \rightarrow c\bar{c}X \rightarrow \mu X$	10,000
3	$p\bar{p} \rightarrow W X \rightarrow \mu\nu X$	10,000
4	$p\bar{p} \rightarrow ZX \rightarrow \mu\mu X$	10,000
5	$p\bar{p} \rightarrow \pi/K X \rightarrow \mu\nu X$	5,000

Table 6.1: The Simulated Data Sample

trigger simulation program. The level 2 reconstruction in the simulator runs (with minor technical modifications) the same computer code as the actual trigger.

The result of the trigger simulation is recorded in a ZEBRA bank together with the readout information of the detector simulation. As in the actual trigger, the direction and energy of muons and jets found in level 1 or reconstructed in the level 2 trigger are recorded as well. The trigger simulator retains events that fail the trigger; this allows us to study the properties of events that do not pass the trigger and is an indispensable tool for determining trigger efficiencies (chapter 8).

6.5 The Simulated Data Samples

We have generated Monte Carlo events for the signal process, $b \rightarrow \mu X$, as well as for other physics processes which have muons and jets in the final state (Table 6.1).

Processes 1 to 4 in table 6.1 are simulated with 4-vectors generated by ISAJET which were then processed through the detector and trigger simulation, and reconstructed. We require a muon of $p_T > 3$ GeV/c in the ISAJET event. This avoids time consuming detector simulation of events that do not contain muons at all, or muons incapable of penetrating the calorimeter and muon toroid.

The generation of the π/K in-flight decay Monte Carlo sample (process 5) is more complicated due to the fact that ISAJET does not simulate pion or kaon decays. Pions and kaons decay within the detector, predominantly in the central detectors and the first few interaction lengths of the calorimeter. However, a 5 GeV pion (kaon) for example has only a $\approx 0.3\%(1.5\%)$ chance of decaying in the ≈ 0.8 m distance to the calorimeter; the vast majority will interact hadronically in the calorimeter.

We have generated ISAJET minimum bias events and low E_T jet events and randomly selected one pion or kaon in the event and decayed it into a muon or neutrino. We then “weight” the event by the probability of that decay occurring naturally. Details of the in-flight decay Monte Carlo are given in appendix B.

6.6 Test of Validity of ISAJET Predictions

As described in section 6.2, ISAJET uses an approximation for the QCD α_s^3 terms. So it is necessary to test the validity of the Monte Carlo data by comparison with:

1. measured quantities,
2. more exact calculations.

The distribution of charged particles in the ISAJET minimum bias spectrum is compared to a measurement of the inclusive charged hadron spectrum by CDF [58]. Figure 6.2 shows that ISAJET reproduces the shape of the hadronic p_T distribution but overestimates the charged hadron cross section by about 20% on average. We therefore introduce a scale factor to correct the ISAJET prediction to the observed value, but due to the fluctuations in figure 6.2, we also assign a 20% error on our prediction of the in-flight decay spectrum. An additional 8% error is due to uncertainties in the fraction of pions and kaons in the inclusive hadron spectrum (appendix A). Summing these two errors in quadrature gives a 22% uncertainty in the background from in-flight decays of pions and kaons.

Processes (3) and (4) in table 6.1 can be directly compared to results of DØ measurements. DØ has measured the cross section for W and Z -boson production from decays into both electrons and muons: $\sigma(p\bar{p} \rightarrow WX) \cdot BR(W \rightarrow lX) = 2.30 \pm 0.07 \pm 0.12 \text{ nb}$ and $\sigma(p\bar{p} \rightarrow ZX) \cdot BR(Z \rightarrow ll) = 0.207 \pm 0.010 \pm 0.011 \text{ nb}$ where $l = e$ or μ [59]. The ISAJET cross section

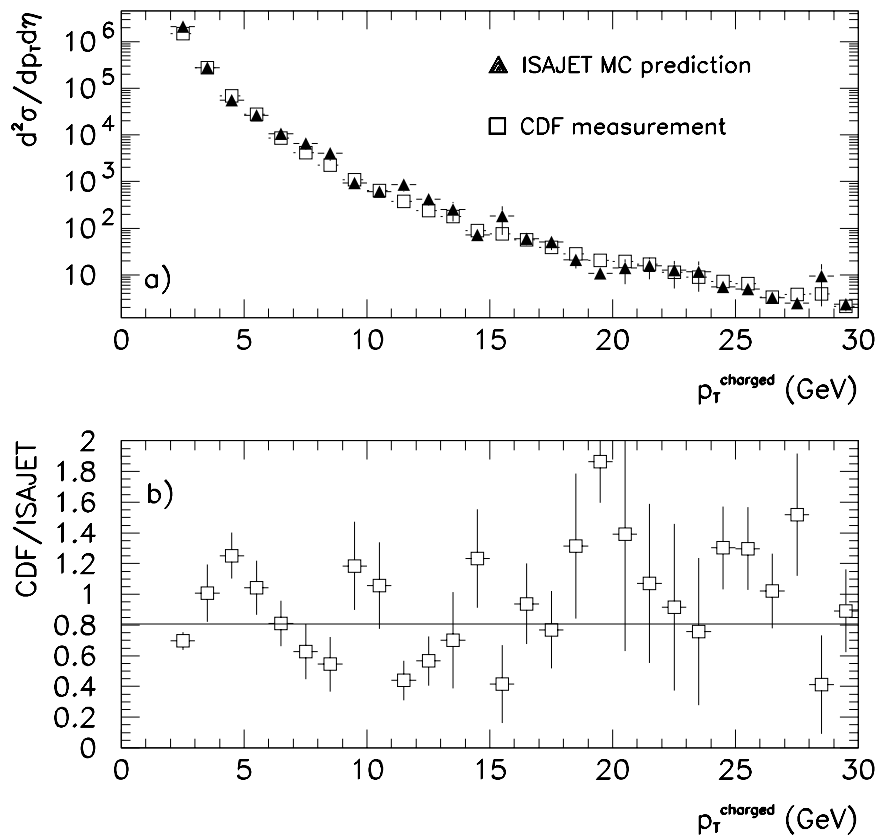


Figure 6.2: Comparison of the inclusive charged hadron cross section predicted by ISAJET and from CDF data. Fig. b) shows the ratio of CDF/ISAJET.

prediction for $W \rightarrow \mu\nu$ and $Z \rightarrow \mu\mu$ was replaced by these measured values. Furthermore, preliminary studies suggest that ISAJET underestimates the production of jets associated with W/Z -production. The data suggest that $44 \pm 6\%$ of W -bosons are produced in association with jets of $E_T > 15 \text{ GeV}$, while ISAJET predicts only 27% [60]. Again, we introduce a correction factor to the Monte Carlo to match the data. The error in the cross-section prediction for W and Z decays is set to 15%, the sum in quadrature of the systematic errors in the measurements of $\sigma(p\bar{p} \rightarrow WX) \cdot BR(W \rightarrow lX)$ and $\sigma(p\bar{p} \rightarrow ZX) \cdot BR(Z \rightarrow ll)$, $\approx 5\%$ and the error in the fraction of W events accompanied by a jet, 14%.

Figure 6.3 shows a comparison of the ISAJET predictions for b and c production with the complete next-to-leading order calculations of NDE (Section 2.2). The ISAJET prediction reproduces the shape of the p_T dependence but the overall magnitude is a factor of ≈ 2 higher than the NDE calculation, independent of the p_T of the $b(c)$ -quark.

When comparing experimental data with theory prediction of b or c production, we use the NDE cross section and rely on ISAJET only for the simulation of fragmentation and decay of b -quarks. For the muon spectrum from $b \rightarrow \mu X$ and $c \rightarrow \mu X$ decays we multiply the ISAJET prediction for the spectrum by 0.52 and 0.59 respectively.

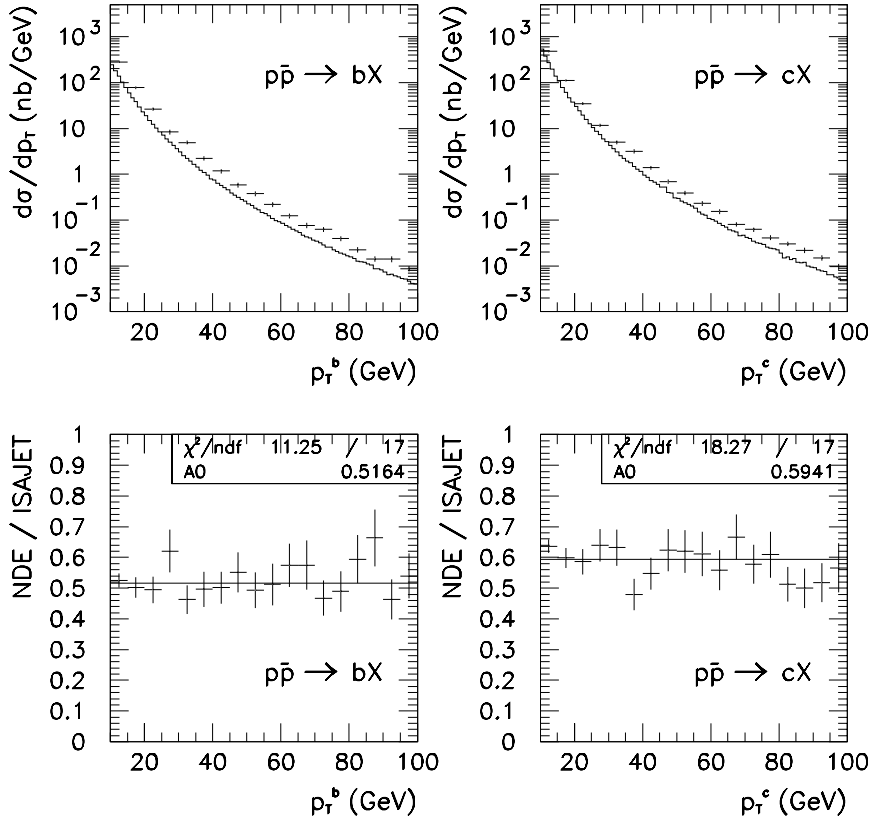


Figure 6.3: Comparison of ISAJET and NDE [14] calculations for b -production (figs a, c) and c -production (figs b, d), as a function of the p_T of the heavy quark. The data points in a) and b) denote ISAJET predictions, while the solid line is for the NDE calculation. All plots are for $|y| < 1.0$ of the b and c quarks. The solid line in c) and d) is a fit of a constant to the ratio NDE calculation/ISAJET.

6.7 Summary

We have described the procedure for generating the Monte Carlo data samples for this analysis. Properties of the trigger and event reconstruction were studied by passing the simulated data based on the ISAJET event generator through the detector and trigger simulation and the offline reconstruction program. In order to obtain realistic predictions for production cross sections, we have renormalized

- the ISAJET b and c quark production cross sections to NDE calculations.
- the ISAJET $W/Z \rightarrow \mu + \text{jets} + X$ cross section to D \emptyset measurements.
- the ISAJET inclusive charged particle cross section to CDF measurements.

By doing so we have effectively replaced the ISAJET cross section calculations with data or at least more reliable theoretical predictions.

The agreement in shape in figures 6.2 and 6.3 gives us confidence that ISAJET does adequately model the kinematics of b and c -production, as well as of pion and kaon in-flight decays.

Chapter 7

Data Selection

7.1 Introduction

The next step, after having reconstructed the data with the muon-jet trigger is to isolate a set of well-measured events in which a muon and a jet have been produced in a beam-beam interaction.

Kinematic cuts are applied to restrict the data to kinematic ranges for which detector acceptance and trigger efficiency are well understood; fiducial cuts are applied to exclude problem regions of the detector. The data contains background both from cosmic ray muons and from "muon tracks" reconstructed from unassociated track segments in the muon chambers ("combinatorics"). These background muons will be eliminated on the basis of their lack of correlation with the interaction vertex and with the beam crossing time.

Finally additional criteria are applied to optimize the "quality" of the muons and jets such that the final data sample consists of well measured muons and jets. All criteria for selecting muon-jet events are based on the

geometry and properties of the D \emptyset detector and on the trigger design.

In this chapter we motivate and define the cuts; event losses “efficiencies” associated with the selection criteria are calculated in chapter 8.

7.2 Fiducial and Kinematic Cuts

We first describe the cuts imposed to confine muons and jets to a region where the efficiencies can be measured do not require very large correction factors when the momentum spectrum is calculated in chapter 9. We reject muons with an efficiency below 18% and jets with an efficiency below 10%.

7.2.1 Muons

The level 2 trigger restricts the muon to $p_T > 3 \text{ GeV}$ and $|\eta| < 1.0$. Because of increasing background due to beam fragments at forward angles it was decided to restrict the muon sample to the central muon spectrometer at $|\eta| < 0.8$ to avoid regions of low $\int B dl$ (fig. 3.10).

The main ring beampipe (section 3.1.1) passes through the upper hadron calorimeter. Beam halo has caused radiation damage in the nearby A layer muon chambers (fig. 3.8). The resulting chamber inefficiency around $\phi = 90^\circ$ is apparent in fig. 7.1 which shows the ratio Data / Monte Carlo for the muon spectrum as a function of the azimuthal angle ϕ . Based on this plot a fiducial cut is applied to exclude muons in the affected region:

$$\phi^\mu < 80^\circ \text{ or } \phi^\mu > 110^\circ.$$

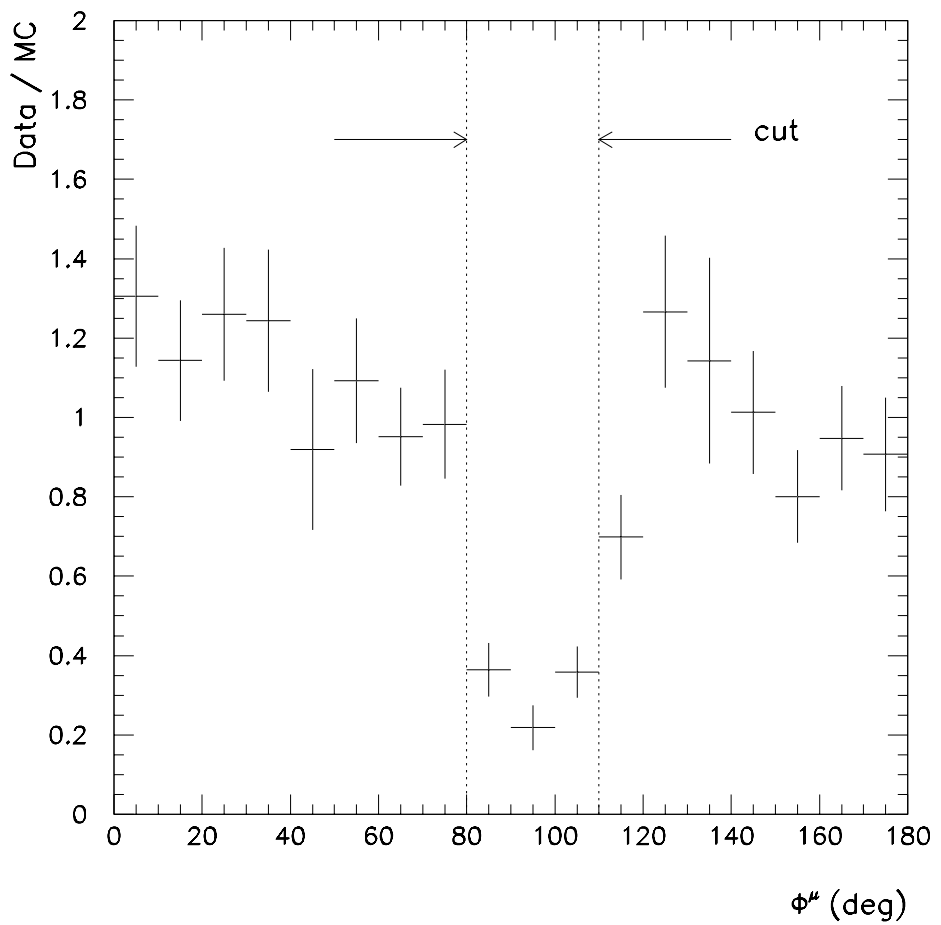


Figure 7.1: Ratio of muon ϕ -distributions from Data and Monte Carlo. The discrepancy in the region around 90° is due to radiation damage in the muon A chambers near the Main Ring pipe.

7.2.2 Jets

We impose a minimum transverse energy requirement on the highest E_T jet in the event of

$$E_T > 15 \text{ GeV}$$

to exclude jets of low trigger/reconstruction efficiency. The cut is based on studies of trigger and reconstruction efficiency which are detailed in section 8.2.

The same trigger studies also reveal a major loss of events in the forward regions, and in the region between the central and forward cryostat. To avoid this region, we reject events that do not have at least one jet with $E_T > 15 \text{ GeV}$ within

$$|\eta^{\text{det}}| < 1.0 \text{ or } 1.6 < |\eta^{\text{det}}| < 2.2.$$

The polar angle, and hence η , for this cut only is measured from the geometric center of the detector ($z = 0$). We refer to η measured this way as “detector- η ”. Usually η , sometimes referred to as “physics- η ”, is measured from the interaction vertex. The two values differ since the interaction vertex has a Gaussian distribution with $\sigma \approx 30 \text{ cm}$. The mean difference between physics and detector η in this data sample is 0.2, but for individual events the difference can be almost one unit in rapidity. We choose to parameterize this cut in terms of “detector- η ” since the affected region is fixed in η^{det} , but its location in “physics- η ” varies from event to event depending on the z -position of the interaction vertex.

7.3 Muon Quality Cuts

The following section describes the selection criteria applied to assure that where the muon momentum is successfully measured.

1. Each muon track is required to have ≥ 1 hits in all 3 layers of the muon system within a road of width 60 (150)cm in the bend (non-bend) views. This assures that a sufficient number of “points” have been measured on each muon track to accurately determine the track’s position.
2. Muons must also receive a minimum momentum “kick” of ≥ 0.6 GeV/c from the magnetic field. This corresponds a muon traversing about 90 cm in the 2 T magnetic field and an angular deflection of the muon of $\approx 0.6/p$ (GeV/c) radians. In comparison the Multiple Coulomb Scattering in the six interaction lengths (≈ 50 radiation lengths) of the muon magnet gives a RMS deflection of the muon of $\approx 0.1/p$ [61].
3. A muon track at $\eta = 0$ traverses about about 40 cm of uranium and 50 cm of copper in the calorimeter. According to the Bethe-Bloch formula [62] a muon, being a minimum ionizing particle, looses approximately 1.5 GeV in this material. Additional energy loss due to other material in the calorimeter (liquid argon, iron of the cryostat wall) and in the central detectors detector amounts to another 0.5 GeV [63].

Badly measured muons or cosmic rays can be identified by a lack of energy deposition along that calculated trajectory. Conversely, if the muon is within a jet, the jet can increase the energy deposited around

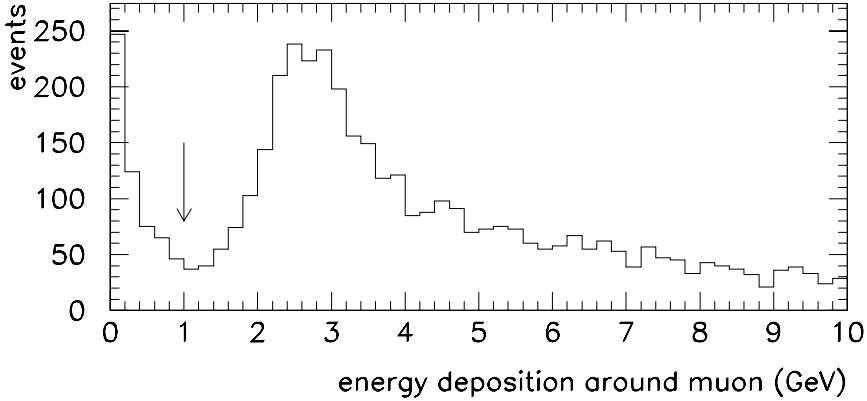


Figure 7.2: Summed energy deposition in the calorimeter cells traversed by a muon track and in the eight neighboring cells.

the muon trajectory. Figure 7.2 shows the summed energy deposited in the calorimeter cells traversed by the muon and in the eight neighboring cells. These cells form a rectangular cone of 0.3×0.3 in $\eta - \phi$ space. We have applied muon kinematic and fiducial cuts for this plot (section 7.2.1). The distribution shows a pileup of events below 1 GeV, which we attribute to mismeasurement.

We retain only muons with an energy deposition of

$$E(\Delta\eta \times \Delta\phi = 0.3 \times 0.3) \geq 1 \text{ GeV}.$$

7.4 Background Cuts

We next describe a series of cuts that eliminate muons and jets that are not produced in beam-beam interactions. The primary source of jet backgrounds is faulty readout of calorimeter cells. The primary source of muon background is cosmic rays traversing the detector.

7.4.1 Background to Jets

Electronic noise and faulty electronics in the readout of the calorimeter can simulate a jet. Three additional cuts are applied to reconstructed jets in order to remove such “fake jets”:

“Hot” calorimeter cell may contribute most if not all of the energy in the jet. To identify such jets we define a parameter $f_{\text{hot cell}}$ which is the ratio of the energies of the hottest and next hottest cell in the jet. The $f_{\text{hot cell}} < 10$ rejects 80% of such “fake” jets [64]. While actual energy profile of jets can vary significantly, some but not all of the energy of the jet should be deposited in the electromagnetic calorimeter. The fraction of the total energy in the electromagnetic calorimeter f_{EM} is required to be within

$$0.05 < f_{EM} < 0.95.$$

This cut was found to reject 95% of jets from hot cells [64].

7.4.2 Background to Muons

Below we describe several techniques which were employed to eliminate cosmic ray muons from the data.

Impact Parameter

A powerful tool for distinguishing beam-produced muons from cosmic ray muons or combinatoric background is the impact parameter, I , the distance of closest approach of a particle to the reconstructed interaction vertex. A prompt muon should have an impact parameter consistent with Multiple Coulomb Scattering in the calorimeter and the spatial resolution of the muon spectrometer.

Figure 7.3 shows I_T versus muon momentum, where I_T is the projection of the muon impact parameter in the transverse plane (the non-bend view in the spectrometer). I_T is obtained by extrapolating the track measured in all three layers of the muon system back towards the interaction vertex.

The seven interaction lengths (210 radiation lengths) of the calorimeter and muon magnet introduce an rms angular deflection of $0.23/p$ radians. The corresponding impact parameter is $(100/p)$ cm, for $|\eta| = 0$. The intrinsic spatial resolution in the non-bend plane is determined by the muon pad measurement and is about 1.6 mm (section 3.5), with an additional 3 mm uncertainty from the muon chamber alignment; the resulting resolution on I_T is ≈ 2 cm.

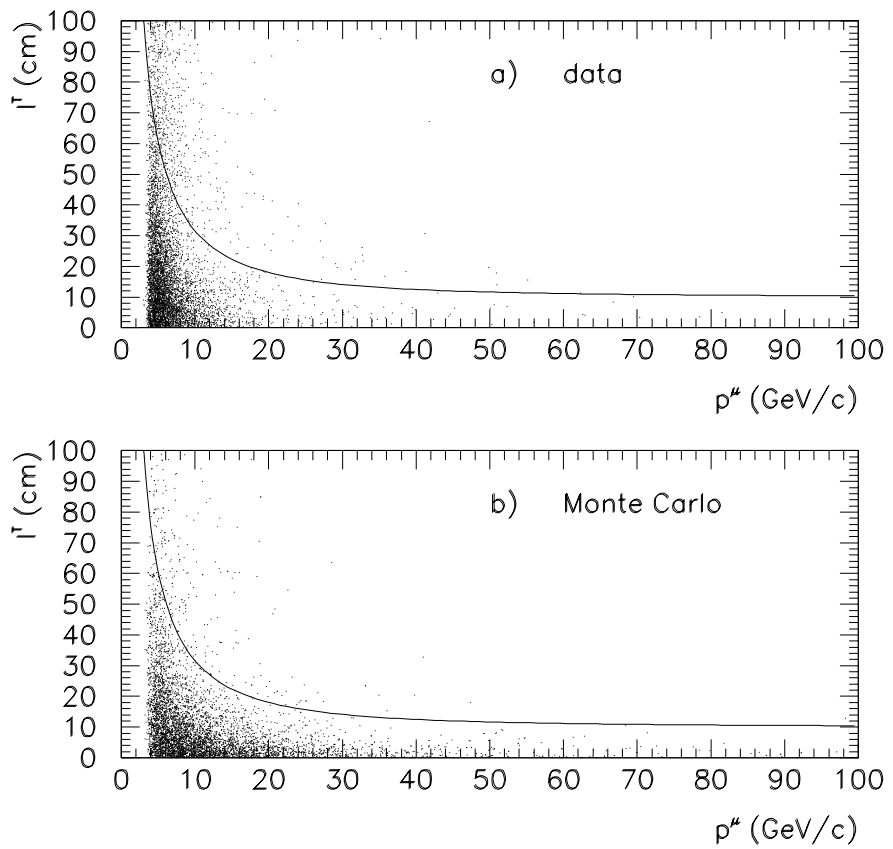


Figure 7.3: Impact parameter I_T in the transverse (non-bend) plane as a function of muon momentum for (a) data and (b) Monte Carlo. Kinematic, fiducial and muon quality cuts have been applied. The curve shows the cut $I_T = \sqrt{(300/p)^2 + 100}$ cm.

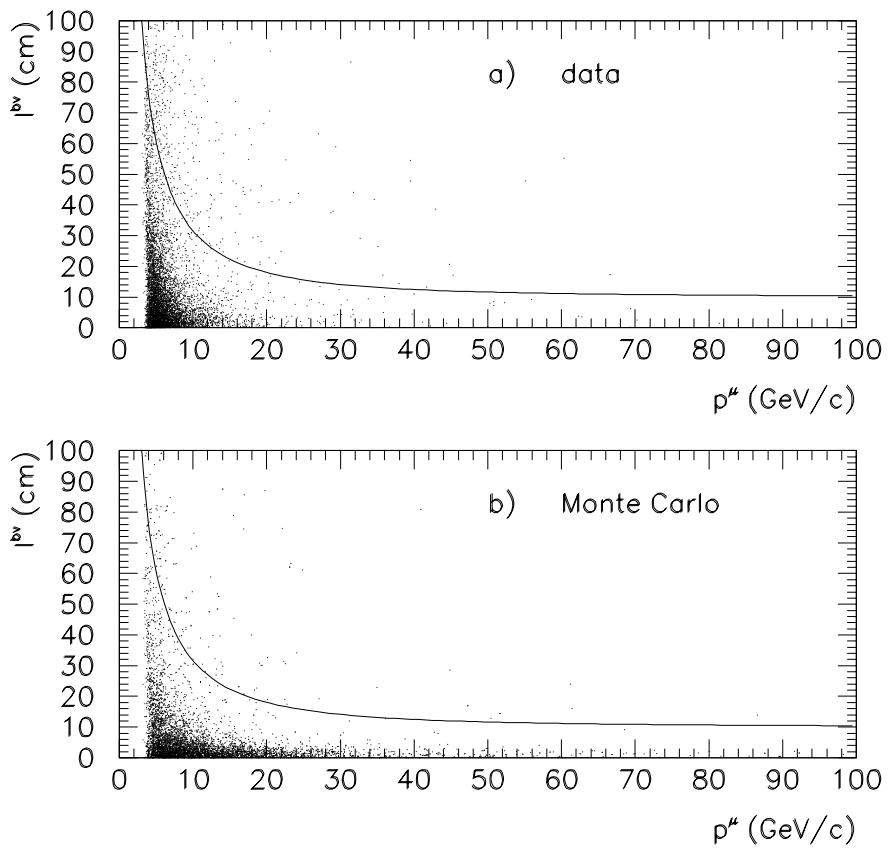


Figure 7.4: Bend view impact parameter I_{bv} as a function of muon momentum for (a) data and (b) Monte Carlo. Kinematic, fiducial and muon quality cuts have been applied to both samples. The curve shows $I_{bv} = \sqrt{(300/p)^2 + 100}$ cm.

Figure 7.3 shows (a) data and (b) Monte Carlo events. Kinematic, fiducial and the muon quality cuts described above have been applied. Both the data and the Monte Carlo events show the expected $1/p$ -dependence of the impact parameter distribution. Figure 7.4 shows the same plot for the bend view impact parameter I_{bv} , where I_{bv} is calculated from the muon trajectory reconstructed from muon spectrometer data.

Based on the uncertainties discussed above the following cuts were applied to the muon tracks:

$$I_T, I_{bv} < \sqrt{(300/p)^2 + 100} \text{ cm},$$

was used where p is the momentum in GeV/c. A total of 4% of the Monte Carlo events fails this cut. The events in figs 7.3 and 7.4a) outside the cuts for low p^μ are due to cosmic rays and mismeasured muons.

The cuts on I_T (I_{bv}) reject 4% (3%) of Monte Carlo events, the combined cuts reject a total of 6% of the Monte Carlo sample.

Correlation of Timing in the Muon Chambers

We reject cosmic rays and accidental background based on the coincidence in time of the muon with the beam crossing. This is done by refitting the muon track while leaving the beam crossing time T_0 as a free parameter. Figure 7.5 shows the ΔT_0 distribution for a) data and b) cosmic ray muons, where the latter were recorded using the physics triggers without beam.

The ΔT_0 -distribution for cosmic events is not flat because the muon system timing and the reconstruction are optimised for data and are hence more

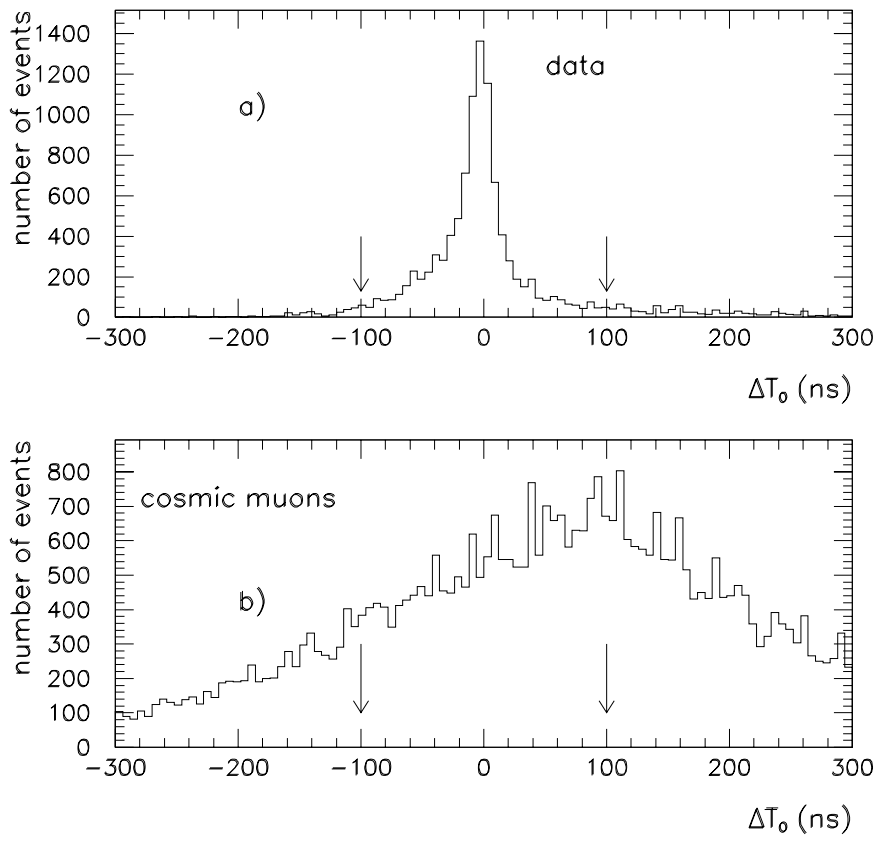


Figure 7.5: The time difference between the actual and fitted T_0 values, ΔT_0 , for muon tracks for a) beam data and b) cosmic rays. All cuts (table 7.1) have been applied to the beam data; to the cosmic data only fiducial and kinematic cuts were applied.

efficient for muons in coincidence with the open gate. A cut of $|\Delta T_0| < 100$ ns is applied in the event selection; this rejects 10% of the events shown in fig. 7.5(a) and 60% of those in the cosmic sample (fig. 7.5(b)).

Matching Track in the Central Detector

For each muon candidate the polar ($\Delta\Theta$) and azimuthal ($\Delta\phi$) angle match between the muon chamber track and the closest track in the central detector is computed. Figs 7.6, shows the polar and azimuthal angle matches for data and Monte Carlo events. All selection criteria previously discussed have been applied to both sets of data. The two distributions are similar, with the Monte Carlo distribution being slightly narrower, indicating that the data is consistent with muon emission from a beam-beam interaction.

In order to minimize the probability of an incorrect match we require $\Delta\Theta < 0.1$ radians and $\Delta\phi < 0.15$ radians. The Monte Carlo predicts a loss of $\approx 9\%$ in acceptance from the $\Delta\Theta$ -cut alone, and a total loss of 20% from both cuts.

7.5 Summary

A total of 7556 events pass all cuts, including 22 events in which two muons pass the cuts. Table 7.1 summarizes the cuts and the number of events remaining after each cut. Figures 7.7 and 7.8 show the p_T and η of all muons and of the highest E_T jet in each event after cuts. The discontinuity in the muon η -distribution at $|\eta| \approx 0.3$ in fig. 7.7b) is due to a change in acceptance

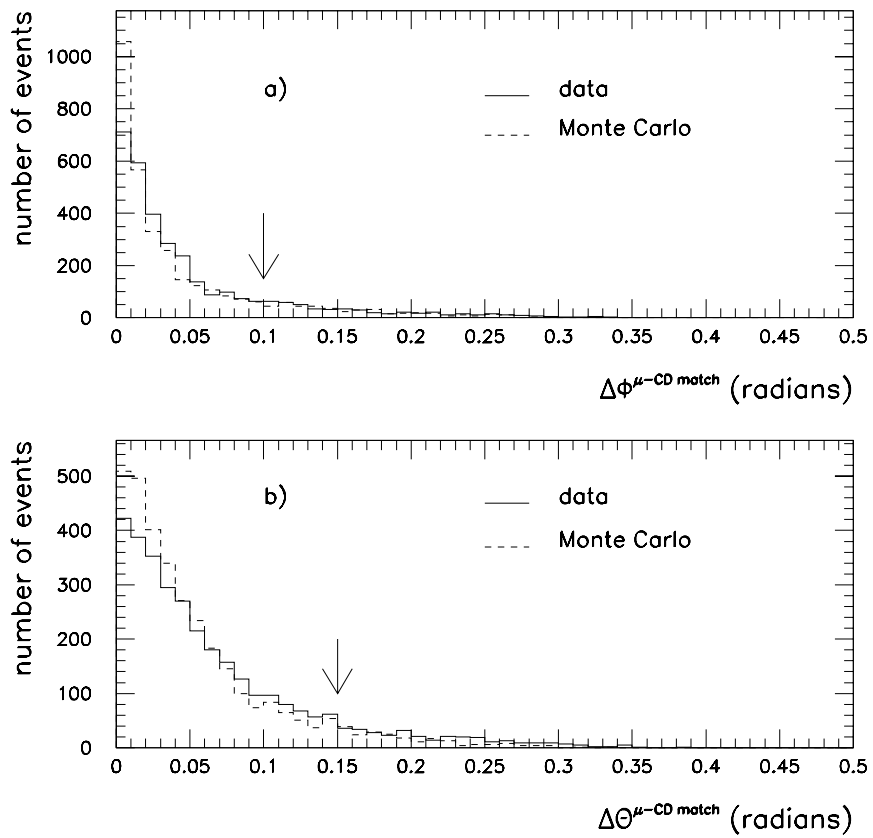


Figure 7.6: Angular separation in Θ and ϕ of the track reconstructed in the muon detector and the closest track in the central drift chamber.

description of cuts		remaining events
triggers collected		
muon kinematic & fiducial		$p_t^\mu > 3 \text{ GeV}/c$
		$ \eta < 0.8$
		$\phi^\mu < 80^\circ \text{ or } \phi^\mu > 110^\circ$
jet kinem. & fiducial		$E_t^{\text{highest jet}} > 15 \text{ GeV}$
		$ \eta^{\text{jet}} < 1.0 \text{ or } 1.6 < \eta^{\text{jet}} < 2.2$
muon quality	3-layers	hits in A B and C-layers
	mag. field traversed	transverse momentum “kick” $> 0.6 \text{ GeV}$
	calorimeter deposition	$E(\Delta\eta \cdot \Delta\phi = 0.3 \cdot 0.3) > 1 \text{ GeV}$
jet quality	hot cell	$f_{\text{hot cell}} < 10$
	electromagnetic fraction	$0.05 < f_{\text{EM}} < 0.95$
	coarse hadronic fraction	$f_{\text{CH}} < 0.4$
muon background	impact parameter	$I_T < \sqrt{(300/p)^2 + 100} \text{ cm}$ $I_{\text{bend-view}} < \sqrt{(300/p)^2 + 100} \text{ cm}$
	timing	$ \Delta T_0 < 100 \text{ ns}$
	CD track match	$\Delta\Theta^{\mu-\text{CD track}} < 0.15 \text{ rad}$ $\Delta\phi^{\mu-\text{CD track}} < 0.10 \text{ rad}$

Table 7.1: Summary of Muon and Jet Selection Cuts

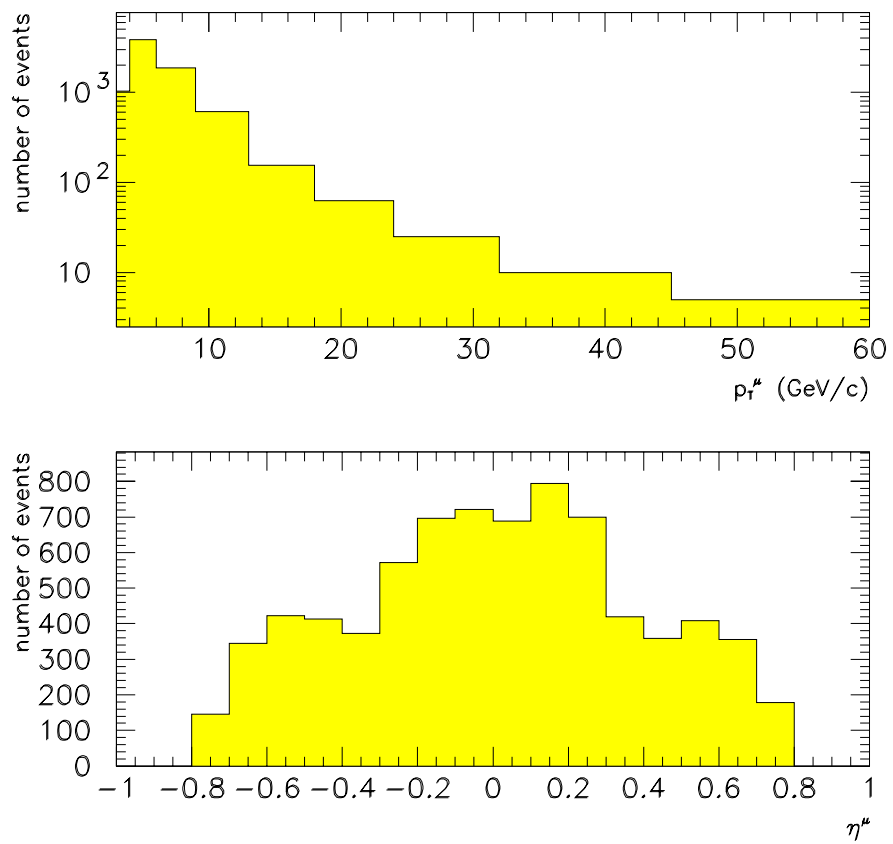


Figure 7.7: p_T and η -distributions of all muons in the data sample after selection cuts.

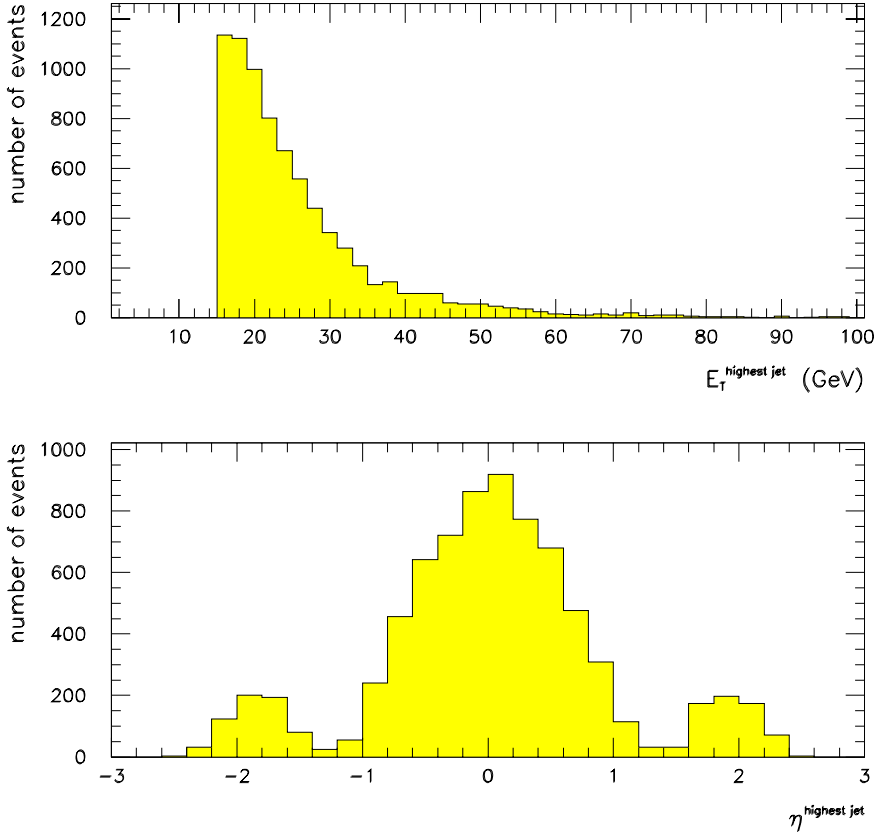


Figure 7.8: E_T and η -distribution of the jet with the highest transverse energy in the event after selection cuts.

for muons with 3-layer tracks. The dip at $|\eta| \approx 1.5$ of the jet η -distributions in fig. 7.8 is due to the fiducial cut in the pseudorapidity described in section 7.2.2. Figure 7.9 displays a typical event passing all cuts. It shows the upper north side of the yz (bend) view of the detector. The event contains a $6 \text{ GeV}/c$ muon within an 11 GeV jet. The muon track shown in the event display is calculated from data in the muon chambers and is extrapolated toward the

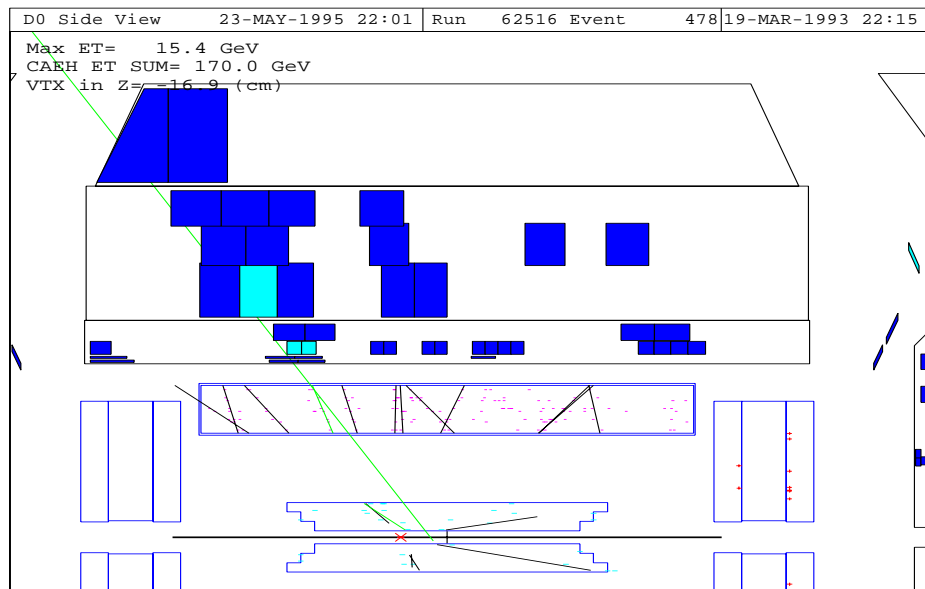
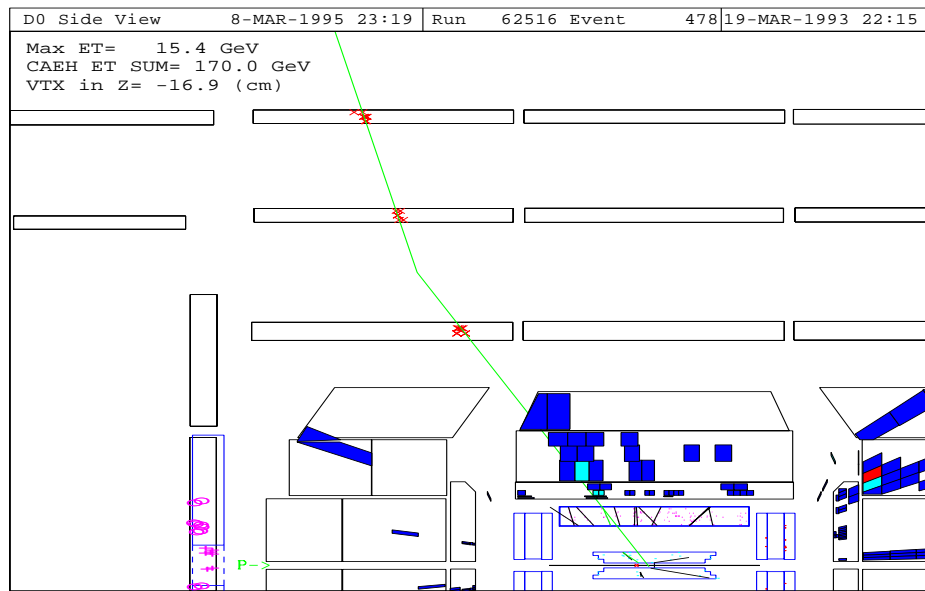


Figure 7.9: Event display of a 6 GeV/c muon within an 11 GeV jet. The bottom figure shows a blowup of the calorimeter and central detectors.

event vertex. There a matching central detector track can be seen in the central detector as well. For the muon momentum measurement the muon trajectory was recalculated incorporating the matching central detector track (section 5.3). The muon track has hits in all three layers of the muon system. The energy depositions in the individual cells in the calorimeter as well as tracks reconstructed in the central drift chamber and the vertex detector are clearly visible.

As a final check of the quality of the selected muons selected, a subsample of 109 events of the final data set has been visually scanned. Two events may contain muons from cosmic rays. These two events have hits in the muon chambers and tracks in the central detector consistent with a cosmic ray passing near the interaction vertex.

Chapter 8

Efficiencies

8.1 Introduction

The object of this study is to determine the b -quark production cross section within a given p_T and η range. This cross section is inferred from the measured production rate for muons in association with jets. However, the final sample of muon-jet data described in chapter 7 represents only a small fraction of the b -quarks which were produced with a muon-jet topology when the data were recorded .

Event losses occur for a variety of causes:

- detector acceptance is not uniform over 4π , for example there are gaps between the central and forward detector components.
- detector efficiency varies; consider for example the damage to the muon chambers in the vicinity of the main ring beampipe (section 7.2.1).

- events are lost when the reconstruction program fails to determine the correct muon momentum or jet energy.
- the selection cuts described in chapter 7 reject a large fraction of the $b \rightarrow \mu + \text{jet}$ events in the data sample.

In order to infer a cross section from the final event sample the losses due to these and other factors must be understood and evaluated. In this chapter we attempt to quantify these loss factors through the study and comparison of recorded data and events simulated by the b -quark Monte Carlo (chapter 6), and as a check with c -quark Monte Carlo. With the exception of the level 1 jet trigger efficiency, the results of the efficiency studies were the same for b and c -quark Monte Carlo samples. However, as described below the comparison of recorded and simulated events discloses inefficiencies in the detector and trigger which were not programmed into the Monte Carlo.

The results of this study are used to “correct” the Monte Carlo so that it more closely reproduces the detector and trigger characteristics. This is necessary since the Monte Carlo is an essential tool for translating the measured event rate into a b -quark cross section.

We characterize the losses which occur at different stages of data acquisition and processing in terms of efficiencies. The “efficiency” for a muon is defined as the probability that a muon will survive a particular process such as the trigger (ϵ_T^μ) or the reconstruction (ϵ_R^μ). The overall muon efficiency, ϵ^μ , is the probability that the muon is accepted into the final analysis sample and

is the product of the individual efficiencies.

$$\epsilon^\mu = \epsilon_T^\mu \cdot \epsilon_R^\mu \cdots \quad (8.1)$$

The efficiencies are calculated separately as functions of p_T^μ / E_T^{jet} . The determination of these efficiencies is described in detail below.

8.2 Jet Efficiency

8.2.1 Jet Trigger Efficiencies

The efficiency of the level 1 jet trigger (section 4.2) is calculated using a set of events recorded with an inclusive muon trigger. When a jet is reconstructed in this data we check for a corresponding L1 (level 1) trigger defined as a trigger tower within $\Delta R = 0.7$ of the axis of the jet. Fig. 8.1 shows the resulting jet efficiencies as a function of η^{det} , where η^{det} is the pseudorapidity measured relative to an origin at the center of the detector ($z = 0$). Only jets with $E_T > 20 \text{ GeV}$ are plotted in order to minimize energy threshold effects. The same quantity is also shown for the $b \rightarrow \mu + \text{jet}$ Monte Carlo.

Two features are obvious from fig. 8.1:

1. The data show a major loss of events around $|\eta| = 1.3$.
2. The Monte Carlo does not reproduce the observed loss of events.

The effect described in item 1 is due to inadequate instrumentation of the trigger for the region between the central and forward calorimeters. As

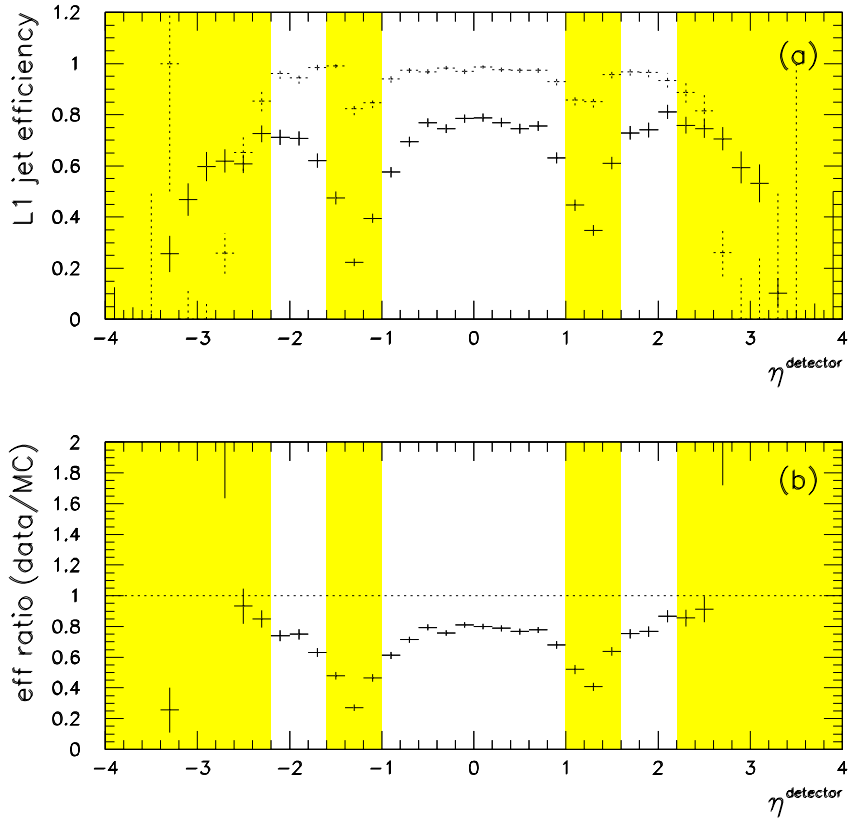


Figure 8.1: (a) Level 1 trigger efficiency for reconstructed jets with $E_T > 20$ GeV. The solid points show the efficiency obtained from inclusive muon data, while the dotted points are from Monte Carlo. Fig. (b) shows the ratio of data/Monte Carlo. Jets in the shaded regions ($1.0 < |\eta| < 1.6$ and $|\eta| > 2.2$) are not included in the analysis.

mentioned in section 7.2.2 we avoid this region of poor efficiency, by excluding jets within the range $1.0 < |\eta| < 1.6$. The region $|\eta| > 2.2$, which, as evident from fig. 8.1 is poorly understood, is also excluded.

Fig. 8.2 shows the L1 trigger efficiency for jets as a function of the reconstructed E_T . The slow “turnon” of the efficiency is due to the narrowness of the trigger tower ($\Delta\eta \times \Delta\phi = 0.2 \times 0.2$) which covers only 3% of the volume of a jet of cone $\Delta R = 0.7$. (Section 4.6). The disagreement between the efficiency calculated from the data and from Monte Carlo is believed to be due to an error in the calorimeter energy scale at the trigger level. As seen in the figure, agreement is achieved with the assumption that the actual threshold is 4.25 GeV. This threshold value is used in subsequent Monte Carlo calculations. Fig. 8.2 is for the region $|\eta| < 1.0$, but the same adjustment in threshold also achieves agreement in the forward region $1.6 < |\eta| < 2.2$.

Figure 8.3 shows the L2 trigger efficiency for jets that passed the L1 trigger, as a function of the reconstructed jet E_T . Below 10 GeV the data points systematically exceed the Monte Carlo points by a few percent, but agreement is excellent at $\approx 100\%$ efficiency above 15 GeV. Figure 8.4 shows the overall jet trigger efficiency ($L1 \times L2$) as a function of the reconstructed E_T of the most energetic jet in the event; the efficiencies from data and Monte Carlo are compared. This efficiency is higher than the trigger efficiency for individual jets (figures 8.2 and 8.3) because there are typically (in $\approx 90\%$ of the events) two or more jets in an event, either of which may satisfy the trigger. The efficiencies derived from data and the $b \rightarrow \mu X$ Monte Carlo agree within 5%. However, the efficiency for the $c \rightarrow \mu X$ Monte Carlo is about 10% higher than the data.

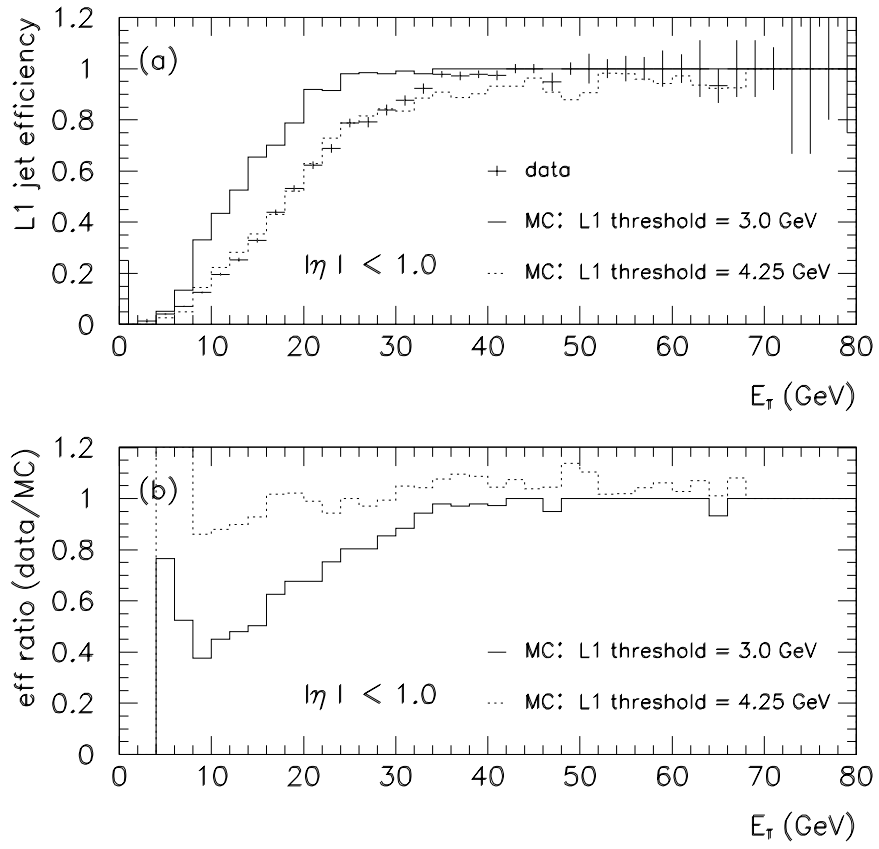


Figure 8.2: (a) Level 1 trigger efficiency for reconstructed jets as a function of jet- E_T , for jets with $|\eta| < 1.0$. The Monte Carlo is shown for trigger tower thresholds of 3.0 and 4.25 GeV. Fig. b) shows the ratio of data: Monte Carlo efficiencies for both thresholds.

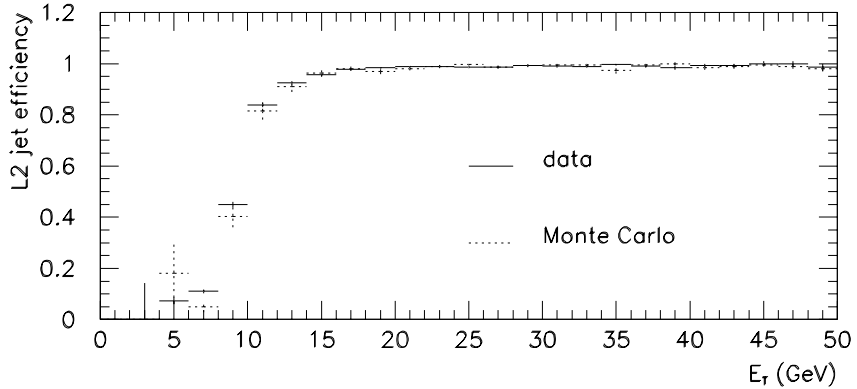


Figure 8.3: Level 2 jet efficiency as a function of the E_T of the reconstructed jet.

Although the amount of b production in the data exceeds c production, we conservatively assign a 10% uncertainty to the jet trigger efficiency.

On the basis of these comparisons we imposed the $E_T > 15 \text{ GeV}$ cut on the highest E_T jet in the event.

8.2.2 Jet Reconstruction Efficiency

The jet reconstruction efficiency has been determined from Monte Carlo events. We reconstruct jets from the particle four-vectors generated by the ISAJET Monte Carlo program. We then check what fraction of these jets are found once the Monte Carlo has been processed through the GEANT detector simulation and the offline reconstruction programs.

The “ISAJET” jets are formed from the particle four-vectors using a cone algorithm comparable to the one in the reconstruction. The jets

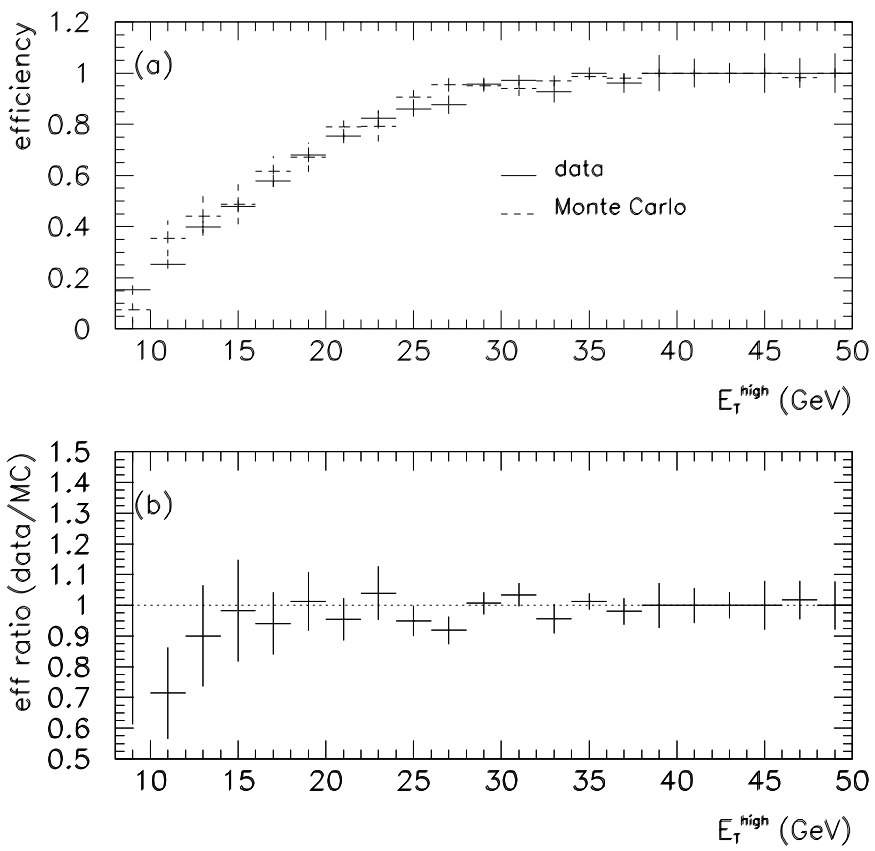


Figure 8.4: Overall jet trigger efficiencies as a function of E_T of the highest E_T jet in the event. The efficiency obtained from the inclusive muon sample is compared to the Monte Carlo result.

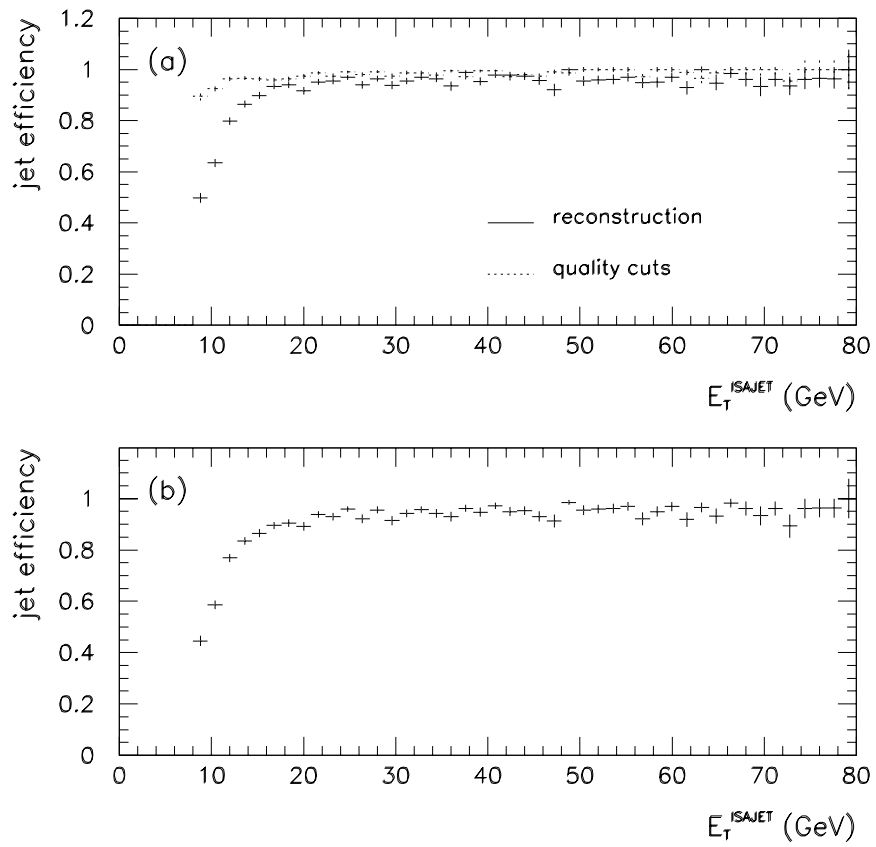


Figure 8.5: Jet Reconstruction and offline quality cut efficiencies from Monte Carlo. a) The solid histogram indicates the reconstruction efficiencies, while the dotted histogram indicates the efficiency of the offline cuts. b) shows the combined reconstruction and offline jet quality cut efficiencies.

reconstructed with the standard reconstruction program using GEANT information, are compared with the ISAJET jets. If the axes of an ISAJET and reconstructed jet are within $\Delta R \leq 0.7$ the jet is defined as reconstructed. The calculated jet reconstruction efficiency (fig. 8.5a) is constant at 95% for $E_T > 15 \text{ GeV}$. The error in the jet reconstruction efficiency has been estimated by comparing the result of this study with another independent, but also Monte Carlo based analysis using the HERWIG [67] event generator [68]. The difference of $\approx 5\%$ has been taken as the systematic error in the jet reconstruction efficiency.

8.2.3 Efficiency of Jet Quality and Fiducial Cuts

The efficiency of the jet quality cuts (section 7.2.2) has been determined the same way as the reconstruction efficiency, i.e by comparison to ISAJET-jets, and is also plotted in fig. 8.5a). It agrees to within 4% with a more detailed study based on data [69]. The systematic error on the efficiency of the jet quality cuts is taken as 4%. Figure 8.5(b) shows the combined efficiency for jet reconstruction and quality cuts.

Finally we examine event losses due to the exclusion of jets in the $|\eta|$ -ranges 1.0-1.6 and $|\eta| > 2.2$ (section 7.2.2). This is done with a sample of Monte Carlo events to which no η -cuts have been applied.

In figure 8.6 the abscissa shows the transverse energy of the highest E_T reconstructed jet in the event, while the ordinate shows the transverse energy of the highest E_T reconstructed jet within $|\eta| < 1.0$ or $1.6 < |\eta| < 2.2$. Events

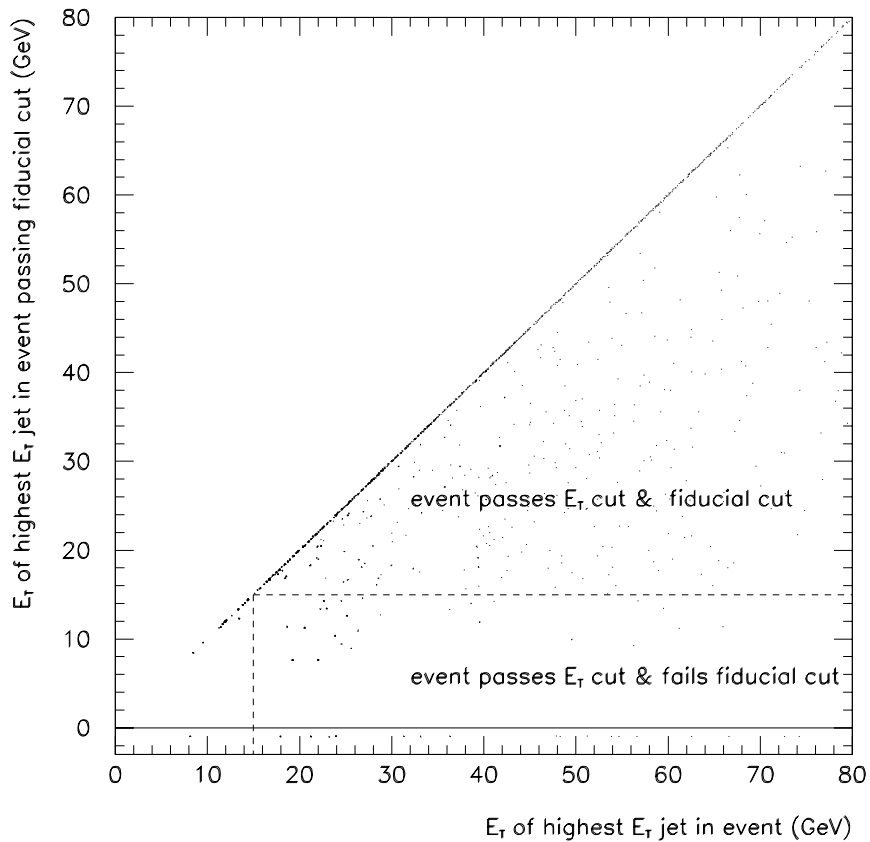


Figure 8.6: Efficiency of the jet fiducial cut in η for the Monte Carlo. The abscissa shows the transverse energy of the highest E_T jet in the event, while the ordinate shows the transverse energy of the highest E_T jet within $|\eta| < 1.0$ or $1.6 < |\eta| < 2.2$.

where the leading jet is within the accepted $|\eta|$ -region lie on the diagonal of the plot. Below the diagonal but above the abscissa are events where a lower E_T jet in the event is within the accepted $|\eta|$ -region. Events with no jet within $|\eta| < 1.0$ or $1.6 < |\eta| < 2.2$ are plotted below the $y = 0$ line. The efficiency for the fiducial cut can be obtained by dividing the number of events passing the fiducial cut as well as the minimum E_T cut by the number of all events passing the minimum E_T cut. The cut is 97% efficient, independent of E_T . We use the statistical error of 5% due to Monte Carlo statistics as the systematic error on this quantity.

We add to this in quadrature the 4% systematic error in the jet quality cuts to obtain a 6% systematic error on the jet offline cut efficiency.

8.2.4 Overall Jet Efficiencies

Figure 8.7 shows the combined jet efficiency, including trigger, reconstruction and offline cuts, for Monte Carlo. The error of 13% in the efficiency includes 10% for trigger efficiency, 5% for reconstruction efficiency, 6% for the uncertainty in the jet offline cuts. The shape of the efficiency curve is dominated by the level 1 jet trigger efficiency. A minimum E_T -threshold of 15 GeV imposed on the highest E_T jet in the event avoids the region of very small efficiencies for soft jets.

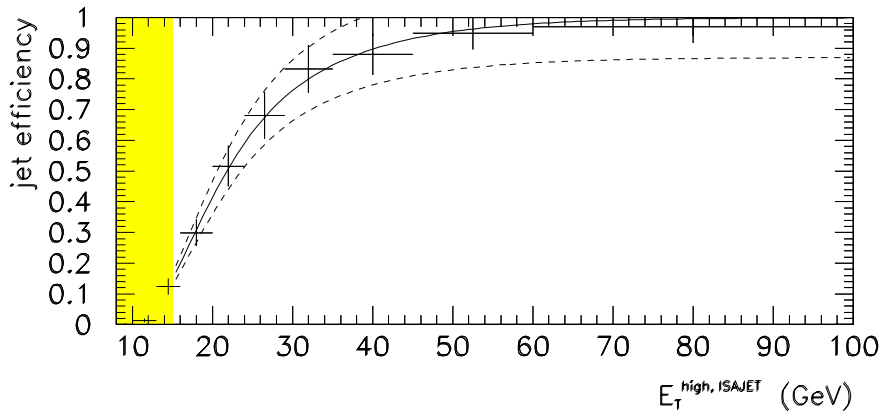


Figure 8.7: Combined jet efficiency, including trigger, reconstruction and off-line cuts, for Monte Carlo events. The efficiency is parameterized in terms of the E_T of highest jet generated by ISAJET. The dashed lines show the uncertainty in the jet efficiency. The shaded region denotes the region excluded by the 15 GeV minimum E_T -cut. The solid line is a fit through the data points, the dotted lines indicate an uncertainty of 13%.

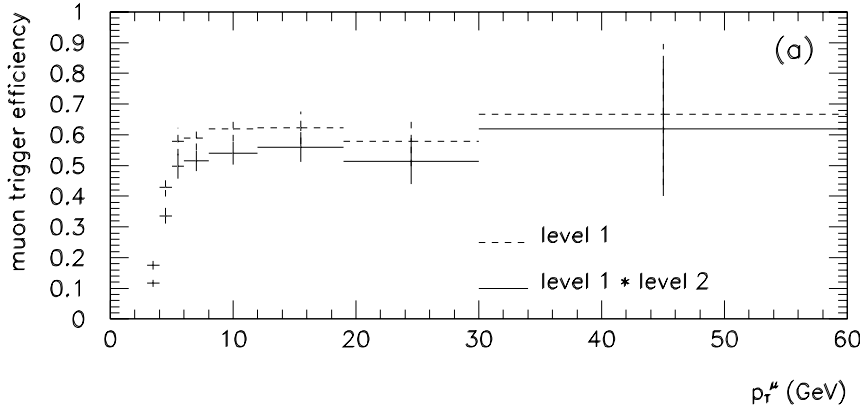


Figure 8.8: Muon trigger efficiency from Monte Carlo. The efficiency is plotted as a function of the transverse momentum of the muon as generated in ISAJET.

8.3 Muon Efficiencies

8.3.1 Muon Trigger Efficiency

The Monte Carlo muon trigger efficiencies for the L1 and L2 trigger are shown in fig. 8.8. It is the fraction of muons generated in the ISAJET Monte Carlo that satisfy the trigger ($E_T > 10$ GeV). The trigger efficiency rises sharply between 3.5 and 5 GeV/c and plateaus a little above 50%. The uncertainty in the L1 muon trigger efficiency was obtained from a study of data collected with a jet trigger. The fraction of muons that were reconstructed in that data sample which satisfied the muon L1 trigger was compared with the equivalent quantity from the Monte Carlo; the muon L1 efficiency from Monte

Carlo was 10% higher than from the data sample [70]. On this basis we assume a 10% systematic error on the L1 muon trigger efficiency. A major contribution to the inefficiency in the muon trigger is the limited geometric acceptance in the bottom in the detector due to the calorimeter support structure.

8.3.2 Muon Reconstruction Efficiencies

The Monte Carlo muon reconstruction efficiency, the probability that a post-trigger muon is reconstructed offline, is shown in fig. 8.9 as a function of the muon transverse momentum and pseudorapidity. A muon is considered to be reconstructed if its original and reconstructed directions are within $\Delta R = 0.7$. The calculated reconstruction efficiency is close to 100%, which is not surprising considering the similarity of the software used in the L2 trigger and offline reconstruction programs.

However, visual scanning of actual events which pass the muon L2 trigger give a value of $95 \pm 3\%$ for the muon reconstruction efficiency [33]; this value is taken as the muon reconstruction efficiency.

8.3.3 Muon Offline Cut Efficiencies

Following offline reconstruction of the muon a series of cuts were applied to the data to eliminate mismeasured muons and cosmic ray background (section 7.3 and 7.4). As noted in section 7.4 a visual scan of a subset of the final data set established that background contamination is less than 2%. We have compared data and Monte Carlo events to check if the effect of these cuts is

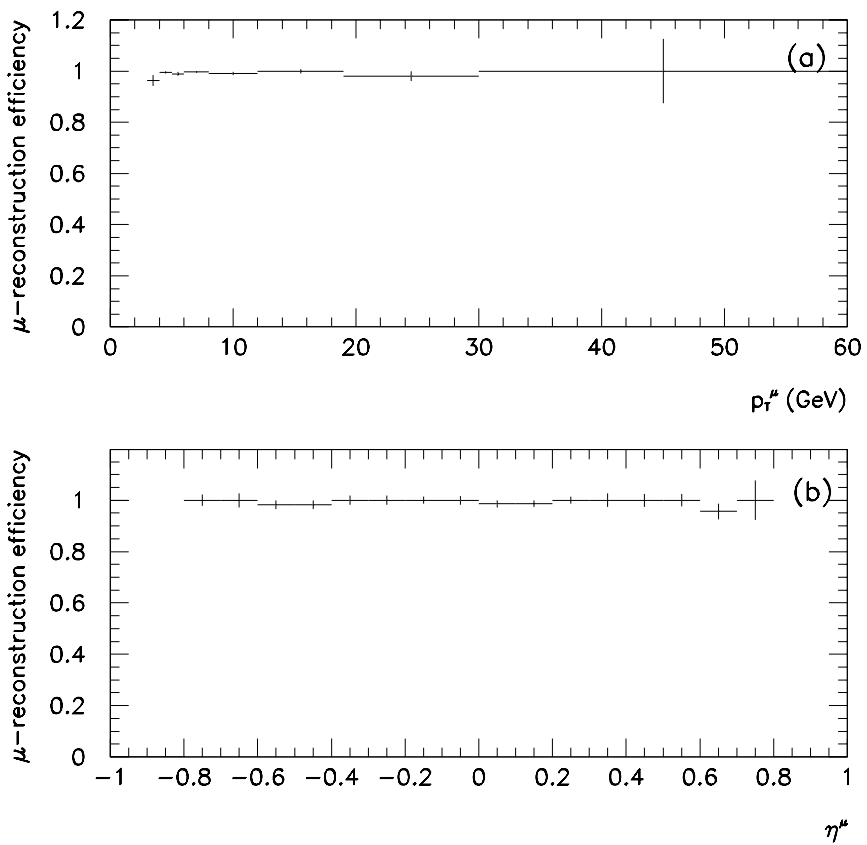


Figure 8.9: Muon reconstruction efficiency from Monte Carlo. The efficiency is plotted as a function of (a) p_T^μ and (b) η^μ

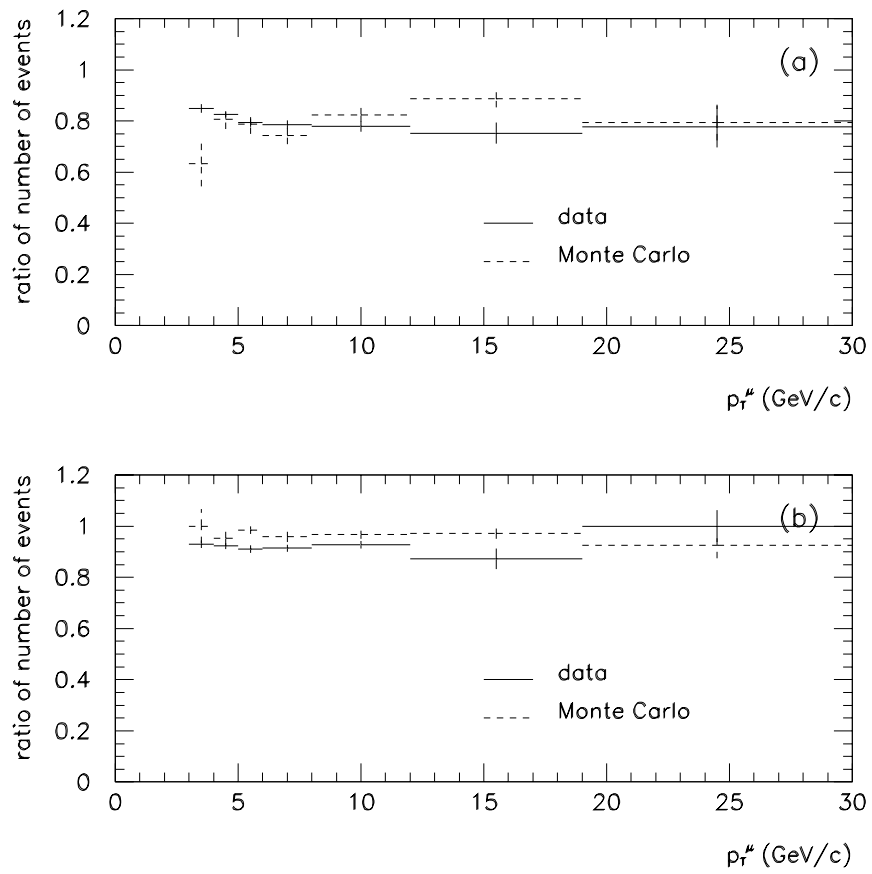


Figure 8.10: Efficiency comparison of data and Monte Carlo for a) the “three layer requirement” and (b) the central track match requirement.

	cuts	data	Monte Carlo	data / Monte Carlo
1	calorimeter dep.	0.990 ± 0.002	0.995 ± 0.005	0.995 ± 0.005
2	3-layer tracks	0.801 ± 0.007	0.81 ± 0.02	0.99 ± 0.03
3	p_T -“kick”	0.953 ± 0.004	0.952 ± 0.008	1.00 ± 0.01
4	impact parameter	0.913 ± 0.006	0.953 ± 0.009	0.96 ± 0.01
5	central detector track	0.918 ± 0.006	0.969 ± 0.008	0.95 ± 0.01
6	floating time	0.904 ± 0.007	0.79 ± 0.002	1.14 ± 0.009

Table 8.1: Comparison of the efficiency for the offline cuts in the data and Monte Carlo for $p_T^\mu > 4 \text{ GeV}/c$.

correctly reproduced in the Monte Carlo. From both Monte Carlo and data a subset of events with the best measured muons is selected; this ensures a negligible component of background muons in the data. Each cut is released in turn and the fraction of events lost in the Monte Carlo and data is noted. Figure 8.10 shows examples of two of these studies; a) the three-chamber layer requirement and b) the CD matching track requirement. Figure 8.10(a) shows that the three chamber layer requirement is well modelled by the Monte Carlo.

The muon efficiencies, listed in table 8.1, are determined are constant in p_T^μ above $4 \text{ GeV}/c$ and are estimated by fitting a constant function to that data/Monte Carlo efficiency ratio in that region. Agreement between the data and Monte Carlo is excellent for the first three factors listed in table 8.1. The discrepancies for the impact parameter and CD match may be due to factors such as errors in in detector alignment parameters, double interactions and CD inefficiency. Finally the 14% disagreement in item 6 is ascribed to an error

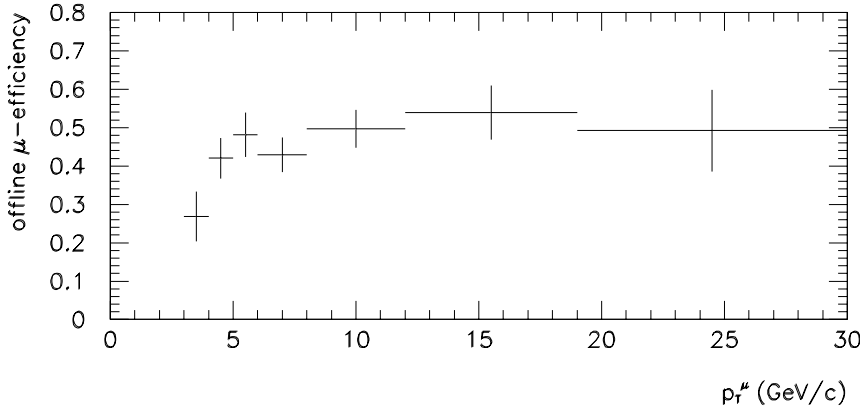


Figure 8.11: Efficiency of the offline muon cuts as a function of the measured muon transverse momentum. The plot shows the Monte Carlo efficiencies corrected with the factor “data/Monte Carlo from table 8.1.

in the Monte Carlo simulation giving erroneous efficiencies for the efficiencies of the floating time cut. The Monte Carlo efficiencies are corrected by the factors in the last column. We have thus used the Monte Carlo to simulate the correlation of the efficiencies of the cuts but have taken the efficiencies of the individual cuts from the data.

The fraction of reconstructed events surviving the offline muon cuts is plotted in fig. 8.11 as a function of the measured muon transverse momentum. The efficiency rises sharply between 3 and 5 GeV and plateaus around 50%. The error in the efficiency was taken as 8% from the sum of the errors in the correction factors listed in table 8.1.

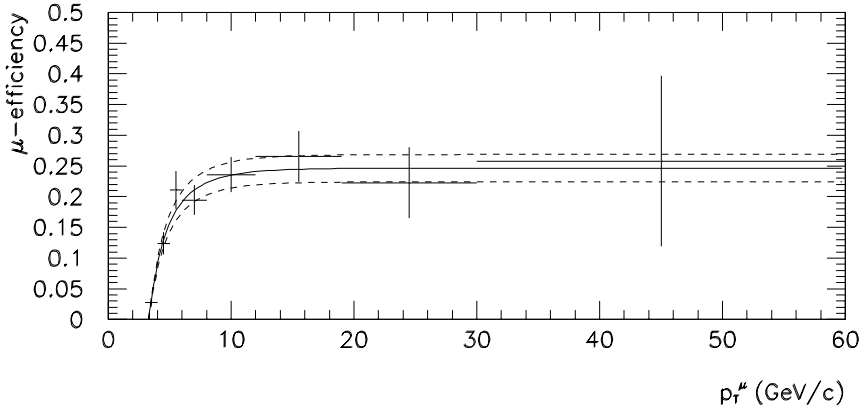


Figure 8.12: Overall muon efficiency. The dotted lines show the 13% systematic error.

8.3.4 Overall Muon Efficiency

The overall muon efficiency is shown in figure 8.12. It is the product of the muon trigger efficiency (fig. 8.8(a)), the muon reconstruction efficiency (95%, independent of p_T^μ), section 8.3.2) and the muon offline efficiencies (fig. 8.11). It is constant at 22% for transverse momenta of 8 GeV/c and higher. The error in the total muon efficiency is taken to be 13%, which is the sum in quadrature of the muon trigger, reconstruction and offline efficiencies.

8.4 Summary

Table 8.2 shows a summary of the efficiencies and their uncertainties. The table shows the approximate transverse momenta for muons, or transverse energies for jets, above which the efficiency is independent of p_T or E_T , as

efficiency	plateau threshold	plateau efficiency (%)	Method	systematic error (%)
μ trigger	≈ 6 GeV/c	52	MC	10
μ reconstruction	\approx flat in p_T	95	data	3
μ offline	≈ 5 GeV/c	50	data	8
jet trigger	≈ 30 GeV	100	MC	10
jet reconstruction	≈ 15 GeV	95	MC	5
jet offline	≈ 10 GeV	97	MC	6

Table 8.2: Efficiencies for muons and jets

well as the efficiency on the plateau. Also listed are the uncertainties for each of the efficiencies. We assume that there is no correlation between trigger, reconstruction and offline efficiencies and take the total systematic error in the efficiencies as the sum in quadrature of the individual contributions. The systematic error in the efficiencies is hence 18%.

We have now determined efficiencies for the muons and jets in the data sample. The muon efficiency is a function of the transverse momentum of the muon (p_T^μ) (fig. 8.12), while the jet efficiency is parameterized in terms of the transverse energy of the highest E_T jet (E_T^{high}) in the event (fig. 8.7). The efficiency of a muon-jet event is now:

$$\epsilon = \epsilon^\mu(p_T^\mu) \cdot \epsilon^{\text{jet}}(E_T^{\text{high}}) \quad (8.2)$$

where $\epsilon^\mu(p_T^\mu)$ and $\epsilon^{\text{jet}}(E_T^{\text{high}})$ are parameterizations of figures 8.12 and 8.7 respectively. Knowing the efficiency and the luminosity of the data sample (section 4.2), we are now prepared to extract the cross section for the muon-jet events in the data sample..

Chapter 9

The Muon Spectrum

9.1 Introduction

In chapter 7 we described a data sample of 7578 beam produced muons in 7556 events enriched in b -quark production. 22 events contain two muons. The goal now is to determine the cross section for b -quark production. We will proceed in three steps:

1. measure the differential cross section $d\sigma/dp_T^\mu$ for muon-jet events by weighting the data by the inverse of the efficiencies and the integrated luminosity $((\epsilon\mathcal{L})^{-1})$.
2. determine the differential cross section $d\sigma/dp_T^\mu$ of the events in 1 that are due to b/\bar{b} -production. We use the event kinematics to separate b -quark production from c -quarks and π/K -background. Cross sections for W and Z -production are obtained from DØ measurements and are subtracted.

3. use a Monte Carlo based conversion to transform $d\sigma/dp_T^\mu$ for b -production into the b -quark production cross section,

We describe steps 1 and 2 in this chapter, while step 3 is explained in chapter 10.

9.2 Differential Muon Cross Section for μ -Jet Events

We now calculate $d\sigma/dp_T^\mu$ for muon-jet events by dividing the observed yield by the efficiencies for trigger, reconstruction and selection cuts.

From the integrated luminosity $\int \mathcal{L} dt = 228 \text{ nb}^{-1}$ (chapter 4), we can determine the differential cross section, $d\sigma/dp_T^\mu$, as a function of the transverse momentum of the muons using the relation

$$\frac{d\sigma}{dp_T^\mu} = \frac{1}{\epsilon \int \mathcal{L} dt} \frac{dN^\mu}{dp_T^\mu} \quad (9.1)$$

where dN/dp_T^μ denotes the observed distribution of the number of muons. We histogram the muon p_T in variable bin sizes compatible with, i.e. equal or greater than, the momentum resolution for a given range of p_T^μ . The binning varies from 1 GeV/c at 3 GeV/c to 15 GeV/c for the highest p_T muons (45 to 60 GeV/c). The differential cross section is obtained by weighting each event by the factor $(\epsilon \int \mathcal{L} dt)^{-1}$:

$$\frac{d\sigma}{dp_T^\mu} = \frac{1}{\Delta p_T^\mu \int \mathcal{L} dt} \sum_i \frac{1}{\epsilon_i} = \frac{1}{\Delta p_T^\mu \int \mathcal{L} dt} \sum_i \frac{1}{\epsilon^\mu(p_{Ti}^\mu) \epsilon^{\text{jet}}(E_{Ti}^{\text{high}})} \quad (9.2)$$

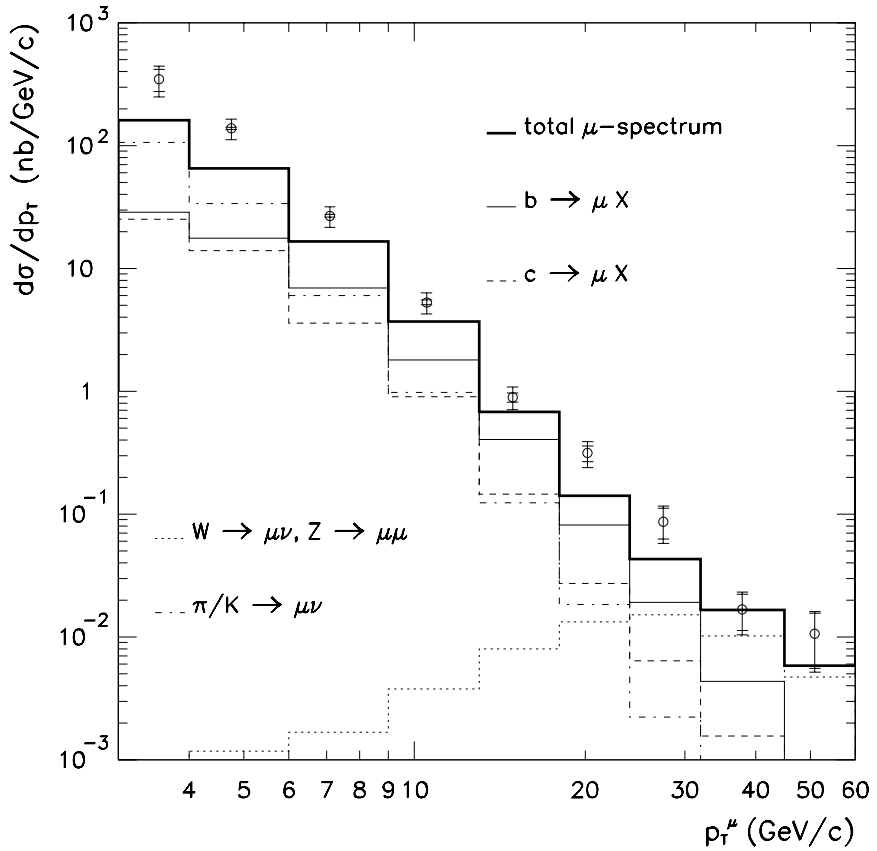


Figure 9.1: Differential muon spectrum $d\sigma^\mu/dp_T^\mu$ for muon-jet events with $|\eta^\mu| < 0.8$, and $E_T > 15$ GeV for the highest E_T jet in the event. The experimental data points are compared to a Monte Carlo prediction, (section 6.2) with the experimental momentum resolution (appendix A) applied to the generated muon momentum.

p_T^μ interval (GeV/c)	observed number of muons	$d\sigma/dp_T^\mu$ (nb/(GeV/c))	statistical error (%)
3-4	1038	350	20
4-6	3817	140	2
6-9	1856	27	3
9-13	609	5.3	5
13-18	154	0.89	9
18-24	63	0.31	15
24-32	25	0.087	25
32-45	10	0.017	33
45-60	5	0.012	48
> 60	1		

Table 9.1: The differential muon spectrum for muon-jet events, showing the p_T^μ intervals, the number of observed muons in each of the intervals, the differential muon cross section and its statistical error. The muon differential cross section and its statistical error are calculated with formulas 9.2 and 9.3, respectively. calculated with form

where the index i applies to all the muons in the i -th data bin, and Δp_T^μ denotes the width of the p_T^μ intervals. The corresponding statistical error is

$$\frac{1}{\Delta p_T^\mu \int \mathcal{L} dt} \sqrt{\sum_i \left(\frac{1}{\epsilon_i} \right)^2} \quad (9.3)$$

Figure 9.1 shows the differential spectrum for muon-jet events with $|\eta^\mu| < 0.8$ and $E_T^{\text{high}} > 15 \text{ GeV}$ as a function of p_T^μ . The results are also listed in table 9.1. The systematic error of 19% comes from the sum in quadrature of the 13%

systematic error in the muon and jet efficiencies each, and 5% systematic uncertainty on the integrated luminosity [21]. The inner error bars on the data points correspond to the statistical errors and the outer bars correspond to the total errors (sum in quadrature of statistical and systematic errors).

The data are compared to ISAJET Monte Carlo predicted cross sections for b -quark production and the other main processes contributing to the spectrum (chapter 6). As the data has not yet been corrected for effects of the muon momentum resolution, we apply the measured muon momentum resolution of $\Delta(1/p) = ((0.18/p)^2 + 0.008^2)^{1/2}$ (chapter 3.5 and appendix A) to the muon momentum from ISAJET. Below $p_T^\mu = 6 \text{ GeV}/c$) the spectrum is dominated by in-flight decays of pions and kaons, while decays of W and Z bosons dominate at high $p_T^\mu (> 25 \text{ GeV}/c)$. We observe reasonably good agreement in shape between the data and the predictions, but the data significantly exceeds the combined theory prediction. We should, however, keep in mind that the Monte Carlo predictions are subject to significant systematic errors. In section 2.2 we noted that the b -production prediction has an uncertainty of more than 60% from uncertainties in the Standard Model parameters alone. In section 6.5 we estimate an uncertainty of 21% on the rate of the in-flight decay muons, while the muon spectrum from W and Z -decays carries an uncertainty of 15% (section 6.5). We observe that the muons from b decays are overwhelmed by in-flight decays of pions and kaons in the region $p_T^\mu < 6 \text{ GeV}/c$, and that in that region the data is not well described by the Monte Carlo predictions. We hence institute an addition cut rejecting muons of $p_T < 6 \text{ GeV}/c$.

Because of the above mentioned uncertainties in cross-section predictions, we will rely on the topology of the muon-jet events such as the transverse momentum of the muon relative to the jet, rather than relying on Monte Carlo cross section predictions whenever possible.

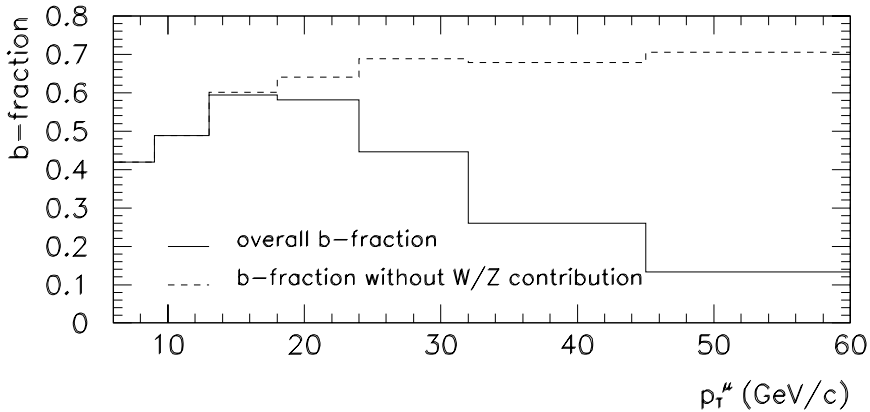


Figure 9.2: Prediction of the fraction of muons from b -quark production from Monte Carlo.

9.3 Isolation of the $b\bar{b}$ -Component of the Muon p_T -Spectrum

In the previous section we extracted the p_T -spectrum ($d\sigma/dp_T$) for muons in the muon-jet data. Now we study the fraction of the data which comes from b (or \bar{b})-quark production.

The principal processes contributing to the muon spectrum are b and c -quark production, the decays of W and Z -bosons and in-flight decays of charged pions and kaons. Contributions from J/Ψ , Drell Yan and Upsilon production are negligible.

In chapter 7 we showed that the contribution of non-beam produced muons to the final data sample is very small. Visual scanning of a subsample

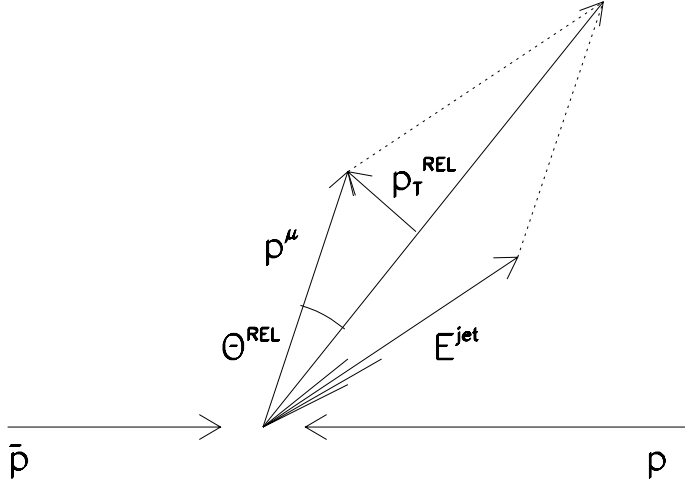


Figure 9.3: Definition of p_T^{REL} .

of 109 events produced two events which were consistent with cosmic ray background. Based on this limited study we assign an upper limit of 2% cosmic ray muons in the data sample.

Figure 9.1 shows a comparison of the data and calculations of the individual contributions to the muon spectrum as a function of the muon p_T .

The Monte Carlo estimates of the fraction of the muon cross section due to b -quark decays, $b / (b+c+\pi/K+W/Z)$ and $b / (b+c+\pi/K)$ are shown in fig. 9.2. The overall b -fraction shows the clear dominance of vector boson decays at high transverse momenta, whereas in the absence of W/Z -decays the b -fraction plateaus at $p_T^\mu \geq 20 \text{ GeV}/c$. While the rates for b and c -production are similar the dominance of the b over the c -quark component is due to fragmentation and smaller Q -value in c -quark decay so that c -quarks give muons of lower p_T .

than b -quarks of the same transverse momentum. As noted in chapter 6 the prediction for b -quark production can vary by up to $\pm 60\%$ depending on the choice of the parameters Λ and μ_0 . In addition the light mass of the c -quark makes calculations of its production rate uncertain.

We can, however, extract the b -fraction from the data directly, if we consider the subsample of $\approx 85\%$ of the data where a jet of $E_T > 8 \text{ GeV}$ is reconstructed within $\Delta R = 1.0$ of the muon. (Since we are not concerned with jet efficiency for this study, we can use jets of low transverse momenta.) B -meson decays, because of the high mass of the b quarks have a higher Q -value ($\approx 3 \text{ GeV}$) than D -meson decays ($Q \approx 1 \text{ GeV}$). Due to the higher Q -value, B mesons can impart a higher transverse momentum “kick” to the muon than decaying D mesons.

We use the quantity $p_T^{\text{REL}} = p^\mu \sin \Theta^{\text{REL}}$ to separate, on a statistical basis, b -quarks from c -quarks and in-flight π/K decays. Θ^{REL} is the angle between the momentum vector of the muon and the vector sum of the muon and jet momenta. Neglecting the neutrino momentum, the vector sum of the muon and jet momenta is an approximation of the momentum vector of the parent particle. p_T^{REL} is defined as the component of the muon momentum perpendicular to the muon-jet axis (Fig. 9.3).

The p_T^{REL} -distributions from Monte Carlo (chapter 6) for b , c and π/K decays are shown in fig. 9.4. All curves are normalized to the same area. The higher Q -value of b -decays result in a result in a p_T^{REL} -distribution shifted towards higher values of p_T^{REL} . Since p_T^{REL} is the projection of the muon momentum perpendicular to the muon-jet axis, it is independent of the momentum of

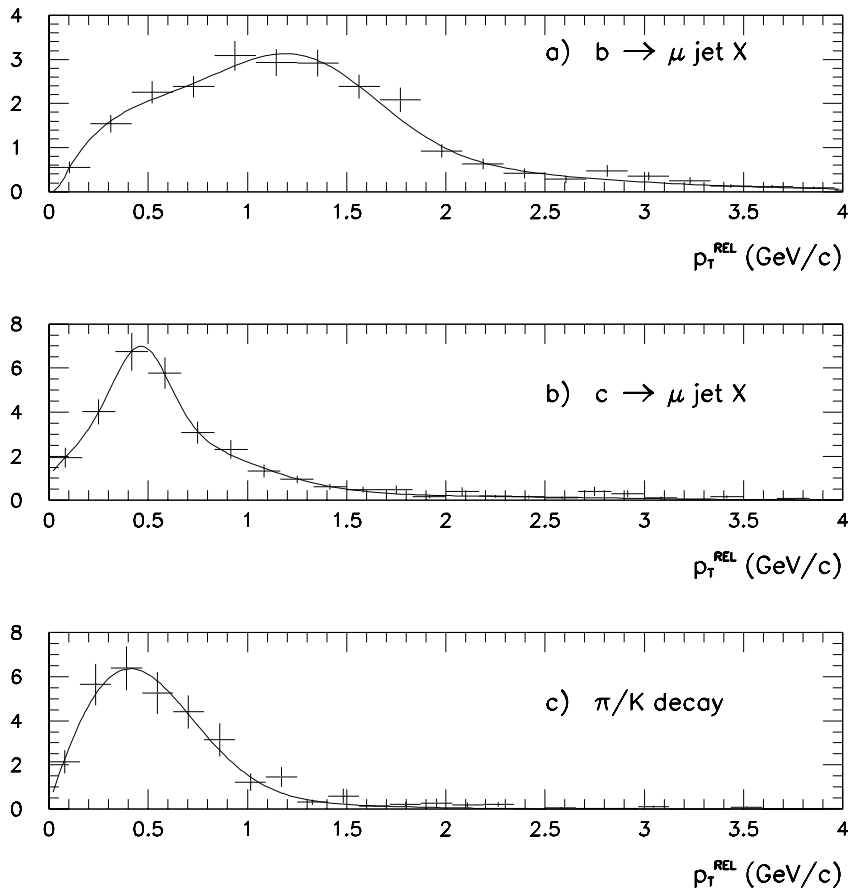


Figure 9.4: Monte Carlo p_T^{REL} -distributions for b and c -quark decays, and for in-flight decays of pions and kaons. The plots show the Monte Carlo with statistical errors (points) and the parameterization used in the fit (smooth line).

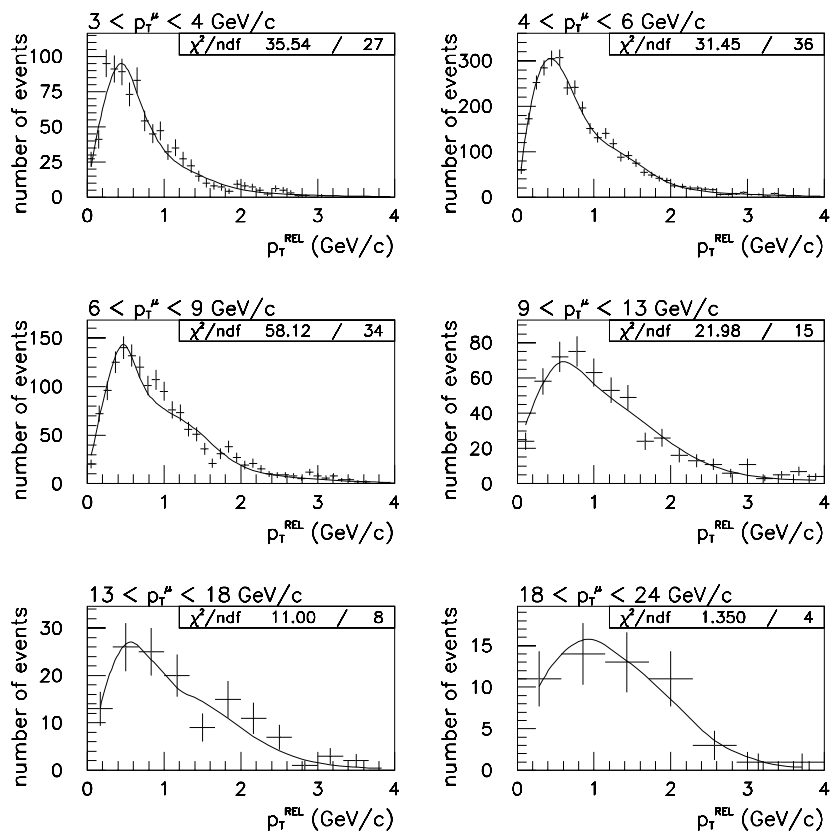


Figure 9.5: Experimental p_T^{REL} distributions for $3 < p_T^\mu < 24 \text{ GeV}/c$. The smooth curves are fits to the summed Monte Carlo p_T^{REL} distributions for b -, c -quark and π/K decay events.

	$4 < p_T^\mu < 9 \text{ GeV/c}$	$p_T^\mu > 9 \text{ GeV/c}$
$b/\bar{b} \rightarrow \mu X$	1.3 / 0.48	1.4 / 0.97
$c/\bar{c} \rightarrow \mu X$	0.77 / 0.69	0.88 / 0.83
$\pi/K \rightarrow \mu\nu$	0.64 / 0.52	1.1 / 0.98

Table 9.2: Mean/RMS deviation from the mean for p_T^{REL} distributions from Monte Carlo.

the decaying object, and a function of only its mass. However, detector effects such as muon momentum resolution have an effect on the p_T^{REL} distributions, causing a broadening of the distribution with increasing muon p_T . Table 9.2 shows the Monte Carlo calculated mean and RMS deviation from the mean for $4 < p_T^\mu < 9 \text{ GeV/c}$ and for $p_T^\mu > 9 \text{ GeV/c}$.

The b -fraction of the data was estimated by fitting the experimental distributions of p_T^{REL} with the Monte Carlo distributions for b , c and π/K -decays, the b and c fractions are taken as fit parameters. The fits are restricted to $p_T^\mu < 24 \text{ GeV/c}$, for which the W/Z component can be ignored. Since the b fraction is expected to vary with muon momentum (fig. 9.2), separate fits were done for each p_T^μ interval below $p_T^\mu = 24 \text{ GeV/c}$ in figure 9.1.

Fig. 9.5 shows the results for the p_T^{REL} fits to data for $p_T^\mu < 24 \text{ GeV/c}$. The fraction of muons from b -decays are equal for the intervals $13 < p_T^\mu < 18 \text{ GeV/c}$ and $18 < p_T^\mu < 24 \text{ GeV/c}$. To reduce the statistical errors, those two bins were merged, giving a b -fraction of 0.82 ± 0.15 . Monte Carlo studies indicate that the ratio $b/(b + c + \pi/K)$, in the absence of W/Z -background, the b -fraction, the b -fraction is approximately constant (within $\approx 10\%$) above $p_T^\mu = 15 \text{ GeV/c}$

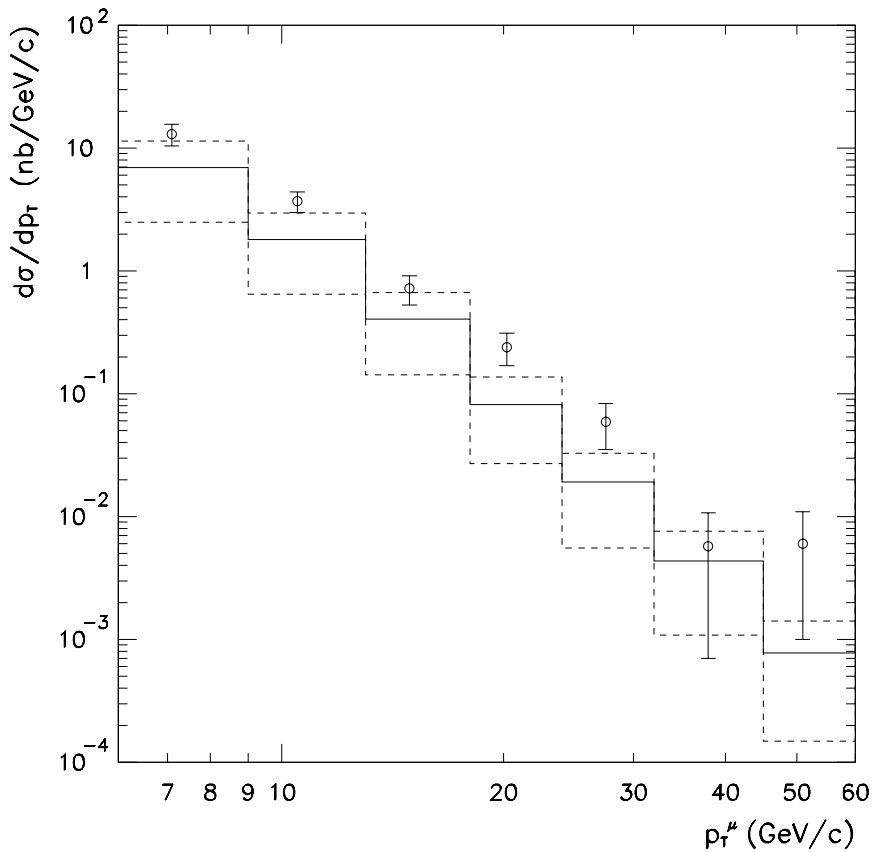


Figure 9.6: Muon spectrum for events with $|\eta^\mu| < 0.8$ and $E_T^{\text{high}} > 15 \text{ GeV}$ with $c, \pi/K$ and W/Z components subtracted, compared to a Monte Carlo calculation of $b \rightarrow \mu X$ processes (solid histogram). The dashed histogram indicates the uncertainty in the Monte Carlo prediction.

p_T^μ range (GeV/c)	fraction of W/Z -decays	f_b $b/(b + c + \pi/K)$	$d\sigma/dp_T^\mu(b/\bar{b} \rightarrow \mu X)$ (nb/(GeV/c))
3-4	0	0.24 ± 0.04	84 ± 30
4-6	0	0.41 ± 0.02	57 ± 10
6-9	0	0.50 ± 0.03	13 ± 3
9-13	0	0.69 ± 0.07	3.7 ± 0.8
13-18	0.009 ± 0.002	0.82 ± 0.15	0.72 ± 0.2
18-24	0.04 ± 0.01	"	0.24 ± 0.07
24-32	0.17 ± 0.06	"	$(5 \pm 2) \cdot 10^{-2}$
32-45	0.69 ± 0.23	"	$(5 \pm 5) \cdot 10^{-3}$
45-60	0.39 ± 0.21	"	$(6 \pm 5) \cdot 10^{-3}$

Table 9.3: Calculation of $d\sigma/dp_T^\mu(b/\bar{b} \rightarrow \mu + \text{jet} + X)$. Shown for each p_T^μ bin are the fraction of muons in the data sample due to W/Z -decays, as well as $f_b = b/(b + c + \pi/K)$ from the p_T^{REL} fits and the muon spectrum associated with $b/\bar{b} \rightarrow \mu X$ decays.

(fig. 9.2); we assumed a value for that ratio of 0.82 ± 0.15 above $p_T^\mu = 24$ GeV/c.

The muon spectrum due to b -quarks is then obtained by subtracting the W/Z component of the spectrum and then applying the $b/(b + c + \pi/K)$ ratio obtained from the p_T^{REL} fits:

$$\frac{d\sigma}{dp_T} = f_b \left[\frac{1}{\epsilon \int \mathcal{L} dt} \frac{dN}{dp_T^\mu} - \frac{d\sigma}{dp_T^\mu}(W \rightarrow \mu\nu, Z \rightarrow \mu\mu) \right] \quad (9.4)$$

where $(\epsilon \int \mathcal{L} dt)^{-1} dN/dp_T^\mu$ is the measured muon spectrum (table 9.1), and $d\sigma/dp_T^\mu(W \rightarrow \mu\nu, Z \rightarrow \mu\mu)$ is the contribution of W/Z decays (section 6.5). f_b denotes the ratio $b/(b + c + \pi/K)$. The results of this background subtraction are tabulated in table 9.3. Figure 9.6 shows the measured muon spectrum for $b \rightarrow \mu + \text{jets} + X$, together with the corresponding prediction; the dotted

	source of uncertainty	estimated error (%)
1	QCD parameters Λ and μ_0	60
2	structure functions	20
3	mass of the b -quark	5
4	branching ratio $b \rightarrow \mu X$	5
5	fragmentation function	14
6	muon momentum resolution	3 to 50

Table 9.4: Uncertainty in theory prediction of $d\sigma/dp_T^\mu(b\bar{b}/\rightarrow \mu X)$

lines indicate an estimate of the uncertainty in the prediction. Table 9.4 list the contributions to the latter (See section 2.2 for a discussion of items 1-3). The uncertainty on the branching ratio $BR(b \rightarrow \mu X)$ is obtained from recent LEP results ($BR(B \rightarrow \mu X) = 0.110 \pm 0.005$) [37]. The effect of the fragmentation uncertainty has been estimated by varying the Peterson parameter ϵ (section 6.2) by 50% [73]. The effect of the momentum resolution uncertainties has been estimated by varying the momentum resolution (section 3.5) within errors and reapplying it to the Monte Carlo. This causes a change in the muon spectrum which varies between 3% at 3 GeV/c to 50% at 60 GeV/c.

The overall uncertainty in the in the Monte Carlo prediction for $d\sigma/dp_T^\mu(b/\bar{b} \rightarrow \mu + \text{jets} + X)$ was taken as the sum in quadrature of the individual contributions in table 9.4, and varies between 65% at low p_T^μ and 82% at high p_T^μ values.

9.4 Summary

In this chapter we have presented a determination of the muon spectrum from $b\bar{b} \rightarrow \mu + \text{jets} + X$ decays, for events with $|\eta^\mu| < 0.8$ and a jet of $E_T > 15 \text{ GeV}$. The results agree well in shape with Monte Carlo prediction, but are a factor of two to three higher in magnitude. In the next chapter we will extract the corresponding b -quark production cross section as a function of the transverse momentum of the b -quark.

Chapter 10

The b -Quark p_T -Spectrum

10.1 Overview

In the previous chapter we determined the differential cross-section $d\sigma/dp_T^\mu(b/\bar{b} \rightarrow \mu X)$ for muons from b and \bar{b} decays in which $|\eta^\mu| < 0.8$ and $E_T^{\text{high}} > 15 \text{ GeV}$. In this chapter we convert this into a cross-section as a function of the p_T of the parent $b(\bar{b})$ quarks.

We proceed in two steps. First the data are corrected for the effects of the muon momentum resolution (section 3.5 and appendix A), translating the measured differential p_T spectrum (fig. 9.6) into the true muon momentum spectrum. Next we use a Monte Carlo based technique to convert this differential cross section into a cross section as a function of the p_T of the $b(\bar{b})$ -quarks.

10.2 Unfolding the Muon Momentum Resolution

Figure 10.1 illustrates the effect of the muon momentum resolution on the p_T^μ -spectrum. Resolution effects flatten the spectrum, and have the largest impact at high p_T^μ . To unfold this effect, we use a Monte Carlo method based on Bayes' theorem, which is described in appendix C.

The method is iterative and starts with an initial guess for the true momentum spectrum, for which we use the ISAJET $b \rightarrow \mu X$ cross section (chapter 6). The iterations are terminated if the χ^2 between the unsmeared cross sections between two consecutive iterations is less than 0.01. This is achieved after 5 iterations. The resulting unsmeared cross section is listed in table 10.1 and shown in fig. 10.2

The uncertainties in the cross section due to our understanding of the muon momentum resolution has been estimated by varying the resolution function $\Delta p = \sqrt{(A/p)^2 + B^2}$, within its range of uncertainty. Values of $A = 0.16$, 0.18 and 0.20 , and $B = 0.006$, 0.008 , and 0.001 , respectively, have been used on a set of $b \rightarrow \mu + X$ Monte Carlo events. Three values of $P(E_j|C_i)$ were obtained and used to unsmeared the experimental spectrum. The deviations of the two extreme values of the resolution from the central value ($A = 0.18$, $B = 0.008$) are used as an estimate of the uncertainty in the unsmeared spectrum. These are listed in table 10.1.

The ISAJET $b \rightarrow \mu + X$ Monte Carlo differential cross section was used as

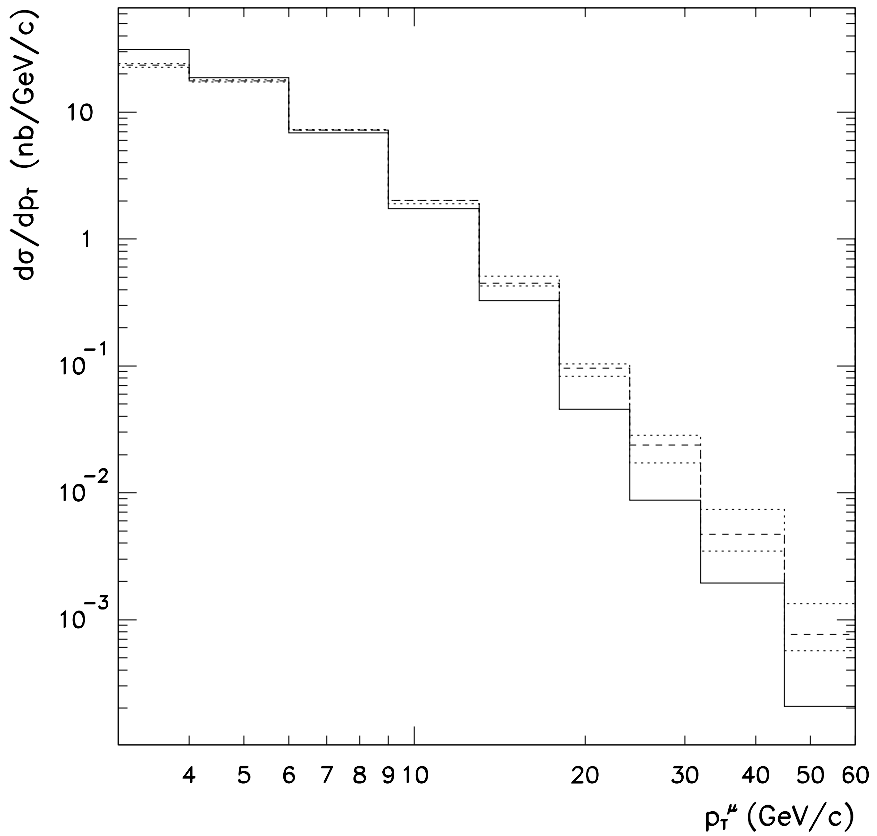


Figure 10.1: The effect of the muon momentum resolution on the measured muon p_T spectrum. The solid line shows the true momentum spectrum from b and \bar{b} production and the dashed line shows the spectrum after muon momentum resolution has been applied. The dotted lines indicate the uncertainty on the resolution function.

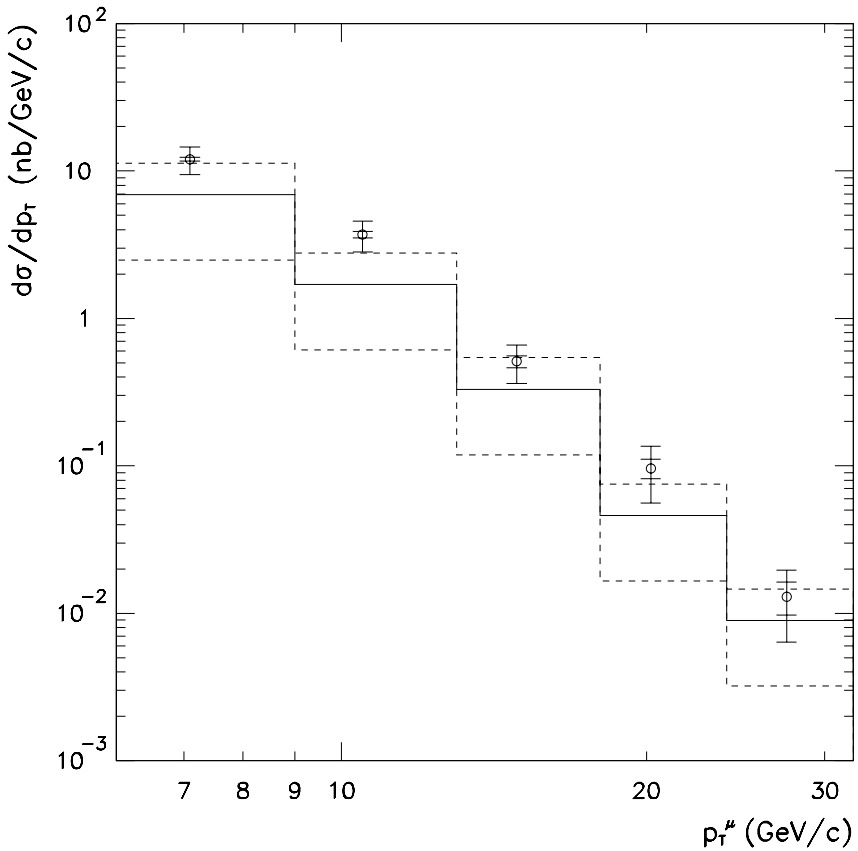


Figure 10.2: Comparison of the muon transverse momentum spectrum $d\sigma/dp_T^\mu$ after correction for muon momentum resolution effects, and the ISAJET prediction (histogram) for $b/\bar{b} \rightarrow \mu X$ production. The inner error bars are the statistical error, and the outer error bars show the sum in quadrature of statistical and systematic errors.

p_T^μ (GeV/c)	unsmearing factor f_u			$d\sigma/dp_T^\mu$	
	f_u	resolution	sys. uncertainty (%)	(nb/GeV/c)	tot. uncertainty (%)
3- 4	1.24	3	0	104	32
4- 6	0.85	3	0	49	19
6- 9	0.92	10	0	12	21
9-12	1.00	10	6	3.7	24
12-18	0.70	10	6	0.51	29
18-24	0.40	20	20	$9.6 \cdot 10^{-2}$	42
24-32	0.26	20	20	$1.3 \cdot 10^{-2}$	51
32-45	0.17	30	50	$8.5 \cdot 10^{-4}$	112
45-60	0.14	100	140	$8.4 \cdot 10^{-2}$	192

Table 10.1: The unsmearing factor $f_u = (d\sigma/dp_T^\mu)^{\text{true}} / (d\sigma/dp_T^\mu)^{\text{reco}}$ and its uncertainties, and the unsmearred muon differential cross section.

the initial guess in the unsmearing procedure. To estimate the dependence of the unsmearred cross section on the initial conditions, we unsmear the Monte Carlo spectrum using the unsmearred data spectrum as the initial guess. The difference between the result of this unsmearing process and the generated spectrum is taken as the uncertainty in the corrected spectrum due to the initial conditions. It is listed in table 10.1. The total uncertainty in the corrected spectrum is the sum in quadrature of the errors of the spectrum before unsmearing (table 9.3) and the uncertainties incurred in the unsmearing process (table 10.1).

The errors in the last two bins ($p_T^\mu > 32 \text{ GeV/c}$) are greater than 100% due to both the large uncertainty in the subtraction of the W/Z background

and due to the large uncertainty in the resolution function in the same region. We hence exclude that region, and are left with 2707 events within ($6 < p_T^\mu < 32 \text{ GeV}/c$).

The results are shown in fig. 10.2. This serves as the basis for the last step of the analysis, the extraction of the transverse momentum spectrum of the parent b -quarks.

10.3 Extraction of the b -Quark p_T -Spectrum

To extract the b -quark production cross section we have to retrace the hadronization and decay process undergone by the b -quarks in their decay (section 6.2). The b -quarks hadronize into B -hadrons which decay weakly with a lifetime of approx 10^{-12} s .

The extraction follows the Monte Carlo method developed by UA1 [76], and subsequently used by CDF [58] and DØ [77, 87]. The method is illustrated by figure 10.3 which shows the calculated integral p_T -spectrum for

1. b quarks with rapidity $|y| < 1$ and $p_T^b > p_T^{\min}$ (open histogram) and
2. for b quarks that decay into muons within a given transverse momentum range $x_1 - x_2$, and which have and which have $|\eta| < 0.8$, and where the event contains at least one jet of $E_T > 15 \text{ GeV}$, as selected in the data. (shaded histogram).

Each bin $x_1 - x_2$ in the differential muon p_T spectrum is transformed in a point

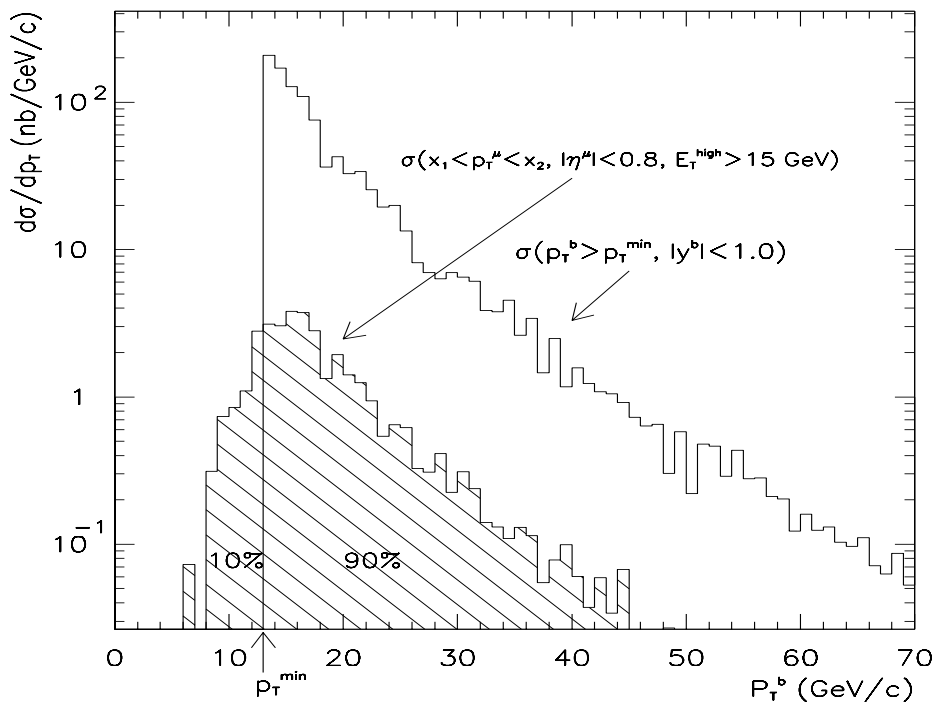


Figure 10.3: Illustration of the method used to convert the muon spectrum into the b -quark production cross section. The conversion factor $f^{\mu \rightarrow b}$ is obtained by dividing the area of the outer (empty) histogram by the area of the shaded histogram.

$\sigma(p_T > p_T^{\min})$ in the b -quark integral spectrum using the formula

$$\sigma(p_T^b > p_T^{\min}, |y^b| < 1) = \sigma^{\text{data}}(x_1 < p_T^\mu < x_2, |\eta^\mu| < 0.8, E_T^{\text{high}} > 15 \text{ GeV}) \cdot f^{\mu \rightarrow b} \quad (10.1)$$

where

$$f^{\mu \rightarrow b} = \frac{\sigma^{MC}(p_T^b > p_T^{\min}, |y^b| < 1)}{\sigma^{MC}(x_1 < p_T^\mu < x_2, |\eta^\mu| < 0.8, E_T^{\text{high}} > 15 \text{ GeV})} \quad (10.2)$$

is the ratio of the areas of the two histograms in fig. 10.3. The choice of p_T^{\min} is not crucial since different values of p_T^{\min} result in different values of $f^{\mu \rightarrow b}$, but the resulting integral b -cross section values all describe the same b -quark transverse momentum spectrum. The values of p_T^{\min} , $f^{\mu \rightarrow b}$ used here, and the calculated b -quark production cross section are listed in table 10.2. The b -quark cross section is also plotted in fig. 10.4. We note that while the denominator in equation 10.2 refers to muons of both signs, we follow the convention of previous analyses and quote the a cross section only for b quarks. The numerator in equation 10.2 hence excludes \bar{b} quarks.

We consider systematic errors in the extraction of the b -quark cross section associated with the choice of fragmentation function, structure functions, the branching ratio $BR(b \rightarrow \mu X)$, and the mass of the b -quark. In order to estimate the effect of the uncertainty in fragmentation function we vary the Peterson parameter (section 6.2) by 50% and recalculate $f^{\mu \rightarrow b}$. This changes the conversion factor by $\approx 14\%$. Changing the structure function from MRSD0 to DFLM has only a minor effect on $f^{\mu \rightarrow b}$, about 1%, since structure functions occur in both the numerator and denominator of $f^{\mu \rightarrow b}$ in equation 10.2.

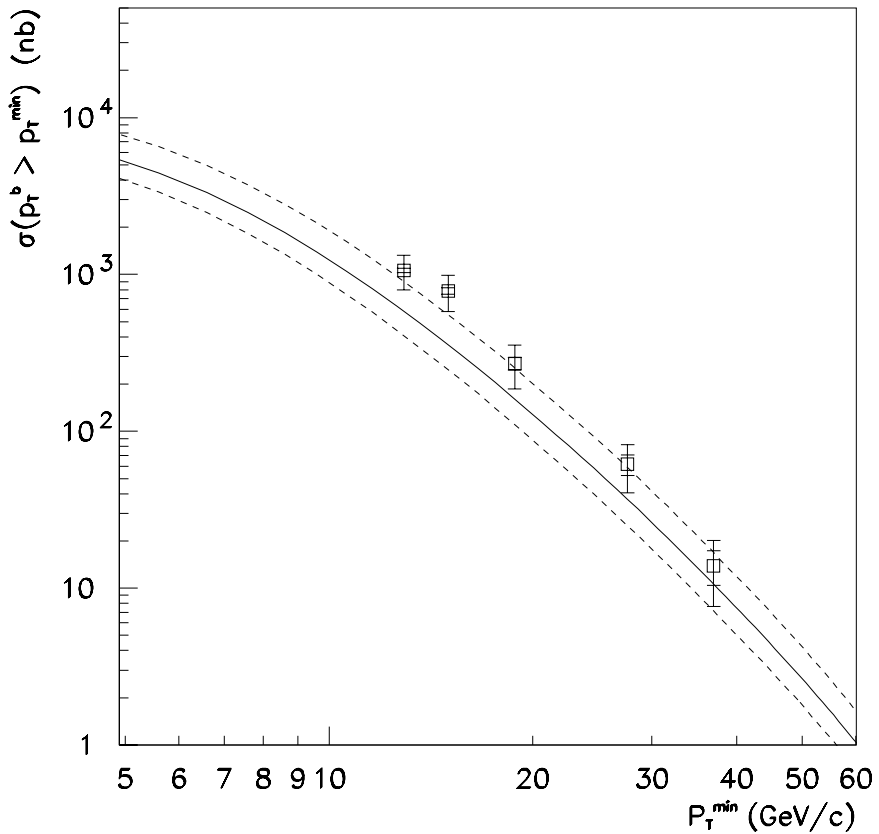


Figure 10.4: b -quark production integral cross section as a function of p_T^{\min} , for $|y^b| < 1$, compared to the NDE prediction. The inner error bars on the data show the statistical error, the outer ones indicate the sum in quadrature of statistical and systematic errors. The solid line shows the central QCD prediction, and the dashed lines show the uncertainty arising from varying Λ and μ_0 .

p_T^μ GeV/c	p_T^{\min} GeV/c	$f^{\mu \rightarrow b}$	(nb)	$\sigma(p_T^b > p_T^{\min})$	
				stat error (%)	sys. error (%)
6-9	12.9	29.5	1060	3	25
9-13	15.0	51.9	770	5	26
13-18	18.8	106	270	9	30
18-24	28	107	62	15	31
23-32	37	135	13.9	25	37

Table 10.2: Conversion of the differential muon cross section into the b -quark production cross section

An error of 5% each was assigned to the branching ratio and to the mass of the b -quark (section 2.2). While an error in the branching ratio only affects the denominator in equation 10.2, the error in m_b affects both numerator and denominator and the 5% error we use here is hence likely to be an overestimate for the error in $f^{\mu \rightarrow b}$. The additional uncertainty incurred in the conversion of the muon to the b -quark spectrum is hence 16%, the sum in quadrature of the errors from m_b (5%), the branching fraction $b \rightarrow \mu$ (5%), the structure function parameterization (1%) and choice of the fragmentation function (14%). We add this in quadrature to the errors in the unsmeared muon spectrum in table 10.1, the result is shown in table 10.2 and figure 10.4.

The experimental data are compared to the theory prediction by NDE described in section 2.2. The central theory prediction was obtained with the MRSD0 structure function with $\mu = \mu_0$ and $\Lambda = 140$ MeV. The bands describing the theoretical uncertainties were obtained by varying Λ and μ to

187 MeV and $\mu_0/2$ (upper line) versus 100 MeV and $2\mu_0$ (lower line). They were obtained by integrating the theory predictions shown in figure 2.2 from p_T^{\min} to infinity.

10.4 Summary

Figure 10.4 and table 10.2 represent the final results of this analysis, the b -quark production cross section as a function of the transverse momentum of the b -quark, for b quarks produced within $|y^b| < 1$. The data are consistently above the theory prediction and line up fairly well with the upper edge of the theoretical uncertainty. In the final chapter of this thesis we will discuss this result and its relationship to other measurements of b -quark production in hadron-hadron collisions. The implications of this investigation for future studies of b -quark production at hadro-hadron colliders will also be addressed.

Chapter 11

Conclusions

11.1 Introduction

In this chapter we survey the present results on b -quark production in $p\bar{p}$ -collider experiments at $0.6 < \sqrt{s} < 1.8$ TeV. The results reported here, as well as those of CDF and UA1, are systematically in excess of QCD predictions.

Finally we consider the prospects for enhanced measurements of b -quark cross sections in future runs of the DØ detector at the Tevatron.

11.2 Current Status of b -Quark Production Cross Sections

The measurement of bottom quark production in $p\bar{p}$ -collisions provides an important test of the theory of QCD. Due to the high mass of the b -quark (≈ 5 GeV/c 2), QCD calculations of b -quark production can be performed as perturbative expansions in α_s . The bottom quark production cross section

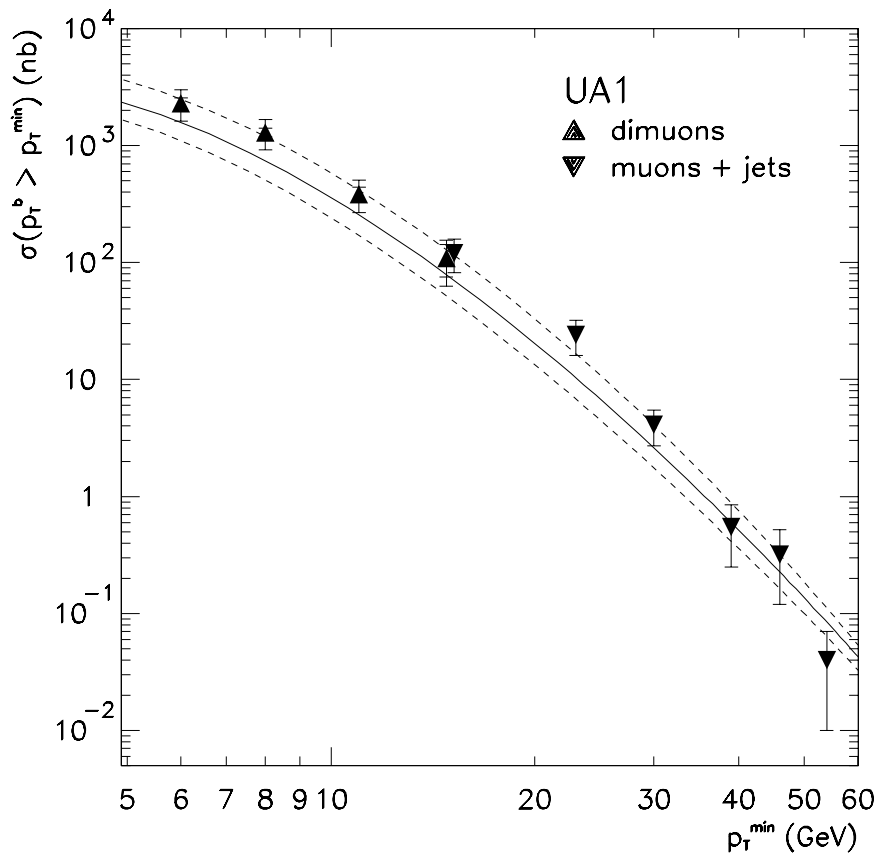


Figure 11.1: Integral b -quark cross sections from dimuon and muon-jet events from the UA1 experiment at CERN, in $p\bar{p}$ collisions at $\sqrt{s} = 0.63$ TeV, for $|y^b| < 1.5$. The central theory prediction (solid line) and uncertainties (dashed lines) are described in the text.

has been calculated to $\mathcal{O}(\alpha_s^3)$ by Nason, Dawson and Ellis (NDE) [14] and Beenakker *et al.* [15].

The b -quark production cross section in $p\bar{p}$ -collisions was first measured by UA1 at CERN at $\sqrt{s} = 0.63$ TeV. Figure 11.1 shows the b -quark cross section measured from UA1 dimuon [78] and muon-jet [4] data samples for the rapidity $|y^b| < 1.5$.

The solid curve in fig. 11.1 is the central QCD prediction using $\Lambda = 140$ MeV, $\mu = \mu_0$ and the MRSD0 [17] structure functions. The uncertainty in the theory prediction is represented by the dashed curves and was obtained by varying Λ and μ from 187 MeV and $\mu_0/2$ (upper limit) to 100 MeV and $2\mu_0$ (lower limit). The experimental data points agree well in shape with the theory prediction but are higher in normalization and lie close to the upper edge of the uncertainty in the QCD prediction.

Figure 11.2 shows similar measurements from the CDF detector [79], again compared to QCD predictions with the same parameters as in fig. 11.1, but for a rapidity coverage of $|y^b| < 1$ and the Tevatron center of mass energy of 1.8 TeV. (The measurements are from inclusive muon [5], inclusive electron [80] and inclusive J/Ψ [81] data samples as well as from radiative χ decay data [82]. Finally, measurements of b -quark production from the exclusive decays $B^\pm \rightarrow J/\Psi K^\pm$ and $B^\circ \rightarrow J/\Psi K^{*\circ}$ are shown [83, 84].) These results are in poor agreement with the central theory prediction. Especially the analyses involving J/Ψ final states give b -quark cross sections higher than theory predictions by a factor of three or more at $p_T^b < 12$ GeV/c.

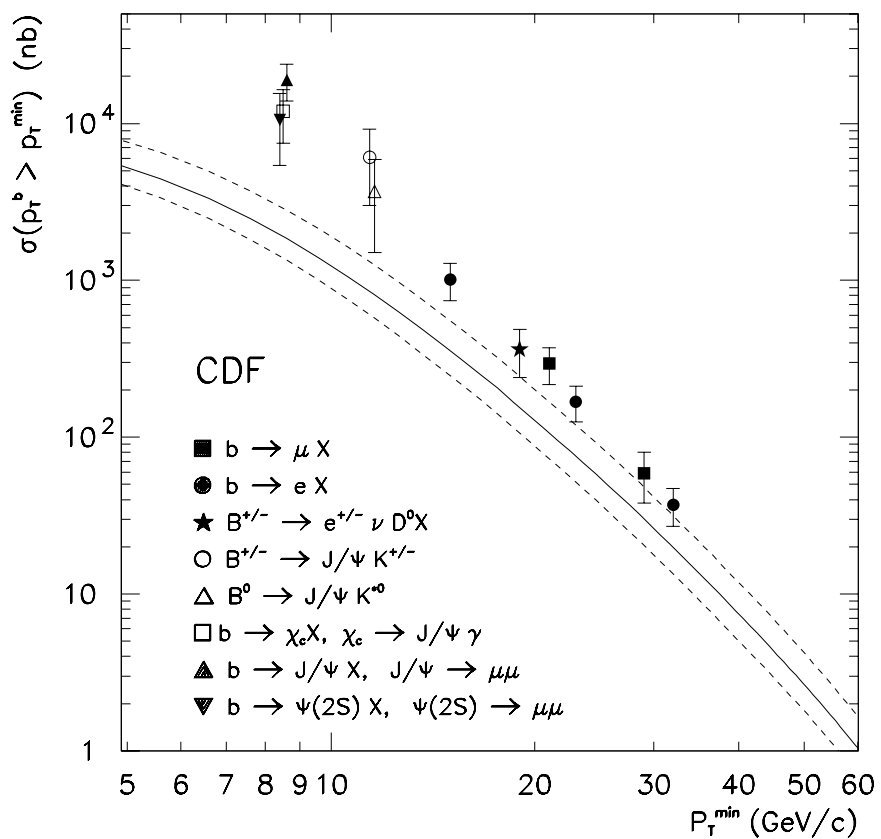


Figure 11.2: Integral b -quark production cross sections for $|y^b| < 1$ from the CDF experiment in $p\bar{p}$ collisions at $\sqrt{s} = 1.8 \text{ TeV}$.

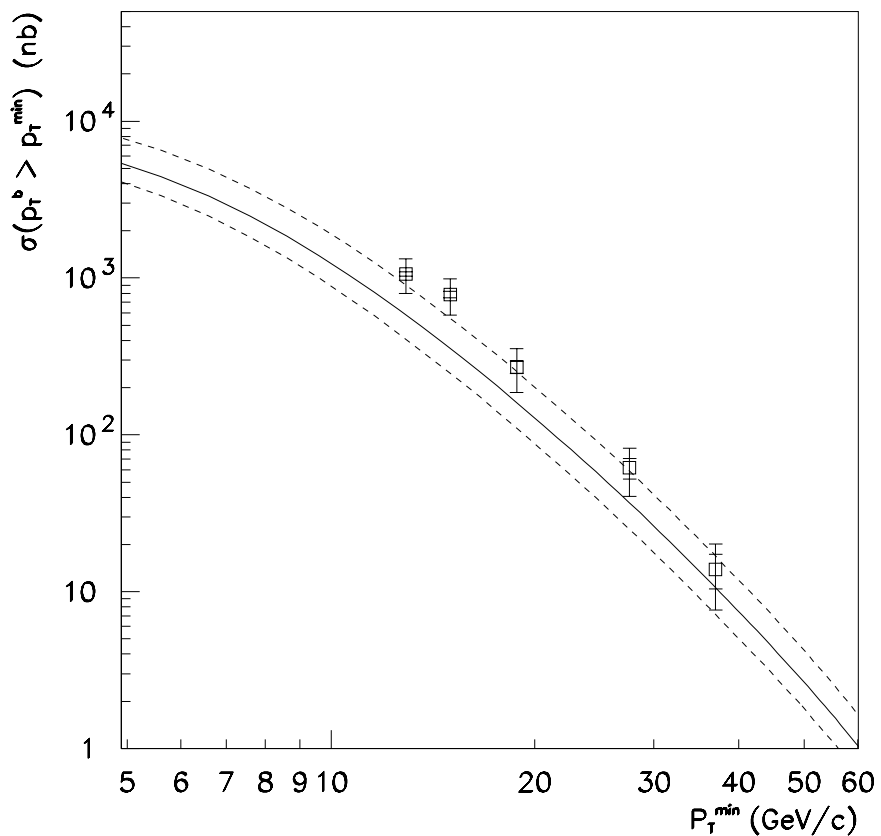


Figure 11.3: b -quark production integral cross section from this analysis, compared to the NLO QCD theory prediction.

p_T^μ (GeV/c)	observed number of muons	$d\sigma/dp_T^\mu(b\bar{b} \rightarrow \mu + \text{jet} + X)$ $ \eta^\mu < 0.8$				p_T^{\min} (GeV/c)	$\sigma(p_T^b > p_T^{\min})$ $ y^b < 1.0$		
		[nb/(GeV/c)]	% uncertainty	stat.	sys.		(nb)	% uncertainty	stat.
6- 9	1856	13	3	19		12.9	1060	3	25
9-12	609	3.7	5	20		15.0	770	5	26
12-18	154	0.72	9	25		18.8	270	9	30
18-24	63	0.24	15	27		28.0	62	15	31
24-32	25	$5 \cdot 10^{-2}$	25	33		37.0	13.9	25	37

Table 11.1: The $b \rightarrow \mu + \text{jet} + X$ and b quark cross section after correction for resolution and background effects

The results of this analysis for the $b \rightarrow \mu + \text{jet} + X$ and the b -quark production cross section for $|y^b| < 1$ are listed in table 11.1. The corresponding integral b -quark cross section is shown in fig. 11.3. The data agree in shape with the theory prediction but are higher in normalization, and are close to the upper edge of the theoretical uncertainty.

We see from table 11.1 that the error in this measurement is predominantly systematic and comes from a variety of sources, with muon and jet efficiencies responsible the largest contribution (18%) at low p_T^b . The error at higher p_T^b is dominated by uncertainties in the muon momentum resolution and the subtraction of backgrounds from W/Z -boson decays.

Figure 11.4 compares the results of this analysis with other DØ measurements based on inclusive muon [85] dimuon [86], and J/Ψ events [87]. The results are in excellent agreement with each other. The large excess of data

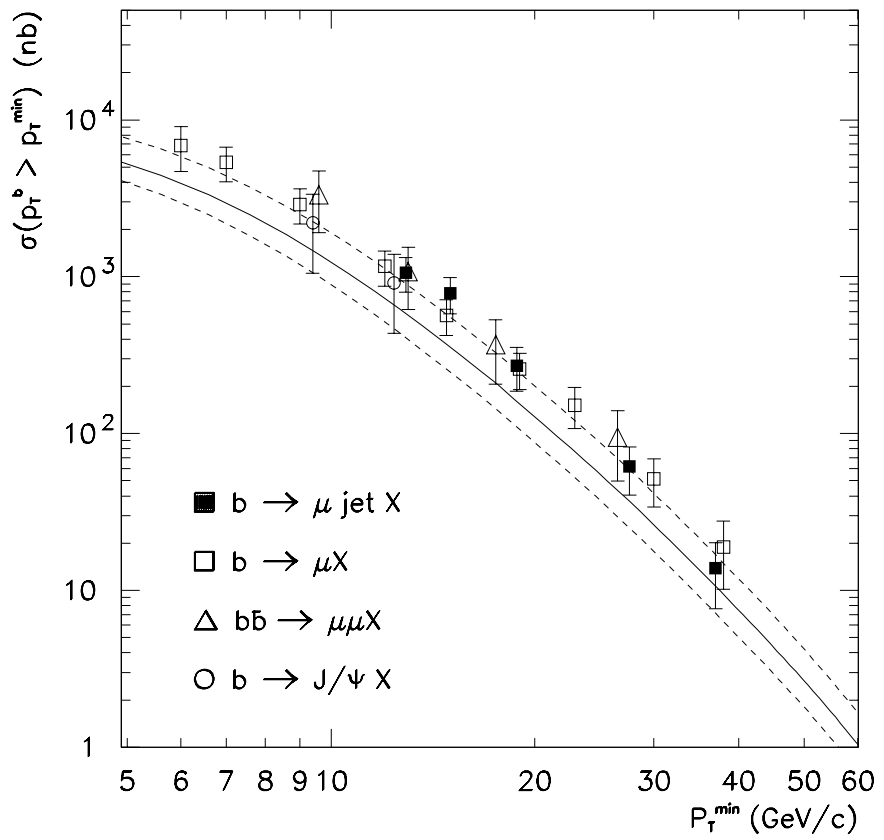


Figure 11.4: b -quark production integral cross section from this analysis, compared to DØ measurements based on inclusive muon, inclusive dimuon, and J/Ψ data.

DØ data at $\sqrt{s} = 1.8 \text{ TeV}$						
muon-jet		inclusive muons		inclusive dimuons		
p_T^{\min}	data/theory	p_T^{\min}	data/theory	p_T^{\min}	data/theory	
12.9	2.0 ± 0.5	6.0	1.7 ± 0.5	9.5	2.4 ± 1.0	
15.0	2.3 ± 0.6	7.0	1.8 ± 0.5	13.0	2.0 ± 0.9	
18.8	1.7 ± 0.5	9.0	1.8 ± 0.5	17.5	1.8 ± 0.8	
27.6	1.7 ± 0.6	12.0	1.7 ± 0.4	26.5	2.2 ± 1.1	
37.0	1.4 ± 0.6	15.0	1.7 ± 0.4			
		19.0	1.7 ± 0.5			
		23.0	2.1 ± 0.6			
		30.0	2.0 ± 0.7			
		38.0	2.0 ± 0.9			

UA1 data at $\sqrt{s} = 0.63 \text{ TeV}$				
muon-jet		dimuons		
p_T^{\min}	data/theory	p_T^{\min}	data/theory	
15.0	1.7 ± 0.6	6.0	1.5 ± 0.4	
23.0	2.4 ± 0.8	8.0	1.8 ± 0.5	
30.0	1.6 ± 0.6	11.0	1.6 ± 0.5	
39.0	0.9 ± 0.5	15.0	1.6 ± 0.7	
46.0	1.4 ± 0.9			
54.0	0.50 ± 0.4			

Table 11.2: Ratio data/central NDE theory prediction for DØ data at $\sqrt{s} = 1.8 \text{ TeV}$ and UA1 data at $\sqrt{s} = 0.63 \text{ TeV}$.

over QCD calculations at $p_T^b < 12 \text{ GeV}/c$ reported by CDF is not observed in the D \emptyset analyses.

D \emptyset and CDF data at $\sqrt{s} = 1.8 \text{ TeV}$ as well as UA1 data at $\sqrt{s} = 0.63 \text{ TeV}$ show a b -quark production cross section above QCD predictions. The excess in the data is most pronounced for CDF at low p_T^b . D \emptyset and UA1 measurements show less of an excess.

D \emptyset and UA1 data divided by the central value of their respective theory predictions are shown in fig. 11.5 and are tabulated in table 11.2. The measurements at both center of mass energies lie systematically above the theory predictions by $\approx 2\sigma$, and agree fairly well in shape with the predictions over one order magnitude in b -quark transverse momentum (6 to 40 GeV/c) and ≈ 3 orders of magnitude in b -quark cross section (≈ 10 to 10^4 nb). The agreement in shape over a large range in p_T^b makes it unlikely that the difference between data and theory predictions is due to an imprecise parton density function parameterization. The persistence of the excess over a factor of three in center of mass energy further suggests that the QCD calculation systematically underestimates b -quark production.

11.3 Future b -Quark Cross Section Measurements at D \emptyset

The data from the 1994-95 (1b) D \emptyset run will be used to investigate b -quark production with larger statistics and to extend the kinematic range to higher

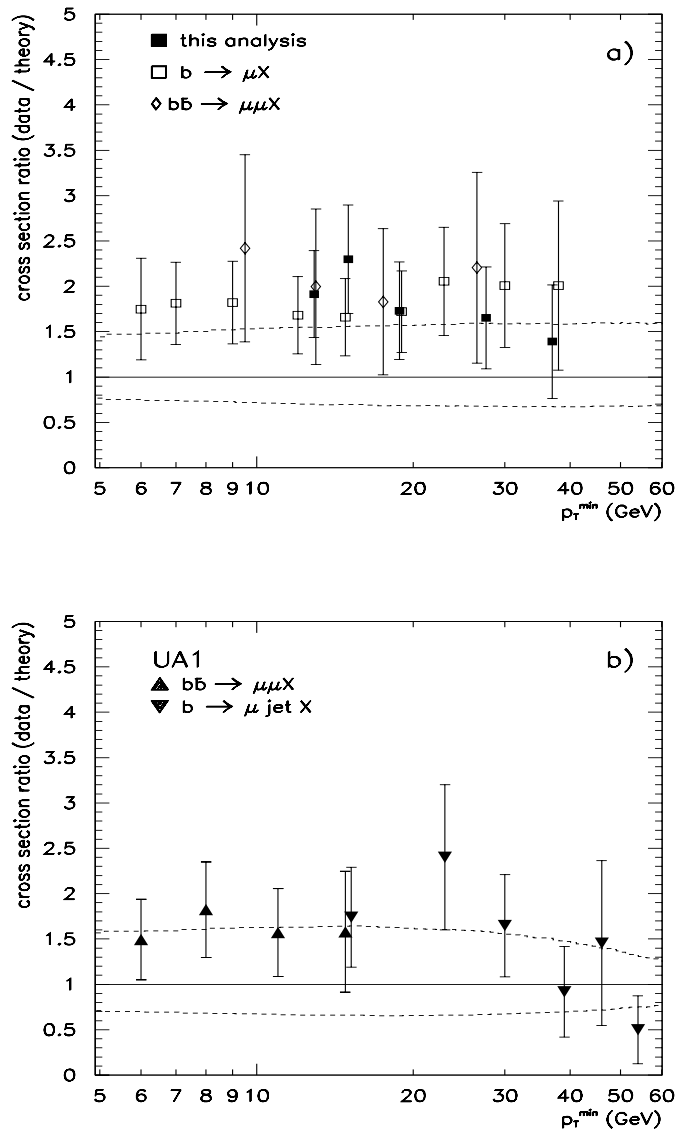


Figure 11.5: Ratio data / theory prediction for the b -quark production cross section measurement from (a) DØ at $\sqrt{s} = 1.8$ TeV for $|y^b| < 1.0$, and b) UA1 at $\sqrt{s} = 0.63$ TeV for $|y^b| < 1.5$. The theory curves are described in the text.

transverse momenta and larger rapidities. As the 1992-93 data run was the first run of the DØ detector, the muon system was not fully functional beyond $|\eta| = 0.8$ due to large beam related backgrounds and radiation damage from the main ring. The muon pseudorapidity coverage will be extended to 3.3 in the 1994-95 (1b) data run. Moreover, we expect that better calibration and increased understanding of the muon detector in run 1b will lead to

- improved understanding of the muon momentum resolution. The improvement will be facilitated by large data sets of dimuon events from J/Ψ -meson and Z -boson decays.
- improved separation of isolated muons and muons in jets. This will be accomplished through a better measurement of the muon trajectory by including calorimeter information in the muon tracking algorithm.

The problems with the jet trigger, described in section 8.2 have been addressed in the 1994-95 run:

- the low efficiency of the jet level 1 trigger below 30 GeV (section 8.2.1), due to the small cone size used in level 1 has been improved by using a larger cone of $\Delta\eta \times \Delta\Phi = 0.8 \times 1.6$.
- the saturation effect in the very forward jet level 1 trigger that contributed to the rapid falloff of the jet level 1 trigger efficiencies for $|\eta| > 2.6$ (section 8.2.1) has been corrected.

In this analysis the p_T -distribution of the b -quark was inferred from the momentum distribution of the decay muon, $b \rightarrow \mu X$. The b -quark p_T can

also be obtained directly from the calorimeter E_T of the b -jet which recoils from the jet containing the muon. This approach becomes very attractive with increasing p_T since $(\Delta p/p)^\mu \propto p$ whereas $(\Delta E/E)^{\text{jet}} \propto E^{-1/2}$. Thus $\Delta E/E = 0.1$ for a 50 GeV jet compared to $\Delta p/p = 0.4$ for a 50 GeV/c muon. In the future jet energy measurements will be used to extend the p_T -range of the b -production cross section. Improved understanding of the jet energy scale will facilitate this approach.

Finally the more precise measurement of the W/Z -boson production cross section in the 1994-95 run will reduce the errors associated with the subtraction of the W/Z -boson backgrounds in b -production studies.

In the longer term, following the 1995 collider run the DØ detector will be upgraded by the addition of a 2T central magnetic field and a new central tracking system which will give a momentum resolution $\Delta p_T/p_T$ of between $0.01 p_T$ and $0.08 p_T$ as p_T^μ varies between 2 and 50 GeV/c. A precision silicon microvertex detector [88] will have an impact parameter resolution of $12 - 21 \mu\text{m}$, allowing b -quark tagging by measuring the decaylength of the B -meson and the reconstruction of exclusive B -decays.

We are hence looking forward to more precise and more complete measurements of b -production, and to continuing tests of QCD theory.

Appendix A

Modelling of the Muon Detector Efficiencies and Resolutions

As mentioned in section 6.3, muon efficiencies and errors in the alignment of the muon chambers are simulated in a separate program run after the GEANT detector simulation. In this appendix, we will explain the algorithm of the MUSMEAR program. The efficiencies in the time, delta-time and padlatch measurements (chapter 3) are determined on a chamber by chamber basis using collider data. Basically, the efficiency for each of these quantities is determined by tabulating the number of planes in the chamber, for which time, delta-time and padlatch data are measured on a given reconstructed muon trajectory. Since there are four planes in the A layers, and three planes in the B and C layers each (section 3.5), a maximum of 10 values are available for each of the quantities per reconstructed muon.

A fraction of the raw muon data in the Monte Carlo for the padlatches, time and delta time are dropped in accordance with the experimentally determined efficiencies. MUSMEAR furthermore degrades the resolution in the

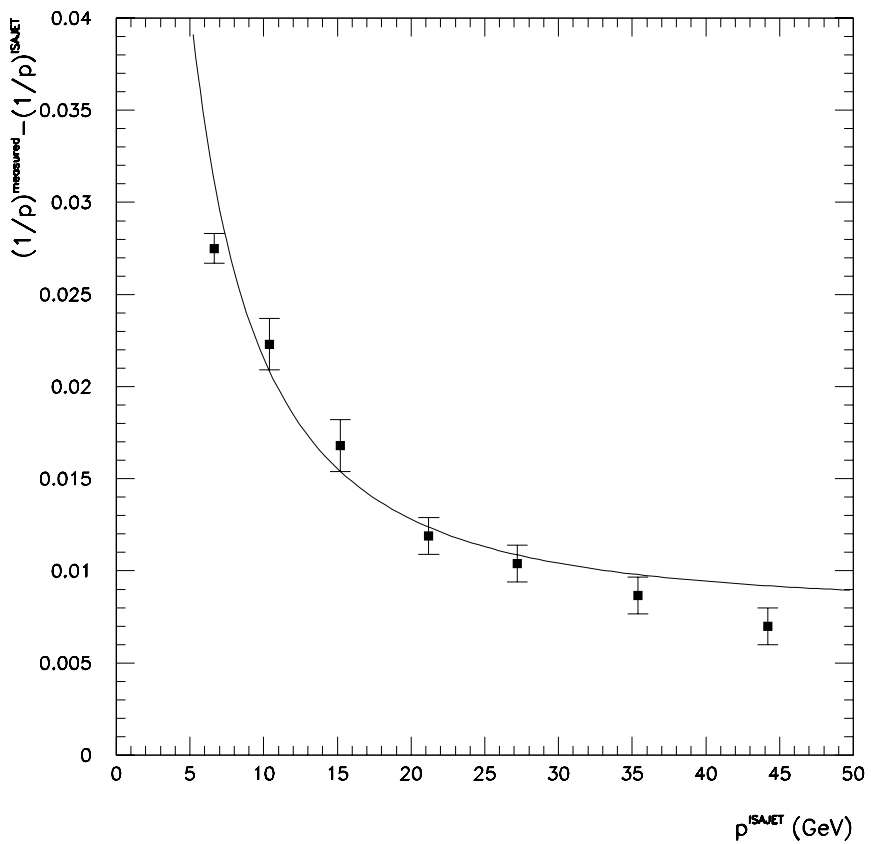


Figure A.1: Muon momentum resolutions from MUSMEAR. The curve denotes the resolution of $\Delta(1/p) = \sqrt{(0.18/p)^2 + 0.008^2}$ measured from J/ψ and Z data.

time and Δ -time measurements to make the simulated resolution conform with that measured in the detector (section 3.5).

The uncertainties in the positions of the muon chambers are simulated by using slightly different chamber positions in the detector simulation (GEANT) and the reconstruction. This models differences in muon chamber positions between the detector and the reconstruction. The chamber geometry for MUS-MEAR is based on the geometry used in GEANT, and then introduces a displacement of the position of each chamber in the drift direction according to a Gaussian distribution of width 3mm.

The 3mm alignment uncertainty was determined by matching the shape of P_T -spectra of $W \rightarrow \mu\nu$ and $Z \rightarrow \mu\mu$ data with the Monte Carlo. W and Z events are chosen because high momentum muons are most sensitive to alignment errors. For softer muons Multiple Coulomb scattering dominates the muon momentum resolution [33].

Figure A.1 shows the muon momentum resolution implemented in the Monte Carlo, it is parameterized as $\Delta(1/p) = \sqrt{(0.18/p)^2 + 0.008^2}$, where $\Delta(1/p)$ denotes the difference between reconstructed and generated (in ISAJET) values for $1/p$.

Appendix B

Decays-in-Flight of Pions and Kaons

In section 6.5 we compared the differential charged hadron spectrum between ISAJET and a measurement with the CDF detector. Here we compare the fraction of pions and kaons in the inclusive hadron spectrum from ISAJET with various experimental measurements, and we examine the probability of a pion or kaon to decay in the DØ detector.

Figure B.1 shows the particle composition of jets generated by ISAJET. More than 90% of the charged particles are pions and kaons which have decaylengths ($c\tau$) of 7.8 and 3.7 m respectively. Although the decaylength in the labframe is larger due to the particles' momentum, a fraction of them will still decay to muons in the central detectors volume.

The decay probability P for a hadron of mass m , lifetime τ and transverse momentum p_T is

$$P = BR \frac{r}{c\tau} \frac{m}{p_T} \frac{1}{r} \quad (\text{B.1})$$

where BR is the branching ratio into a muon. r is the radius of the decay volume, approximately a cylinder of radius 84 cm reaching out to the innermost

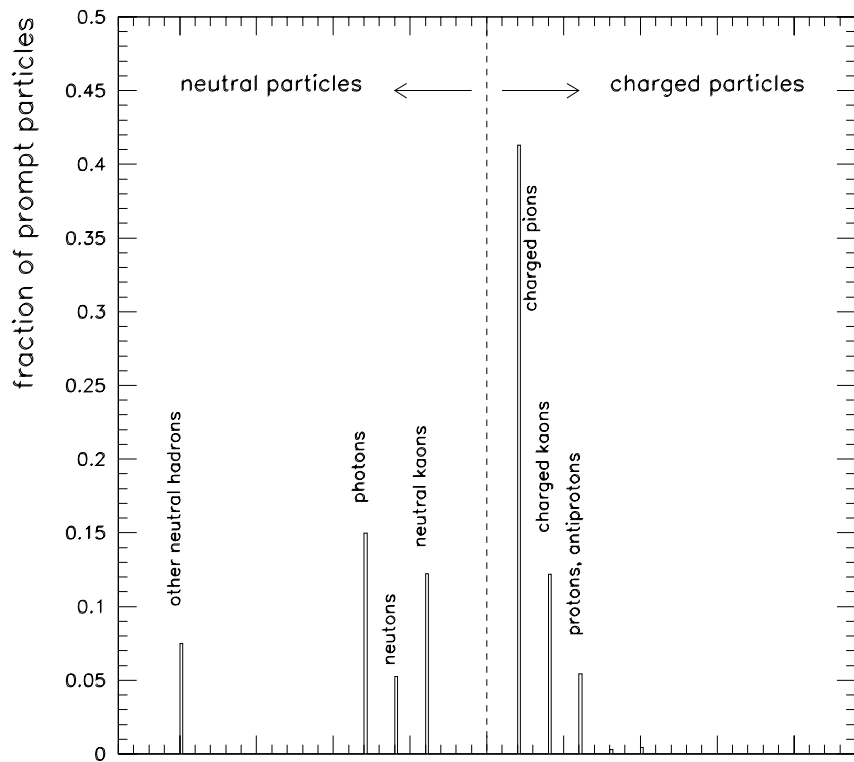


Figure B.1: Prompt particles generated in ISAJET jet events. Only particles of $p_T > 4 \text{ GeV}/c$ and $|\eta| < 0.8$ are plotted. More than 90% of the charged particles are pions and kaons which can decay to muons in the detector.

layer of the electromagnetic calorimeter. Hence the decay probability can be approximated by $P_\pi = 0.015/p_T^\pi$ and $P_K = 0.070/p_T^K$.

The cross-section for muons from in-flight decays depends on the production cross section for the parent hadrons, the fraction of these which decay and their decay kinematics. It is important to model both the production rate and the topology of events containing in-flight decays. In this analysis $p\bar{p} \rightarrow \text{jets}$ events from ISAJET are input to a GEANT detector simulation which randomly selects a single pion or kaon in the event and decays it into a muon and a neutrino [89]. The decay probability is then calculated using the formula:

$$W = N P_i \prod_{j=1}^{N-1} (1 - P_j) \quad (\text{B.2})$$

where N is the number of pions and kaons in the event and P_i is the probability that the i -th pion or kaon will decay, and P_j is the decay probability of the remaining pions and kaons. The quantity W is the weight assigned to the event. This approach of “forcing” decays is adopted to avoid processing large amounts of Monte Carlo which do not contain in-flight decays.

Figure B.2 shows the fractions of pions and kaons in the ISAJET charged hadron spectrum. The charged pion and charged kaon fractions are independent of p_T at 0.73 ± 0.05 and 0.18 ± 0.05 , respectively. In comparison, estimates from data taken by the UA2 [90] and UA5 [91] collaborations at $\sqrt{s} = 0.54$ TeV predict charged pion and kaon fractions of 0.58 ± 0.03 and 0.23 ± 0.06 . The Fermilab E605 collaboration measured a charged K/π -ratio of 0.28 ± 0.03 and a $(p + \bar{p})/\pi$ ratio of 0.04 ± 0.01 at $\sqrt{s} = 38.8$ GeV [58], which translates into

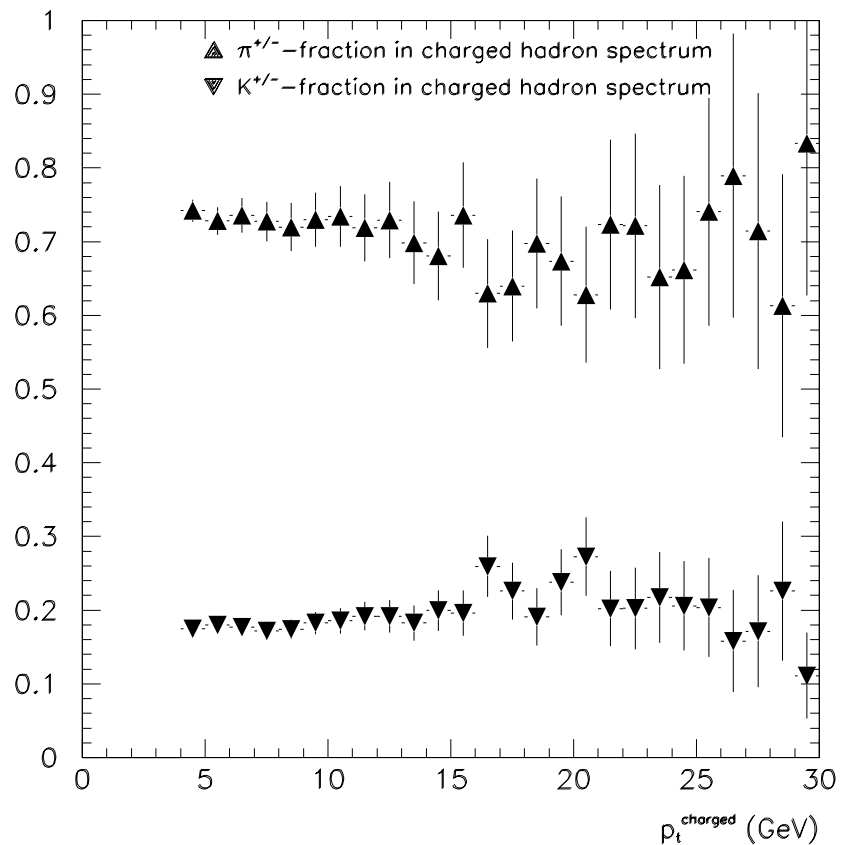


Figure B.2: Fraction of charged pions and kaons in the inclusive charged hadron spectrum generated by ISAJET.

pion and kaon fractions of 0.75 and 0.21, respectively. Since the pions or kaons are produced in the fragmentation of partons we expect that their relative proportions in charged hadron spectrum are independent of the center of mass energy. In the fragmentation scheme adopted by ISAJET (section 6.2), light quark are generated according to the ratio $u : d : s = 0.4 : 0.4 : 0.2$, independent of the center of mass energy of the interaction as well as of the p_T of the fragmenting parton.

The total rate of in-flight decays is relatively insensitive to the exact pion and kaon fractions. Replacing the ISAJET predictions by the UA1/UA5 values results in an 8% increase in muons from in-flight decays, while the E605 fractions give 6% fewer in-flight decays than ISAJET. We account for this by assigning a systematic error in the rate of in-flight decays due to of 8%.

Appendix C

Bayes' Method for Unfolding Resolution Effects

We describe in this section the method used for correcting the data for the effects of the muon momentum resolution. This unsmearing procedure allows us to transform the muon differential cross section in terms of measured muon transverse momenta, $d\sigma/dp_T^{\text{reco}}$, into the spectrum in terms of the “true” muon transverse momenta, $d\sigma/dp_T^{\text{true}}$. The method chosen in this analysis for the transformation is based on Bayes' theorem [74, 75].

Bayes' theorem can be stated in terms of n_c independent mutually exclusive causes C_i which produce an effect E . The conditional probability that effect E is caused by cause C_i , $P(C_i|E)$, can be written in terms of the probability of C_i causing E , $P(E|C_i)$:

$$P(C_i|E) = \frac{P(E|C_i) \cdot P(C_i)}{\sum_{l=1}^{n_c} (P(E|C_l) \cdot P(C_l))} \quad (\text{C.1})$$

where $P(C_i)$ is the probability of event C_i to occur.

In this application, we associate the causes with the production of a muon

with a true transverse momentum p_T^{true} , and the effects with the reconstructed transverse momentum p_T^{reco} . The true and reconstructed transverse momenta differ due to Multiple Coulomb Scattering of the muons as well as to the spatial resolution of the muon system (chapter 3.5 and appendix A). We consider $n_e = 9$ effects occurring with probabilities $P(E_j)$, $j = 1 \rightarrow n_e$, each of them representing a muon which is reconstructed in one of the nine bins of p_T^{RECO} (see table 9.1). The $n_c = 9$ causes represent the muons being produced with a momentum in one of the bins.

The differential cross section of the unsmeared (true) muon spectrum for the i -th bin, $(d\sigma/dp_T)_i^{\text{true}}$ can be written in terms of the spectrum of reconstructed muons, $(d\sigma/dp_T)_j^{\text{reco}}$, as follows:

$$\left(\frac{d\sigma}{dp_T} \right)_i^{\text{true}} = \sum_{j=1}^{n_c} P(C_i|E_j) \cdot \left(\frac{d\sigma}{dp_T} \right)_j^{\text{reco}}. \quad (\text{C.2})$$

We can then substitute Bayes' theorem (C.1) and get

$$\left(\frac{d\sigma}{dp_T} \right)_i^{\text{true}} = \sum_{j=1}^{n_c} \frac{P(E_j|C_i) \cdot P(C_i)}{\sum_{l=1}^{n_c} (P(E_j|C_l) \cdot P(C_l))} \cdot \left(\frac{d\sigma}{dp_T} \right)_j^{\text{reco}}. \quad (\text{C.3})$$

The probabilities $P(E_j|C_j)$ can be obtained from Monte Carlo. They are independent of the shape of the true spectrum, and merely describe how each p_T interval of the true spectrum maps into the reconstructed spectrum.

The probabilities $P(C_i)$ for each momentum bin i are converted into differential cross sections by multiplying by the total differential cross sections. Since the muon efficiencies are already corrected for efficiencies, the true and reconstructed spectra vary in shape, but have the same total cross section.

Thus

$$\left(\frac{d\sigma}{dp_T} \right)_i = P(C_i) \cdot \sum_{j=1}^{n_c} \left(\frac{d\sigma}{dp_T} \right)_j. \quad (\text{C.4})$$

The algorithm is iterative and starts with an initial guess for the true cross section, from which we get the first set of $P(C_i)$'s. The ISAJET $b \rightarrow \mu X$ cross section (chapter 6) is taken as the initial guess. The elements of the "smearing matrix" $P(E_j|C_i)$ are obtained by comparing the values of the muon transverse momenta from ISAJET with the reconstructed values. The values for $(d\sigma/dp_T)_i^{\text{true}}$ are used to calculate the $P(C_i)$ for the next iteration. A χ^2 comparison is made between two consecutive iterations, and the iteration process is terminated if the difference in χ^2 is less than 0.01 (for 9 degrees of freedom).

Bibliography

- [1] J. A. Appel *et. al*, Phys. Rev. Lett. **39**, 252 (1977) .
O. Achterberg *et. al*, Phys. Lett. **B76**, 243 (1978).
- [2] S. Abachi *et. al*, Phys. Lett. **B 122**, 2632 (1995).
- [3] F. Abe *et. al*, Phys. Rev. Lett. **74**, 2626 (1995).
- [4] C. Albajar *et. al.*, Phys. Lett. **B256**, 121 (1991).
- [5] F. Abe *et. al*, Phys. Rev. Lett. **71**, 2396 (1993).
- [6] A. Maciel, to appear in the Proceedings of the European Particle Physics Conference, Brussels, July 1995.
- [7] S. D. Holmes and V. A. Yarba, “Fermilab Tevatron and Upgrade Status”, FERMILAB-CONF-94-360 (1994).
- [8] “Large Hadron Collider in the LEP Tunnel”, ECFA 84/85, CERN 84-10,2.09.1984.
- [9] G. Miller *et. al.*, Phys. Rev. **D55**, 528 (1972).
- [10] N. Isgur and. M.B. Wise, Phys. Lett. **B232** 113 (1989); *ibid.* **B237**, 537 (1990).
- [11] M. Neubert, SLAC Report No. SLAC-PUB 6263 (1993)
- [12] Particle Data Group, “Review of Particle Properties”, Phys. Rev. **D50** 1437 (1994).
- [13] Particle Data Group, “Review of Particle Properties”, Phys. Rev. **D50**, 1299 (1994).

- [14] P. Nason, S. Dawson and R. K. Ellis, Nucl. Phys. **B327**, 49 (1989)
- [15] W. Beenakker, W. L. van Neerven, R. Meng, G.A. Schuler and J. Smith, Nucl. Phys. **B351**, 507 (1991).
- [16] M. Mangano, P. Nason and G. Ridolfi, Nucl. Phys. **B373**, 259 (1992)
- [17] A. Martin, R. Roberts, J. W. Stirling, Phys. Rev. **D47**, 867 (1993).
- [18] M. Diemoz, F. Ferroni, E. Longo and G. Martinelli, Z. Phys **C39**, 21 (1988).
- [19] S. Abachi *et. al.*, Phys. Rev. **D50**, 5518 (1994).
 S. Abachi *et. al.*, Phys. Rev. **D50**, 5535 (1994).
 S. Abachi *et. al.*, Phys. Rev. **D50**, 5550 (1994).
- [20] R. Rubenstein *et. al.*, “Status of Fermilab E710”, FERMILAB-Conf-93/216-E (1993) (Unpublished).
- [21] N. Amos *et. al.*, “Change to the DØ Luminosity Monitoring Constant”, Fermilab TM-1911 (1995).
- [22] S. Abachi *et. al.*, Nucl. Inst. and Meth. **A338**, 187 (1990)
- [23] D. Pizzuto, Ph.D. Thesis, SUNY at Stony Brook, 1989 (Unpublished).
- [24] S. Abachi *et al.*, Nucl. Instrum. Meth. **A324**, 53 (1993).
- [25] R. Hirosky, “The Response of the DØ Central Calorimeter to Electrons and Pions from 2 through 150 GeV/c”, DØ Note 1499, 1993 (Unpublished).
- [26] S. Abachi *et. al.*, Nucl. Inst. and Meth. **A338**, 219 (1990).
- [27] Yu. M. Antipov *et. al.*, Nucl. Inst. and Meth. **A297**, 121 (1990).
- [28] D. Hedin, “Preliminary DØ Punchthrough Rates”, DØ Note 1738, 1993 (Unpublished).
- [29] K. Lang, Ph.D. Thesis, University of Rochester, 1985 (Unpublished).
- [30] S. Abachi *et. al.*, Nucl. Inst. and Meth. **A338**, 221 (1990).

- [31] H. Haggerty *et. al.*, “Time-to-Distance Relation for DØ Muon Drift Tubes”, DØ Note 2104, 1994 (Unpublished).
- [32] D. Hedin (personal communication).
- [33] C. Gerber, Ph. D. Thesis, University of Buenos Aires, 1995 (Unpublished).
- [34] A. Baldini, W.G. Moorhead, and D.R.O. Morrison, CERN; and COMPASS Group, IHEP, Serpukhov, Russia. See “Total Cross Sections for Reactions for Reactions of High Energy Particles”, Landolt-Boernstein, New Series Vol. **I/12 a** and **I/12 b**, ed. H. Schopper (1988).
Particle Data Group, “Review of Particle Properties”, Phys. Rev. **D50**, 1336 (1994).
- [35] M. Goosens *et. al.*, CERN Library Program N0. Q100 (1991).
- [36] S. Abachi *et. al.*, Nucl. Inst. and Meth. **A338**, 223 (1990).
- [37] S. Squarcia, CERN Report N0. CERN-PPE/94-99, 1994.
- [38] J. M. Butler, “Main Ring Veto”, DØ Note 1682, 1993 (Unpublished).
- [39] S. Abachi *et. al.*, Nucl. Inst. and Meth. **A338**, 224 (1990).
- [40] K. Bazizi and R. Hall, “Muon Module Address Card Description”, DØ Note 1143, 1991 (Unpublished).
- [41] S. Abachi *et. al.*, Nucl. Inst. and Meth. **A338**, 228 (1990).
- [42] J. Thompson, Ph. D. Thesis, SUNY Stony Brook, 1994 (Unpublished).
- [43] B. May, Ph. D. Thesis, University of Arizona, 1994 (Unpublished).
- [44] J. Cochran (personal communication).
- [45] B. May, Ph. D. Thesis, University of Arizona, 1994 (Unpublished).
- [46] J. Bendich *et. al.*, “Beam XY Position at DØ Determined the the VTX Chamber”, DØ Note 2331, 1994 (Unpublished).
- [47] C. Gerber *et. al.*, “Muon Momentum Determination”, DØ Note 2240, 1994 (Unpublished).

- [48] U. Heintz, “Energy Scale Corrections for W Mass Measurements”, DØ Note 1819, 1993 (Unpublished).
- [49] F. Paige and S. Protopopescu, ISAJET 6.49. “A Monte Carlo Event Generator for pp and $p\bar{p}$ Interactions”, Fermilab Computing Division, PM0059, 1992
- [50] R. Brun *et al.* CERN Program Library, GEANT 3.15 program manual.
- [51] A. Geiser, Ph. D. Thesis, University of Aachen, 1992 (Unpublished).
- [52] D. Hedin and L. Markosky, “ b -Physics Results from DØ”, Proceedings of the 27th International Conference on High Energy Physics, Glasgow, Institute of Physics Publishing, 1995, p.997
- [53] E. Eichten *et. al.*, Rev. Mod. Phys. **56**, 579 (1984).
- [54] CTEQ Collaboration, J. Botts *et al.*, Phys. Lett. **B304**, 159 (1993).
- [55] R. Field and R. Feynman, Nucl. Phys. **B136**, 1, (1978)
- [56] J. C. Collins and T.D. Gottschalk, “Assessment of Perturbative Monte Carlos for Hadron Hadron Scattering”, Proceedings of the 1996 Summer Study on the Physics of the Superconducting Supercollider, American Physical Society, 1986.
- [57] P. Quintas and T. Diehl (personal communication).
- [58] T. Huffman, Ph.D Thesis, Purdue University, 1992 (Unpublished)
- [59] S. Abachi *et. al.*, Phys. Rev. Lett. **75**, 1456 (1995).
- [60] S. Chopra (personal communication).
- [61] Particle Data Group, “Review of Particle Properties”, Phys. Rev. **D50**, 1253 (1994).
- [62] Particle Data Group, “Review of Particle Properties”, Phys. Rev. **D50**, 1251 (1994).
- [63] A. Klatchko and S. Youssef “A Toy Monte Carlo Study of the Momentum Resolution of the WAMUS in DØ”, DØ Note 1804, 1993 (Unpublished).

- [64] R. Astur, J. Blazey and D. Elvira "A Study of Standard Jet Cuts and Efficiencies Using DØ Collider Data", DØ Note 1763, 1993 (Unpublished).
- [65] D. Perkins, *Introduction to High Energy Physics*, Addison Wesley Publishing, New York, 1987, p. 42.
- [66] D. Norman, "Some comments on PJETS", DØ Note 2197, 1993 (Unpublished).
- [67] R. D. Field and R. P. Feynman, *Nucl. Phys.* **B136** (1978).
- [68] D. Elvira, Ph. D. Thesis, University of Buenos Aires, 1995 (Unpublished).
- [69] M. Bhattacharjee *et. al.*, "Efficiencies of the Standard Jet Cuts", DØ Note 2197, 1994 (Unpublished).
- [70] E. James, Ph. D. Thesis, University of Arizona, 1995 (Unpublished).
- [71] Particle Data Group, "Review of Particle Properties", *Phys. Rev.* **D50**, p. 1611 and 1644 (1994).
- [72] A. Smith, Ph. D. Thesis, University of Arizona, 1995 (Unpublished).
- [73] J. Chrin, *Z. Phys.* **C36**, 163 (1987).
- [74] R. Hogg and E. Tanis. *Probability and Statistical Inference*, 2nd ed., Macmillan Publishing Company, New York, 1983.
- [75] G. D'Agostini, "A Multidimensional Unfolding Method Based on Bayes' Theorem", DESY preprint 94 099 (1994).
- [76] N. Ellis and A. Kernan, *Phys. Rep.* **195** (1990).
- [77] D. Fein, Ph. D. Thesis, University of Arizona, 1995 (in preparation).
- [78] J. Geiser, Ph. D. Thesis, University of Aachen, Germany, 1992 (Unpublished).
- [79] F. Abe *et. al.*, *Nucl. Inst. and Meth.* **A271**, 387 (1988).
- [80] F. Abe *et. al.*, *Phys. Rev. Lett.* **71**, 500 (1993).

- [81] F. Abe *et. al.*, Phys. Rev. Lett **69**, 3704 (1992).
- [82] F. Abe *et. al.*, Phys. Rev. **D50**, 2537 (1993).
- [83] F. Abe *et. al.*, Phys. Rev. Lett **68**, 3403 (1992).
- [84] F. Abe *et. al.*, Phys. Rev. **D50**, 4254 (1994).
- [85] S. Abachi *et. al.*, Phys. Rev. Lett **74**, 3548 (1995).
S. Abachi *et. al.*, “Inclusive Muon and b -Quark Production Cross Sections in $p\bar{p}$ Collisions at $\sqrt{s} = 1.8$ TeV.”, FERMILAB-CONF-95/208-E
- [86] S. Abachi *et. al.*, “Inclusive Muon and b -Quark Production Cross Sections in $p\bar{p}$ Collisions at $\sqrt{s} = 1.8$ TeV.”, FERMILAB-CONF-95/208-E.
- [87] C. Murphy, Ph. D. Thesis, Indiana University, 1995 (Unpublished).
- [88] M. Wayne, “The DØ Tracker Upgrade and Projections for b -Physics” to appear in the proceedings of Beauty’94, Blois, France, June 1994. FNAL-CONF-94 230-T.
- [89] Herbert Greenlee (personal communication).
- [90] M. Banner *et. al.*, Phys. Lett. **B 122**, 322 (1983).
- [91] G. J. Alner *et. al.*, Nucl. Phys. **B 285**, 505 (1985).